EFFICIENT PIEZOELECTRIC BEAM FINITE ELEMENT FORMULATIONS BASED ON COUPLED POLYNOMIAL INTERPOLATIONS

A thesis submitted
in partial fulfillment for the degree of

Doctor of Philosophy

by

LITESH NANDKISHOR SULBHEWAR

Department of Aerospace Engineering
INDIAN INSTITUTE OF SPACE SCIENCE AND TECHNOLOGY
Thiruvananthapuram – 695547

January 2015

CERTIFICATE

This is to certify that the thesis entitled **EFFICIENT PIEZOELECTRIC BEAM FINITE ELEMENT FORMULATIONS BASED ON COUPLED POLYNOMIAL INTERPOLATIONS** submitted by **LITESH NANDKISHOR SULBHEWAR** to the Indian Institute of Space Science and Technology, Thiruvananthapuram, in partial fulfillment for the award of the degree of **Doctor of Philosophy**, is a *bona fide* record of the research work carried out by him under my supervision. The contents of this thesis, in full or in parts, have not been submitted to any other Institute or University for the award of any degree or diploma.

Dr. P. Raveendranath
Supervisor
Department of Aerospace Engineering
Indian Institute of Space Science and Technology

Dr. Salih A.
Associate Professor & Head
Department of Aerospace Engineering
Indian Institute of Space Science and Technology

Thiruvananthapuram
January, 2015

DECLARATION

I declare that this thesis entitled **EFFICIENT PIEZOELECTRIC BEAM FINITE ELEMENT FORMULATIONS BASED ON COUPLED POLYNOMIAL INTERPOLATIONS** submitted in partial fulfillment of the Degree of **Doctor of Philosophy** is a record of original work carried out by me under the supervision of **Dr. P. Raveendranath**, and has not formed the basis for the award of any other degree or diploma, in this or any other Institution or University. In keeping with the ethical practice in reporting scientific information, due acknowledgements have been made wherever the findings of others have been cited.

Litesh Nandkishor Sulbhewar
(SC10D007)

Thiruvananthapuram
January 2015

ACKNOWLEDGEMENTS

With a deep sense of gratitude, I wish to express sincere thanks to my supervisor **Dr. P. Raveendranath** for his excellent guidance, advice and support. His constant encouragement, numerous interesting ideas, and meticulous review during the entire course of this research have been invaluable.

I am grateful to Prof. Kurien Issac (Dean, IIST) and Dr. A. Salih (HOD, Aerospace Engineering), for providing necessary facilities to carry out my research work. Special thanks are due to Mr. Mohan Sukumar (System Administrator- Computer System Group) for the excellent computational and network support.

The author would like to acknowledge and thank the Department of Space-Government of India for the IIST-ISRO fellowship provided to him.

I am thankful to all the members of the Doctoral Committee, whose timely guidance helped me stay on the right track for my research.

Among the co-scholars and friends who have shared my joys and frustrations in the campus of IIST, I wish to express my sincere gratitude to Mr. Muthukumaran, Mr. Mathiazhagan, Mr. Rahul Waghmare, Ms. Parvathy, Ms. Roshina, Mr. Siby Chacko and Dr. Narayanan. I thank them all for keeping up my morale all along and for making the memorable part of my years at IIST, as a research scholar.

No amount of words would be sufficient to express my gratitude to my family members for their forbearance and reassurances provided to me.

Litesh Nandkishor Sulbhewar

ABSTRACT

The performance of the conventional two-noded Equivalent Single Layer (ESL) extension mode piezoelectric beam finite elements is affected by ‘locking’ phenomena. The conventional formulations available in the literature employ independent polynomials for the interpolation of mechanical displacements and transverse electric potential. ‘Material locking’ due to bending-extension coupling and ‘shear locking’ due to bending-shear coupling hamper the finite element convergence, while ‘piezolocking’ due to induced potential coupling affects the accuracy. Hence, the conventional formulations demand a refined mesh in the axial direction, to overcome shear and material locking effects and a sublayered modelling of the electric potential in the transverse direction, to overcome piezolocking effects. However, these measures to circumvent locking effects are inefficient because they lead to increase in number of nodal degrees of freedom and computational effort. In this thesis, accurate and efficient ESL piezoelectric beam finite elements are developed using coupled polynomials for field interpolations, without increasing the number of nodal degrees of freedom. The formulations are developed for Euler-Bernoulli theory (EBT), first-order (FSDT) and higher-order (HSDT) shear deformation theories.

The higher-order through-thickness distribution of electric potential in a physical piezoelectric layer, consistent with the respective ESL theory, is derived from an electrostatic equilibrium equation to eliminate piezolocking. This consistent potential contains, in addition to conventional linear terms, higher-order coupled term(s) which depends only on the bending strain and hence does not bring in any additional nodal electric potential degree of freedom in the formulation. The governing equilibrium equations derived from a variational formulation are used to establish the relationship between field variables involved in the ESL theory based formulations with respective consistent potential. These relationships lead to a set of coupled polynomials for their interpolations. A set of coupled shape functions obtained from these polynomials incorporate the bending-extension, bending-shear and induced potential couplings in a variationally consistent manner.

The proposed coupled polynomial based piezoelectric beam finite element formulations are validated by benchmark solutions from ANSYS 2D simulations. Comparison of results for numerous test problems proves improved accuracy and efficiency of the proposed formulations over their conventional counterparts.

TABLE OF CONTENTS

LIST OF FIGURES

LIST OF TABLES

ABBREVIATIONS

CPI	Coupled Polynomial Interpolation
CP	Consistent Potential
ESL	Equivalent Single Layer
EB	Euler Bernoulli
FSDT	First-order Shear Deformation Theory
HSDT	Higher-order Shear Deformation Theory
SBT	Sandwich Beam Theory
LP	Linear Potential

NOTATIONS

A	Area of cross-section, *m^2*
b	Width, *m*
h	Thickness, *m*
L	Length, *m*
H	Potential energy, *Nm*
K	Kinetic energy, *Nm*
W	Work, *Nm*
ε	Normal strain
γ	Shear Strain
σ	Normal stress, Nm^{-2}
τ	Shear stress, Nm^{-2}
C	Elastic coefficient, Nm^{-2}
D	Electric displacement, Cm^{-2}
E	Electric field, Vm^{-1}
d	Piezoelectric strain constant, mV^{-1}
e	Piezoelectric stress constant, $NV^{-1}m^{-1}$ *or* Cm^{-2}
ϵ	Permittivity, Fm^{-1}
$\varphi(x,z)$	Two dimensional electric potential field, *volt*
$\phi(x)$	Electric potential, *volt*
ρ	Mass density, kgm^{-3}
ξ	Natural coordinate along the length
x	Global coordinate along the length
U	Global nodal mechanical displacement vector
Φ	Global nodal electric potential vector
F, Q	Global nodal mechanical and electrical force vectors
K_{uu}	Global mechanical stiffness matrix
$K_{u\varphi}$	Global electro-mechanical stiffness matrix

$K_{\varphi\varphi}$	Global electric stiffness matrices
M	Global mass matrix

Subscripts

al	Aluminum
c	Core layer
i	Count for piezoelectric layers
k	Count for total (piezoelectric+host) layers
p	Piezoelectric layer
x	Longitudinal direction
y	Direction into the plane
z	Transverse direction
0	Centroidal quantities

CHAPTER 1

INTRODUCTION

1.1 Piezoelectric Smart Structures

In the recent years, the need of self controllable structures has motivated the research and development of smart structures. A structure which can respond to any change in the external environment can be termed as 'smart or intelligent structure'. Such structures make use of special materials called 'smart materials'. Smart materials have couplings between different physical fields present in them, which can be used effectively to control their behaviour. Piezoelectric smart materials have coupling between mechanical and electrical fields. The history of piezoelectricity dates to 1880 when Pierre and Jacques Curie discovered the piezoelectric effect in several substances such as the quartz crystal, which is a naturally occurring piezoelectric material. Lead Zirconate Titanate (PZT) and Polyvinylidene Fluride (PVDF) are widely used ceramic and polymer based piezoelectric materials, respectively.

Due to their high reliability, piezoelectric smart structures are widely used in the shape and vibration control technologies. In piezoelectric materials, the presence of mutual dependency between stress/strain field and electric field/voltage makes them capable of responding to the subjected loading (electrical or mechanical) environment in a real time. A piezoelectric material can be used as a *sensor* to generate the voltage corresponding to the subjected mechanical field or as an *actuator* to generate corrective force corresponding to the subjected electric field.

Piezoelectric beams are widely employed in the modern structural applications. The application of piezoelectric beams generally involves two modes of operation: *Extension* mode and *Shear* mode. In the extension mode, the coupling between longitudinal strain and transverse electric field is utilised while in the shear mode, the coupling between shear strain and transverse electric field is utilised. The directional nature of the electromechanical coupling in piezoelectric material is achieved by 'poling' process in which a high electric field is applied to re-orient the electric dipoles. In the extension mode beams, transversely poled piezoelectric material is used whereas in the shear mode beams, axially poled piezoelectric material is used. Design of piezoelectric smart beams essentially involves mathematical modelling and structural analyses. The present research work focuses on the finite element modelling and analysis of the extension mode piezoelectric smart beams.

Piezoelectric beams in extension mode of operation is one of the widely used mechanisms to control the behaviour of structures. In a typical extension mode of operation, piezoelectric layers are bonded to the top and bottom surfaces of the host structure, as shown in Fig. 1.1, in which P is the poling direction and E_3 is the applied electric field in the transverse direction. The host cantilever beam of conventional material is bended upward due to the contraction and extension of the oppositely poled top and bottom piezoelectric layers, respectively, under the applied electric field.

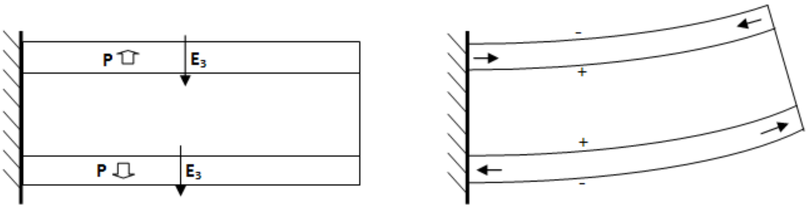

Figure 1.1: Extension mode operation of piezoelectric smart beam.

1.2 Analysis of Extension-Mode Piezoelectric Smart Beams

Structural analysis to predict the response under the field conditions plays an important role in the design of piezoelectric beams. Unlike beams of conventional materials, the presence of electro-mechanical coupling presents great challenges in the development of reliable and efficient tools for modelling and analysis of piezoelectric beams.

The electromechanical coupling renders analytical solutions extremely cumbersome, even for simple geometries and loadings. Among the numerical methods for solving field problems, the Finite Element Method (FEM) has emerged as a versatile tool for the analysis of piezoelectric structures with complex geometry, boundary condition and loading. In the FEM, the structure is visualized as an assemblage of simple geometric shapes called *finite elements*, defined by nodal points. The field variables (displacement, stress, strain, electric potential, electric field, electric displacement etc.) are interpolated within each element using simple assumed functions. The field equations for whole structure are obtained as an assemblage of elements in terms of nodal values of the field variables chosen. Based on the particular variational method, different types of piezoelectric beam finite element formulations are available. However, the displacement based piezoelectric beam finite element models have been very popular by virtue of their simplicity and adaptability. The general constitutive relations for the displacement based piezoelectric finite elements are given as:

$$\sigma_{ij} = C^{E}_{ijkl}\varepsilon_{kl} - e_{kij}E_k$$
$$D_m = e_{mkl}\varepsilon_{kl} + \epsilon^{\varepsilon}_{mk}E_k$$

where σ= Stress tensor (Nm^{-2}), C= Stiffness when electric field is constant (Nm^{-2}), ε= Strain tensor, D= Electric displacement vector (Cm^{-2}), E= Electric field vector (Vm^{-1}), e= Piezoelectric constant ($NV^{-1}m^{-1}$) or (Cm^{-2}), ϵ= Permittivity under constant strain (Fm^{-1}).

The Equivalent Single Layer (ESL) theory based *two-noded* beam finite elements are widely used to model piezoelectric beam structures. ESL theories employ a single function to define the beam deformation kinematics across the whole thickness. There are various types of ESL theories based on the approximation of the transverse shear strain across the thickness of the beam, as mentioned below:

- **Euler-Bernoulli Theory (EBT)**: Considers linear longitudinal displacement across the thickness and neglects deformation due to transverse shear strain, as:
  $u(x,z) = u_0(x) - zw_0'(x); \quad w(x,z) = w_0(x)$ and
  $\gamma(x,z) = \partial u(x,z)/\partial z + \partial w(x,z)/\partial x = 0$
  where $u(x,z)$ and $w(x,z)$ are the displacements along the longitudinal (x) and transverse direction (z), respectively. The sub-functions $u_0(x)$ and $w_0(x)$ are the longitudinal and transverse displacements at the centroidal axis of the beam, respectively. $\gamma(x,z)$ is the transverse shear strain and $()'$ denotes d/dx.

- **First-order Shear Deformation Theory (FSDT)**: Considers linear longitudinal displacement and constant shear strain across the thickness, as:
  $u(x,z) = u_0(x) + z\theta(x); \quad w(x,z) = w_0(x)$ and

$\gamma(x,z) = \partial u(x,z)/\partial z + \partial w(x,z)/\partial x = \theta(x) + w_0^{'}(x)$
where $\theta(x)$ is the section rotation.

- **Higher-order Shear Deformation Theory (HSDT)**: Considers cubic longitudinal displacement and quadratic shear strain across the thickness. The usual form of Reddy's HSDT field is given as:
  $u(x,z) = u_0(x) + z\theta(x) - \frac{4}{3h^2}z^3\left[\theta(x) + w_0^{'}(x)\right]; \quad w(x,z) = w_0(x)$ and
  $\gamma_{xz}(x,z) = \partial u(x,z)/\partial z + \partial w(x,z)/\partial x = \left(1 - z^2\frac{4}{h^2}\right)\left[\theta(x) + w_0^{'}(x)\right]$
  where h is the total thickness of the beam.

In extension mode ESL based piezoelectric beam finite elements, the coupling between longitudinal mechanical stress and transverse electric field is accommodated in the formulation through constitutive relations, using piezoelectric stress coefficient e_{31}. The electric field in the transverse direction is obtained as $E_z(x,z) = -\partial\varphi(x,z)/\partial z \; (V/m)$, the order of which depends on the order of interpolation of $\varphi(x,z)$ in the transverse direction.

1.3 Performance Related Issues in Displacement Based Piezoelectric Beam Finite Element Models

Numerous displacement based piezoelectric beam finite element formulations with various theories and assumptions are available in the literature. The performance of a finite element formulation can be best assessed by evaluating the convergence characteristic and accuracy of the solution.

1.3.1 Issues related to convergence

In the displacement based methods, convergence characteristic of a beam finite element essentially depends on the order of polynomial employed for field variable interpolation in the longitudinal direction. The minimum order of polynomial for each field variable is governed by continuity requirements imposed by the variational formulation employed. Use of lowest permissible order of polynomial naturally leads to the two-noded beam elements, which are widely used for structural analyses. However, it is observed that the nature of the convergence characteristic of low-order beam elements depends on the extent of bending-extension coupling and bending-shear coupling. These couplings in turn depend on the geometric and/or material configurations of the beam.

Bending-extension coupling

Generally, most of the piezoelectric beams are made up of host structure of conventional materials with asymmetrically bonded/embedded piezoelectric layers/patches. The asymmetry in the material distribution over the cross-section of the beam activates the 'bending-extension' coupling mechanism in the piezoelectric beam finite elements. The two noded EBT, FSDT and HSDT based piezoelectric beam finite elements which use assumed linear polynomial approximations for the interpolation of axial displacement (u_0), are inefficient in handling bending-extension coupling and hence show poor convergence. The deterioration in the convergence due to bending-extension coupling is generally termed as *material locking*.

Presence of material locking effects demands refinement of finite element mesh to yield reliable results. Use of higher-order polynomial interpolation for u_0 also tend to eliminate ill-effects of material locking. However, use of higher order independent polynomial necessitates either the addition of intermediate nodes or the use of derivative of u_0 as additional degrees of freedom at the existing nodes. Hence, these methods to yield a reliable solutions increase the number of global nodal degrees of freedom and hence increase the computational costs.

Bending-shear coupling

In the conventional two-noded FSDT and HSDT beam finite element formulations, there exists a coupling between bending and shear by virtue of the definition of shear strain field. The shear strain field is computed as the sum of the bending rotation (θ) and derivative of the transverse displacement ($w_0^{'}$) of the beam.

In the two-noded isoparametric FSDT beam formulation, where linear polynomials are employed for interpolating w_0 and θ, the polynomial expression for transverse shear strain would contain a linear term from θ field, which has no matching contribution from w_0 field. This unmatched or inconsistent *linear* term in the shear strain, contributed by θ

leads to a significantly poor bending response in the thin regimes and adversely affects the convergence characteristics. This phenomenon is widely known as ‘shear locking’. Various methods have been practised to eliminate the ill-effects of shear locking in FSDT beam elements.

Reduced integration (RI) techniques have been widely used to alleviate shear locking in FSDT-based elements. A one-order-lower reduced integration of transverse shear energy can be shown to nullify one or more higher order components of the shear strain field which lead to spurious constraints in the thin beam limits. Indiscriminate use of reduced integration can introduce zero-energy modes and should therefore be used with caution. The reduced integration procedures are meaningful in the domain of computation of stiffness matrix only. Hence in the case of distributed static and inertial loadings, the use of fully integrated consistent load vector and consistent mass matrix with the under-integrated stiffness matrix, cannot be free of associated errors.

Use of consistent order of independent polynomial interpolation for the displacement fields participating in the definition of shear strain field eliminates shear locking. Typically, a quadratic interpolation for w_0 and a linear interpolation for θ will not produce any spurious terms in the shear strain field. However, use of quadratic polynomial for w_0 would demand a third (mid) node for its interpolation, increasing the number of nodal variables and the computational cost.

In the HSDT beam formulation, a cubic interpolation for w_0 and a linear interpolation for θ is employed. Hence, in the polynomial expression for transverse shear strain, an inconsistent *quadratic* term contributed by $w_0^{'}$ field will exist, which has no matching contribution of the same order from θ. As this inconsistent term in HSDT shear strain field is of higher order and hence weaker, the shear locking effects are insignificant. However, as the interpolation for section rotation (θ) is only linear, derivative of which forms the major component in the curvature strain field, the convergence characteristics are still not impressive. The convergence behaviour may be improved by introducing shear strain (γ_0) as a nodal degree of freedom and defining a section rotation as $(\gamma_0 - w_0^{'})$. However, use of γ_0, which is not an engineering degree of freedom, invites difficulties in the application of certain boundary conditions.

1.3.2 Issues related to accuracy

In general, the through-thickness distribution of *applied electric potential* in the actuator configuration and the *developed electric potential* in the sensor configuration of a piezoelectric beam is generally approximated as linear. In a piezoelectric beam under pure extension where the normal strain is uniform across the thickness, the linear assumption of through-thickness potential is appropriate. However, under bending deformations, the curvature strain causes the distribution of electric potential to be nonlinear across the thickness. The nonlinear part of the through-thickness distribution of electric potential is generally termed as the *induced potential*. The effect of induced potential is more significant when the piezoelectric material dominates the beam cross-section. In such cases, the use of linear polynomial to approximate the through-thickness distribution of electric potential will lead to inaccurate results. This phenomenon leading to inaccurate converged results, due to single layer modelling of transverse electric potential with linear approximation is termed here as *piezolocking*.

The conventional methods to relieve piezolocking and yield accurate results, taking the nonlinear nature of the induced potential into consideration are (i) use of sublayers in the mathematical modelling of the piezoelectric physical layer, leading to addition of sublayerwise nodal electric potential degrees of freedom and/or (ii) use of higher order polynomial interpolation for through-thickness electric potential field, leading to additional nodal electric potential degrees of freedom. Both methods would increase the computational effort and cost.

1.4 Scope for Research

Piezoelectric materials provide many advantages in the design of lightweight and controllable structures. Extension mode piezoelectric beams are extensively used in aerospace, defence, automotive structures. They offer the most reliable structural control with ease.

Numerical simulation using finite element method serves as a powerful tool for the analysis of the piezoelectric beam structures. Assessment of static, dynamic and stability characteristics of structures provides crucial information for efficient and optimized design. It will be highly beneficial to use computationally efficient, numerically wellbehaved and accurate finite elements for reliable analysis of piezoelectric structures.

ESL piezoelectric beam finite elements based on assumed displacements in the form of polynomial functions are very attractive and extensively used, by virtue of its simplicity. However, they are plagued by material-locking, shear-locking and piezolocking phenomena. Despite the existence of some techniques to circumvent these problems, it is worthwhile to put further efforts to look for more efficient methods of handling these locking effects.

It would be interesting to develop simple elements which, with their original polynomial displacement fields, perform consistently over a wide range of geometric and material parameters, without the requirements of any special technique to eliminate locking effects. Such finite elements would definitely have wider applications as they present more economic, reliable and accurate elements. Any investigation in this direction becomes very essential and significant in the context of ESL piezoelectric beam finite elements as they are widely used for the analysis of smart structures. In this regard, an extensive literature survey on the existing extension mode piezoelectric beam finite element formulations has been carried out.

CHAPTER 2

LITERATURE REVIEW

2.1 Introduction

In general, displacement-based finite element formulations for piezoelectric beams available in the literature, can be classified as:

- 3D solid models (Allik and Hughes, 1970; Tzou and Tseng, 1991, 1988; Ha et al., 1992; Koko et al., 1997; Duczek and Gabbert, 2013)
- Sandwich beam theory (Benjeddou et al., 1997, 2000; Raja et al., 2002, 2004),
- Layerwise beam theory (Robbins and Reddy, 1991; Saravanos and Heyliger, 1995; Donthireddy and Chandrashekhara, 1996; Ahmad et al., 2005; Plagianakos and Saravanos, 2005),
- Sinus beam model (Beheshti-Aval and Lezgy-Nazargah, 2010; Beheshti-Aval et al., 2011; Lezgy-Nazargah et al., 2013)
- Zig-zag beam model (Kapuria et al., 2004; Kapuria and Alam, 2006; Kapuria and Hagedorn, 2007)
- Global-Local beam theory (Beheshti-Aval and Lezgy-Nazargah, 2012, 2013) and
- Equivalent Single Layer (**ESL**) beam theories.

In line with the scope of the present investigation discussed in Chapter 1, the extensive literature survey reported here, places major emphasis on the **ESL** beam theory based *extension-mode* piezoelectric beam *analytical solutions* and *finite element formulations* with special attention to:

(i) The kind of assumed polynomial interpolation for displacement and electric potential fields in the longitudinal direction

(ii) Approximation for distribution of transverse electric potential in the piezoelectric layer

(iii) Locking phenomena and their effects

(iv) Methods of eliminating adverse effects of locking.

2.2 ESL-based Analytical Solutions for Piezoelectric Beams

Equivalent Single Layer (ESL) Euler-Bernoulli Theory (EBT) was used by Crawley and deLuis (1987), Crawley and Anderson (1990) and Abramovich and Pletner (1997) in their analytical formulations for analysis of piezoelectric beams. They considered the strain induced by the piezoelectric actuators as an equivalent applied mechanical force. Crawley and deLuis (1987) derived static and dynamic models for segmented piezoelectric actuators that are either bonded to an elastic substructure or embedded in a laminated composite. They discussed the optimal location for the actuator placement. The scaling analysis carried out by them, indicated that the nondimensional effectiveness of the piezoelectric actuator remains constant if the dimension of the piezoelectrics increase in scale with those of the structure. Crawley and Anderson (1990) extended these solutions to establish the range of parameters for which the simpler analytical solutions are valid. They proved the accuracy of the EBT based beam model to predict extensional and bending deformation. Abramovich and Pletner (1997) provided analytical solutions for induced axial strains and the curvature leading to the calculation of equivalent mechanical loads produced by piezoceramic actuators in a newly proposed sandwich structure.

ESL First-order Shear Deformation Theory (FSDT) which considers constant shear strain across the beam cross-section was used by Abramovich (1998); Krommer and Irschik (1999); Wang et al. (1999); Sun and Huang (2000); Huang and Sun (2001); Edery-Azulay and Abramovich (2004); Waisman and Abramovich (2002); Zhou et al. (2005) and Khdeir et al. (2012) for their analytical solutions for piezoelectric beams. Abramovich (1998) presented closed form solutions for the bending angle and the axial and lateral displacements along the beam for various configurations of lay-up, boundary conditions and mechanical loading. A closed-loop approach was then applied to control the lateral deflection of an axially loaded piezolaminated beam based on the measurement of the average bending slope. Edery-Azulay and Abramovich (2004) extended this formulation for parametric study of the effects of actuator location and number of patches on actuator's performance in various configurations and loading. Krommer and Irschik (1999) studied free transverse vibrations of smart beams using a Timoshenko based analytical formulation which considered the shear and rotary inertia. The effective stiffness parameters given by correction of electrical coupling, were used to study the influence of electric field on free vibration of beams. Wang et al. (1999) derived optimality conditions and analytical expressions based on FSDT for determining the optimal voltages to be applied to piezoelectric actuators so as to bend the beam in the desired shape. Sun and Huang (2000); Huang and Sun (2001) developed a FSDT-based electromechanical model for the active vibration control of smart composite beam structures with embedded piezoelectric actuators and sensors. The analytical model was developed using the displacement potential function and the transformation method of complex numbers. Waisman and Abramovich (2002) studied the active stiffening effects of the smart piezolaminated composite beams with a FSDT-based formulation. They evaluated the influence of actuator using the pin-force model. It is demonstrated that the stiffness of the beam can be actively altered using the piezoelectric bonded actuators, producing significant changes in the natural frequencies and mode shapes of the beam. Zhou et al. (2005) provided analytical solutions for piezoelectric bimorphs based on improved FSDT beam model. A general electric field function was proposed to reasonably approximate the through-the-thickness distribution of the applied and developed electric potentials. Khdeir et al. (2012) proposed FSDT-based analytical solution for the free vibration of cross-ply laminated beams with multiple distributed extension piezoelectric actuators, using the state space approach.

ESL Higher-order Shear Deformation Theory (HSDT) which considers the parabolic nature of transverse shear was used by Gaudenzi (1998); Aldraihem and Khdeir (2000); Khdeir and Aldraihem (2001); Aldraihem and Khdeir (2003) for their analytical formulations to study the behaviour of piezoelectric beams. Gaudenzi (1998) presented exact higher order solutions for simple adaptive structures for the cases of membrane actuation and pure bending. This formulation allows to evaluate the importance of higher order effects in the modelling of the interaction between induced strain actuators and a simple beam structure. Aldraihem and Khdeir (2000) presented analytical models and exact solutions for smart beam bending problem by using the state-space approach along with the Jordan canonical form. Khdeir and Aldraihem (2001) extended this formulation for smart beams with segmented actuators. They proved the validity of ESL theories for the analysis of extension mode smart beams. Aldraihem and Khdeir (2003) presented precise deflection models of beams with a number of pairs of piezoelectric patches and checked the performance of their previous formulation (Khdeir and Aldraihem, 2001), using various parametric studies.

2.3 ESL-based Piezoelectric Beam Finite Elements

2.3.1 EBT beam elements

The Euler-Bernoulli Theory (EBT) based piezoelectric beam finite elements neglect transverse shear deformation in their formulation, which can be reliably used for the analysis of slender beams. The two-noded EBT finite element essentially use a Hermite cubic interpolation for transverse displacement (w).

The EBT-based beam *bending* element was used by Hanagud et al. (1992); Gaudenzi et al. (2000); Stavroulakis et al. (2005) for vibration control studies with piezoelectric material. This element does not incorporate axial displacement in the formulation and has transverse displacement (w) and its derivative ($w^{'}$) as mechanical nodal degrees of freedom. Hanagud et al. (1992) used EBT-based beam bending element for the development of optimal active control procedures by minimizing a quadratic performance index of state and control vectors using output feedback for a flexible structure equipped with sensors and actuators. Gaudenzi et al. (2000) addressed vibration attenuation effects in active cantilever beams with position and velocity control approaches. The numerical simulation was performed using FEM with subsequent modal factorisation. Stavroulakis et al. (2005) used EBT beam bending element in the design of a vibration control mechanism for a beam with bonded piezoelectric sensors and actuators and an application of the arising smart structure for vibration suppression. These finite elements developed are without electric potential as a nodal degree of freedom and the piezoelectric effects were incorporated as the equivalent applied nodal forces.

The EBT-based piezoelectric beam *bending* finite element with a bilinear variation of potential in the piezoelectric layer was used by Zemcik and Sadilek (2007) and Sadilek and Zemcik (2010) for modal and frequency response analysis of piezoelectric beams, respectively. This formulation incorporated, apart from w and $w^{'}$, layerwise nodal electric potential degrees of freedom. Zemcik and Sadilek (2007) carried out the sensitivity analysis for the case of modal analysis of steel beam with and without applied piezoelectric patches. Sadilek and Zemcik (2010) carried out frequency response analysis of hybrid aluminium beam with piezoelectric actuators using the developed element. The piezoelectric actuators were driven by harmonic signals around the first eigen frequency and the beam oscillations were investigated.

The Euler-Bernoulli piezoelectric beam finite element with w, $w^{'}$ and u_0 as mechanical nodal degrees of freedom and a single electric potential degree of freedom for each piezoelectric layer was used by Carpenter (1997); Balamurugan and Narayanan (2001) and Kumar and Narayanan (2008). The axial deformation (u_0) was interpolated by a linear polynomial. They considered the developed/applied voltage constant over the surface of the piezoelectric layer and linear through the thickness. Carpenter (1997) used energy methods to derive beam finite elements for piezoelectric smart beams and obtained the EBT-based beam model as a special case. Balamurugan and Narayanan (2001) developed a finite element model based on the EBT for studying active vibration control of beam structures with distributed sensor and actuator layers, using different control strategies. Kumar and Narayanan (2008) discussed the strategy of determining the optimal location of piezoelectric sensor-actuator pairs in active vibration control of structures using the linear quadratic regulator (LQR) performance criterion, with the help of the EBT-based piezoelectric beam finite element formulation.

The EBT-based piezoelectric beam finite element with element-wise electric potential degree of freedom for each piezoelectric layer was developed by Bruant et al. (2001). They simulated the active vibration control of beam structures with piezoelectric actuators and sensors. A linear quadratic control method including a state observer was used to compute the control.

The EBT-based piezoelectric beam finite element with electric potential as a nodal degree of freedom for each piezoelectric layer was used by Bendary et al. (2010) for static and dynamic analysis of intelligent beam structures. They carried out various parametric studies of surface mounted piezoelectric beams.

2.3.2 FSDT beam elements

The FSDT-based two-noded beam bending element with Lagrange linear interpolations for transverse displacement (w) and section rotation (θ) was used by Foutsitzi et al. (2002, 2003) to study vibration control of a beam with bonded piezoelectric sensors and actuators using optimal LQR control strategy and H_2 controller, respectively. The piezoelectric effect was introduced through equivalent applied nodal forces and electric potential is not a nodal degree of freedom. They assumed a linear through-thickness potential distribution.

The FSDT-based two-noded beam bending formulation with interdependent interpolations for w and θ was used by (Aldraihem et al., 1996, 1997; Moutsopoulou et al., 2012, 2013) for their studies on vibration control using piezoelectric smart beams. These interpolations were originally derived by Friedman and Kosmatka (1993) based on the governing equations for conventional/composite materials. The electric potential was not considered as a nodal degree of freedom and the piezoelectric actuation was incorporated in terms of equivalent mechanical load and sensing voltage was calculated from the derived quantities. Aldraihem et al. (1996, 1997) compared EBT and FSDT smart beam *bending* finite elements for distributed control of laminated beams. They reported that use of an EBT based controller to suppress beam vibration can lead to instability caused by inadvertent excitation of unmodelled modes and recommended use of FSDT. Moutsopoulou et al. (2012) presented modelling and numerical analysis of piezoelectric systems and smart structures with embedded control. Moutsopoulou et al. (2013) studied active control of piezoelectric smart structures in vibration and noise attenuation applications with the FSDT-based finite element model.

The FSDT-based two-noded beam bending formulation with interdependent interpolations for w and θ and a single electric potential degree of freedom for each piezoelectric layer was used by Bona et al. (1994) for the analysis of structures with embedded piezoelectric sensors/actuators. The electric potential was considered linearly varying across the thickness of piezoelectric layer.

The FSDT-based two-noded beam bending formulation with interdependent interpolations for w and θ and element-wise electric potential degree of freedom for each piezoelectric layer was used by Manjunath and Bandyopadhyay (2006) for study of vibration control. They discussed on the smallest magnitude of the control effort required to control the vibrations of the smart cantilever beam with surface bonded piezoelectric patches.

The isoparametric FSDT-based two-noded piezoelectric beam element with Lagrange linear interpolations for u_0, w and θ was used by Sedaghati et al. (2006) to develop a design optimization methodology. The electric potential was not considered as a nodal degree of freedom and the piezoelectric effect was introduced by means of equivalent nodal forces. They combined the finite element model and the sequential quadratic programming technique to improve the structural performance of laminated composite beams with piezoelectric actuators.

The isoparametric FSDT-based two-noded piezoelectric beam finite element with Lagrange linear interpolations for u_0, w and θ and layerwise nodal electric potential degrees of freedom was used by Narayanan and Balamurugan (2003) to study active vibration control of piezolaminated smart structures using distributed sensors and actuators. They employed a layerwise assumed linear through-thickness potential.

Three-noded FSDT piezoelectric beam elements based on higher-order interpolations for mechanical field variables were developed by Ray and Mallik (2004); Blandford et al. (1999); Neto et al. (2009) for the analysis of piezoelectric beams. However, all these formulations used only linear interpolation of through-thickness electric potential.

2.3.3 HSDT beam elements

The Reddy's HSDT incorporates the accurate parabolic distribution of through-thickness shear strain. Finite elements with Reddy's usual displacement field use assumed Lagrange linear interpolation for axial displacement (u_0) and section rotation (θ) and Hermite cubic interpolation for transverse displacement (w_0). This form of HSDT was used by Chandrashekhara and Varadarajan (1997), Peng et al. (1998), Komeili et al. (2011) and Elshafei and Alraiess (2013) for their piezoelectric beam formulation with a layerwise linear through-thickness potential. Chandrashekhara and Varadarajan (1997) presented numerical results from HSDT-based finite element to demonstrate the effectiveness of piezoelectric actuators and position sensors for adaptive shape control.

The model is without electrical nodal degrees of freedom and the piezoelectric effect is brought in through equivalent nodal forces. Peng et al. (1998) developed a finite element model for the active position control and vibration control of composite beams with distributed piezoelectric sensors and actuators. This model used equivalent forces generated by the electric potential applied to the actuator in the calculation. Komeili et al. (2011) used the HSDT-based finite element as well as analytical solutions by Fourier series, for static analysis of functionally graded piezoelectric material (FGPM) beams under thermo-electro-mechanical loads. Equivalent nodal forces were incorporated to bring in the piezoelectric effect. Elshafei and Alraiess (2013) used the HSDT-based finite element for static analysis of piezoelectric smart beams with layerwise nodal electric potential degrees of freedom. The formulation is validated by comparing the results for various parametric studies with standard solutions.

A modified form of Reddy's HSDT displacement field with shear angle (γ_0) as a variable instead of section rotation (θ) in the description of displacement field was used by Chee et al. (1999). This improved the curvature representation and the element convergence characteristic. This model considered nodal electric potential degrees of freedom with layerwise linear through-thickness distribution. In some cases they used sublayers within piezolayer and sublayer-wise linear through-thickness potential. Wang et al. (2007) and Jiang and Li (2007) used a modified form of HSDT given by Chee et al. (1999) with an assumed layerwise cubic function to approximate the higher-order through-thickness potential. The potential difference between top and bottom surfaces (V), electric fields at top and bottom surfaces (E_b and E_t) were used as electrical degrees of freedom. The E_b and E_t were statically condensed out to reduce the size of the global finite element matrices.

2.4 Modelling of Through-thickness Potential

Most of the finite elements available in the literature used an assumed distribution of through-thickness potential with various orders of interpolation (linear, quadratic and cubic). Wang (2004) studied the effect of higher-order through-thickness potential on the accuracy of the piezoelectric finite element solutions, with the help of sublayered modelling in which the sublayerwise linear interpolation for through-thickness potential was employed. Sze et al. (2004) carried out the review of the assumptions used for electric variables in the piezoelectric analysis with a FSDT-based plate model. They compared results from constant electric field (EC), linear electric field (EL) and constant electric displacement (DC) models for piezoelectric laminates in their numerical study. Rachmadini et al. (2005) tested the effect of full coupling stiffness on the through-thickness electric potential distribution in the piezoelectric actuator/sensor using their earlier three dimensional finite element developed in Lee et al. (2004).

2.5 2D FE Simulation Results as Benchmark

The literature survey reveals the concepts and methodology adopted by various researchers for developing new piezoelectric beam finite element formulations. In the context of studying beam bending, shear and extension, the deformations in the 2-dimensional (longitudinal:X and transverse:Z) plane are essentially addressed. The loading and deformations are limited to the XZ plane. For validation of such beam formulations, many researchers (Zhang and Sun, 1996; Kapuria et al., 2004; Kapuria and Alam, 2006; Wang et al., 2007) have used results from the analysis of the corresponding two-dimensional geometry, modelled by appropriate piezoelectric 2D finite elements as a benchmark. Finite element analysis using a refined 2D mesh is able to extract the exact variation of the field variables in the longitudinal and transverse directions. This approach would reveal the efficacy and adequacy of the beam formulations in extracting the *two*-dimensional structural behaviour using the *one*-dimensional (beam) finite element. Lin et al. (1994) verified in detail, the use of ANSYS 2D finite element simulations as benchmark for validating both static and dynamic analyses results of piezoelectric extension mode smart beam formulations.

2.6 Summary of Literature Survey

Piezoelectric smart structures are dominating the shape and vibration control technologies. Many numerical models are available in the literature for modeling the piezoelectric smart structures, depending on their application. The selection of a particular model depends on the complexity of the structural behaviour to be modelled. The exact or analytical solutions are suitable for simple and regular geometries. Ability to handle geometric and loading complexities have made the finite element analysis a most preferred numerical tool for the structural analysis of the piezoelectric smart systems. Numerous piezoelectric finite elements based on different theories are available in the literature. ESL theories are mostly preferred in the literature for piezoelectric beams by virtue of their simplicity and adaptability. The specific observations from the literature survey are summarised here for each ESL beam theory:

- EBT:
  - The conventional two-noded EBT-based piezoelectric beam element uses independent Lagrange linear interpolations for both axial displacement (u_0) and electric potential (φ) and Hermite cubic interpolation for transverse displacement (w_0).
  - As the field interpolations are independent, the inherent coupling between mechanical and electrical field variables is accommodated only through constitutive relations.
  - The material locking effects in EBT-based piezoelectric beam finite elements due to material asymmetry are not addressed.
  - An assumed linear through-thickness distribution of electric potential is widely used. The piezolocking effects of higher-order induced potential are not addressed.
- FSDT:
  - The conventional two-noded isoparametric FSDT-based piezoelectric beam element uses independent Lagrange interpolations for axial displacement (u_0), transverse displacement (w_0), section rotation (θ) and electric potential (φ).
  - As the field interpolations are independent, the inherent coupling between mechanical and electrical field variables is accommodated only through constitutive relations.
  - Shear locking has been generally eliminated by the use of Reduced Integration technique. Some researchers used interdependent interpolations for w_0 and θ, which relieved shear locking and improved the performance.

  - The material locking effects in FSDT-based piezoelectric beam finite elements due to material asymmetry are not addressed.
  - The through-thickness distribution of electric potential has been approximated as linear. Some researchers suggested use of sublayered modelling to accommodate the higher order induced potential effects.

- HSDT:
  - The conventional two-noded piezoelectric beam element based on Reddy's HSDT uses Lagrange linear interpolations for axial displacement (u_0), section rotation (θ) and electric potential (φ) and Hermite cubic interpolation for transverse displacement (w_0).
  - As the field interpolations are independent, the coupling between mechanical and electrical field variables is accommodated only through constitutive relations.
  - Use of shear angle (γ_0) as a variable instead of section rotation (θ) improves the bending behaviour of the HSDT-based elements.
  - The material locking effects in HSDT-based piezoelectric beam finite elements due to material asymmetry are not addressed.
  - An assumed linear approximation for through-thickness potential is applied by most of the researchers. Some of the researchers used assumed cubic variation of through-thickness potential and sublayered modelling to accommodate the effects of higher-order induced potential.

ANSYS 2D finite element simulations can be effectively used to obtain a set of reference values to validate the newly developed piezoelectric beam finite elements.

2.7 Motivation and Objective of the Thesis

It is observed from the review of the literature that delayed convergence due to shear locking and material locking and loss of accuracy due to piezolocking are the main factors which affects the performance of conventional displacement based ESL beam finite elements employed for the analysis of extension mode piezoelectric smart beams.

The literature review also indicates that in the displacement based finite element formulations, the nature of *assumed interpolation polynomials* has a direct influence on the basic performance characteristics of the element.

A basic cause for the above mentioned deficiencies can be attributed to the coupling among the various participating fields. Material locking is the outcome of coupling between axial and bending deformations of the beam which is termed as 'bending-extension' coupling. The shear locking is the outcome of 'bending-shear' coupling by virtue of shear strain definition in the respective formulation. The 'piezolocking' due to the nonlinear nature of the induced potential arises from coupling between electric potential and flexural strain. In the case of piezoelectric beam finite elements, these couplings are governed by the coefficients of the coupled constitutive matrix relating the mechanical and electrical quantities.

In the domain of assumed polynomial displacement based finite element procedures, the apparently competitive ways of overcoming the above locking problems in the piezoelectric beam finite elements are (i) use of higher order polynomials for interpolation of displacements and through-thickness electric potential or (ii) use of refined descretization in the axial direction for mechanical field variables and in the thickness direction (by means of sublayered modelling) for electric potential. However, these methods are computationally expensive.

A more natural and economical way to tackle these problems seems to be the incorporation of an inherent coupling among the assumed polynomial fields, consistent with element kinematics. A natural and reliable source for bringing in such coupling is obviously the element equilibrium equations, which can be used for deriving a set of coupled polynomial approximations for the participating fields. The investigation reported in this thesis is a humble attempt in this direction.

The main objective of the present investigations are as follows:

- Development of ESL-based EBT, FSDT and HSDT extension mode piezoelectric smart beam finite elements using coupled polynomial fields, which involves:
    1. Formulation of element kinematics.
    2. Derivation of governing equations with the help of a variational formulation.

3. Derivation of coupled polynomial interpolations for the displacement and electric potential field variables which incorporate all the field couplings at the interpolation level itself.
4. Application of the derived field interpolations for the proposed beam finite elements.
5. Validation of the finite elemets by applying it to numerical test problems of static and free vibration analyses.
6. Critical evaluation of the elements by comparing its performance with the conventional finite elements, in terms of accuracy and computational efficiency.

2.8 Organization of the Thesis

In additional to *Chapter 1 Introduction* which presents basic ideas about extension mode piezoelectric smart beams and issues related with their finite element modelling and *Chapter 2 Literature Review* which provides the extensive review and objective of the research, the thesis contains four more chapters.

The *Chapter 3* develops the coupled polynomial interpolations for ESL EBT-based extension mode piezoelectric beam finite element with a layerwise consistent through-thickness potential. The proposed EBT-*Coupled* formulation is validated with numerical test problems.

The *Chapter 4* develops the coupled polynomial interpolations for ESL FSDT-based extension mode piezoelectric beam finite element with a layerwise consistent through-thickness potential. The proposed FSDT-*Coupled* formulation is validated with numerical test problems.

The *Chapter 5* develops the coupled polynomial interpolations for ESL HSDT-based extension mode piezoelectric beam finite element with a layerwise consistent through-thickness potential. The proposed HSDT-*Coupled* formulation is validated with numerical test problems.

The *Chapter 6* contains the major conclusions from the present investigation. Conclusions have been derived with respect to the performance of the coupled polynomial interpolations in terms of accuracy and computational economy. A brief outline of work for future investigation is also given.

References arranged in alphabetical order are presented at the end of the thesis.

CHAPTER 3

COUPLED EBT PIEZOELECTRIC BEAM FINITE ELEMENT

3.1 Introduction

In this chapter, coupled polynomial interpolations are proposed for ESL-EBT (Equivalent Single Layer Euler-Bernoulli Theory) based piezoelectric beam formulation. The conventional EBT-based piezoelectric beam element suffers from *loss of accuracy* due to piezolocking and *slow convergence* due to material locking.

Piezolocking arises from the use of linear approximation to model the nonlinear nature of the through-thickness potential. The effect of piezolocking tends to be more significant when the piezoelectric material dominates the beam cross-section. The conventional EBT-based piezoelectric beam finite element formulations employ linear polynomial to approximate the through-thickness potential and hence converge to inaccurate results, in spite of finite element refinement in the longitudinal direction of the beam. Therefore, conventional formulations demand either the use of higher-order approximation for through-thickness potential or the use of sublayers in the mathematical formulation of the piezoelectric layer with electric potential as a degree of freedom at each interface between sublayers. In any case, it increases the number of nodal degrees of freedom and the computational effort. A coupled consistent potential derived from the electrostatic equilibrium equation is used here in the present formulation to eliminate piezolocking, without increasing the number of nodal degrees of freedom. Use of the consistent potential interpolation is shown to improve and consistently maintain the accuracy of results, irrespective of the proportion of piezoelectric material in the beam cross-section.

Material locking arises from the activation of bending-extension coupling due to asymmetric distribution of material over the beam cross-section. The conventional EBT-based piezoelectric beam finite element which uses linear interpolation of axial displacement exhibits poor convergence of solutions, when the beam cross-section is asymmetric. Hence, the conventional formulations demand the use of a more number of elements or the use of higher order polynomial interpolation of axial displacement, to yield converged solutions. In the present formulation, a coupled quadratic polynomial for axial displacement of the beam is derived from the governing equilibrium equations obtained using the variational formulation. The polynomial expression for axial displacement of the beam contains a quadratic coupled term with contributions from an assumed cubic polynomial for transverse displacement and linear polynomials for layerwise electric potentials.

The shape functions derived using the coupled polynomials for through-thickness electric potential and the axial displacement handle the induced potential coupling and the bending-extension coupling in a variationally consistent manner. The comparison of results from numerical experiments proves the improved performance of the present coupled polynomial based formulation over the conventional formulations.

3.2 Theoretical Formulation

The present formulation is based on the equivalent single layer (ESL) Euler-Bernoulli theory (EBT) for mechanical field and a layerwise model for electric potential (φ). A multilayered piezoelectric smart beam is considered, as shown in Fig. 3.1. The layer(s) can be host layers of conventional/composite material or bonded/embedded layer(s) of piezoelectric material. The beam layers are assumed to be made up of isotropic or specially orthotropic materials, with perfect bonding between them. The top and bottom faces of the piezoelectric layers are fully covered with electrodes. The mechanical and electrical quantities are assumed to be small enough to apply linear theories of elasticity and piezoelectricity.

3.2.1 Mechanical displacements and strain

The displacement field expressions for EBT are given as (Bendary et al., 2010):

$$u(x,z) = u_0(x) - zw_0'(x) \tag{3.1}$$

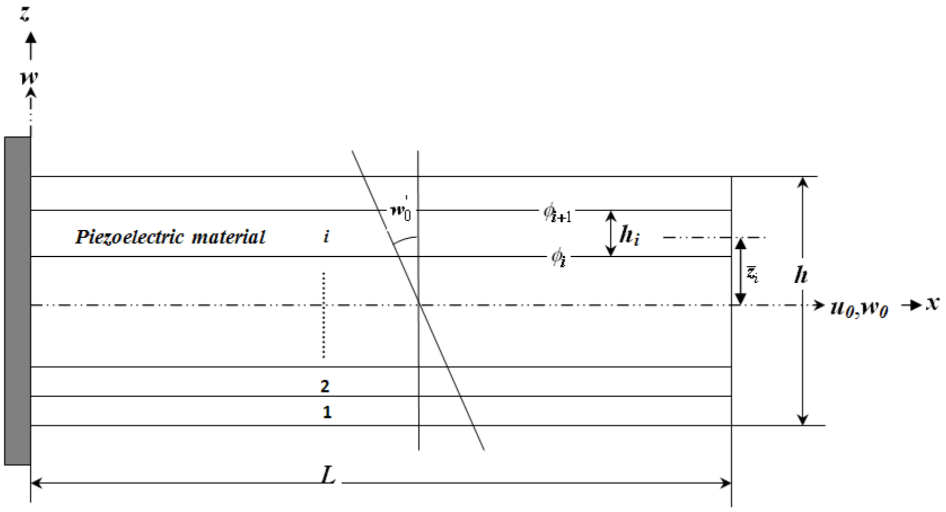

Figure 3.1: EBT formulation: Geometry of a general multilayered extension mode piezoelectric smart beam.

$$w(x,z) = w_0(x) \tag{3.2}$$

where $()'$ denotes $\mathrm{d}/\mathrm{d}x$. $u(x,z)$ and $w(x,z)$ are the displacements in the longitudinal and transverse directions, respectively. The sub-functions $u_0(x)$ and $w_0(x)$ are the longitudinal and transverse displacements at the centroidal axis of the beam, respectively. L, b and h are the length, width and the total thickness of the structure, respectively.

Substituting Eqs. (3.1) and (3.2) in the usual strain-displacement relations, the following expression for axial strain is obtained:

$$\varepsilon_x(x,z) = \frac{\partial u(x,z)}{\partial x} = u_0'(x) - z w_0''(x) \tag{3.3}$$

3.2.2 Electric potential and electric field

The layerwise through-thickness distribution of the electric potential is assumed as shown in Fig. 3.1. The two dimensional electric potential of the i^{th} piezoelectric layer $\varphi_i(x,z)$, takes the values of $\phi_{i+1}(x)$ and $\phi_i(x)$ at the top and bottom surfaces of the piezoelectric layer with thickness h_i, respectively. The electric field in the transverse (z) direction is derived from the electric potential as (Benjeddou et al., 1997):

$$E_z^i(x,z) = -\frac{\partial \varphi_i(x,z)}{\partial z} \tag{3.4}$$

3.2.3 Constitutive relations

The reduced constitutive relations for EBT-based piezoelectric beam formulation are given as (Appendix A):

$$\begin{bmatrix} \sigma_x^k \\ D_z^i \end{bmatrix} = \begin{bmatrix} \tilde{Q}_{11}^k & -\tilde{e}_{31}^i \\ \tilde{e}_{31}^i & \tilde{\epsilon}_3^i \end{bmatrix} \begin{bmatrix} \varepsilon_x \\ E_z^i \end{bmatrix} \tag{3.5}$$

where (i=1....number of piezoelectric layers in beam) and (k=1....total number of layers in beam).

3.3 Derivation of Potential Consistent with EBT

For the free volumic charge density assumption, the electrostatic equilibrium equation of the i^{th} piezoelectric layer reduces to (Benjeddou et al., 1997):

$$\frac{\partial D_z^i(x,z)}{\partial z} = 0 \tag{3.6}$$

as $D_x^i = D_y^i = 0$ form Eq. (3.5).

Using Eqs. (3.3), (3.4), (3.5) and (3.6), we get:

$$\frac{\partial^2 \varphi_i(x,z)}{\partial z^2} = -\frac{\tilde{e}_{31}^i}{\tilde{\epsilon}_3^i} w_0^{''}(x) \tag{3.7}$$

On solving Eq. (3.7), we have:

$$\varphi_i(x,z) = -\frac{\tilde{e}_{31}^i}{\tilde{\epsilon}_3^i}\frac{z^2}{2} w_0^{''}(x) + C_1^i(x)z + C_2^i(x) \tag{3.8}$$

where, C_1^i and C_2^i are the constants to be obtained from boundary conditions for φ_i in z-direction. For i^{th} piezolayer boundary conditions are $\varphi_{z=z_i}(x,z) = \phi_i(x)$ and $\varphi_{z=z_{i+1}}(x,z) = \phi_{i+1}(x)$. After solving Eq. (3.8) and simplifying, we get (Benjeddou et al., 1997):

$$\varphi_i(x,z) = \bar{\varphi}_i(x) + \left(\frac{z-\bar{z}_i}{h_i}\right)\tilde{\varphi}_i(x) + \frac{1}{2}\left[\left(\frac{h_i}{2}\right)^2 - (z-\bar{z}_i)^2\right]\frac{\tilde{e}_{31}^i}{\tilde{\epsilon}_3^i} w_0^{''}(x) \tag{3.9}$$

where $\bar{\varphi}_i = \left(\phi_{i+1} + \phi_i\right)/2; \qquad \tilde{\varphi}_i = \left(\phi_{i+1} - \phi_i\right); \qquad \bar{z}_i = (z_{i+1} + z_i)/2$

From Eq. (3.9), it is clear that the potential distribution consistent with the EBT is quadratic in the transverse direction. The first two terms describe the conventional linear part in which $\bar{\varphi}$ and $\tilde{\varphi}$ are the mean and difference of potentials on the top and bottom faces of the i^{th} piezoelectric layer, respectively. The third term which is quadratic denotes the bending strain contribution to the potential. This nonlinear term constitutes the induced potential and plays an important role in the formulation, as it changes the stiffness of the structure. The induced potential depends on the geometrical location along transverse direction $(\bar{z}_i)$ and $(\tilde{e}^i_{31}/\tilde{\epsilon}^i_3)$ ratio.

The transverse electric field is derived from Eq. (3.9) as:

$$E^i_z(x,z) = -\frac{\partial\varphi_i(x,z)}{\partial z} = -\frac{\tilde{\varphi}_i(x)}{h_i} + \frac{\tilde{e}^i_{31}}{\tilde{\epsilon}^i_3}\left(z - \bar{z}_i\right) w_0^{''}(x) \tag{3.10}$$

3.4 Variational Formulation

Hamilton's principle is used to formulate the smart beam. It is expressed as (Chee et al., 1999):

$$\delta \int_{t_1}^{t_2} (K - H + W)dt = \int_{t_1}^{t_2} (\delta K - \delta H + \delta W)dt = 0 \tag{3.11}$$

where *K* is the kinetic energy, *H* is the electric enthalpy density function for the piezoelectric material and the mechanical strain energy for the linear elastic material and *W* is the work done by external forces.

3.4.1 Variation of electromechanical/strain energy

For the j^{th} conventional material layer, the variation of mechanical strain energy is written as:

$$\delta H_j = \int_V \left(\sigma^j_x \delta\varepsilon^j_x\right) dV \tag{3.12}$$

The electromechanical energy variation of the i^{th} piezoelectric layer is given by (Chee et al., 1999):

$$\delta H_i = \int_V \left(\sigma^i_x \delta\varepsilon^i_x - D^i_z \delta E^i_z\right) dV \tag{3.13}$$

Substituting values of axial strain (ε_x), electric field (E_z) from Eqs. (3.3), (3.10) and using them along with constitutive relations given by Eq. (3.5) in expressions (3.12) and (3.13), the total variation on the potential energy of the smart beam is given as:

$$\begin{aligned}\int_{t_1}^{t_2} \delta H dt = \int_{t_1}^{t_2} \int_x \Bigg\{ & \delta u_0^{'} \begin{pmatrix} (\tilde{Q}_{11}^k I_0^k) u_0^{'} - \left[\tilde{Q}_{11}^k I_1^k + ((\tilde{e}_{31}^i)^2/\tilde{\epsilon}_3^i)\,(I_1^i - I_0^i \bar{z}_i)\right] w_0^{''} \\ + (\tilde{e}_{31}^i I_0^i/h_i)\,\tilde{\varphi}_i \end{pmatrix} + \\ & \delta w_0^{''} \begin{pmatrix} -\left[\tilde{Q}_{11}^k I_1^k + ((\tilde{e}_{31}^i)^2/\tilde{\epsilon}_3^i)\,(I_1^i - I_0^i \bar{z}_i)\right] u_0^{'} \\ + \left[\tilde{Q}_{11}^k I_2^k + ((\tilde{e}_{31}^i)^2/\tilde{\epsilon}_3^i)\,(I_2^i - I_0^i \bar{z}_i^2)\right] w_0^{''} \\ -(\tilde{e}_{31}^i I_0^i \bar{z}_i/h_i)\,\tilde{\varphi}_i \end{pmatrix} + \\ & \delta\tilde{\varphi}_i \Big((\tilde{e}_{31}^i I_0^i/h_i)\,u_0^{'} - (\tilde{e}_{31}^i I_0^i \bar{z}_i/h_i)\,w_0^{''} - (\tilde{\epsilon}_3^i I_0^i/(h_i)^2)\,\tilde{\varphi}_i \Big) \Bigg\} dxdt \end{aligned} \tag{3.14}$$

where (i=1....number of piezoelectric layers in the beam); (k=1....total number of layers in the beam) and $I_q^k = b\left(z_{k+1}^{q+1} - z_k^{q+1}\right)/(q+1)$.

3.4.2 Variation of kinetic energy

Electrical variables do not enter into the expression for kinetic energy, which is given as (Chee et al., 1999):

$$K = \frac{1}{2} b \int_x \int_{z_k}^{z_{k+1}} \rho_k \left(\dot{u}^2 + \dot{w}^2\right) dzdx \tag{3.15}$$

where ρ_k is the mass density of k^{th} layer in kg/m^3 and (k=1....total number of layers in the beam). Substituting values of u and w from Eqs. (3.1) and (3.2) and applying variation to get:

$$\begin{aligned}\int_{t_1}^{t_2} \delta K dt = -\rho_k \int_{t_1}^{t_2} \int_x \Big\{ & \delta u_0 \left(I_0^k \ddot{u}_0 - I_1^k \ddot{w}_0^{'}\right) + \delta w_0^{'} \left(-I_1^k \ddot{u}_0 + I_2^k \ddot{w}_0^{'}\right) \\ & + \delta w_0 \left(I_0^k \ddot{w}_0\right) \Big\} dxdt \end{aligned} \tag{3.16}$$

where $\dot{()}$ denotes $\partial/\partial t$.

3.4.3 Variation of the work of external forces

The total virtual work on the structure can be defined as the product of the virtual displacements with forces for the mechanical work and the product of the virtual electric potential with the charges for the electrical work. The variation of the total work done by the external mechanical and electrical loading is given as (Chee et al., 1999):

$$\begin{aligned}\int_{t_1}^{t_2} \delta W dt = \int_{t_1}^{t_2} \Big\{ & \textstyle\int_V (\delta u f_u^v + \delta w f_w^v) dV + \int_S (\delta u f_u^s + \delta w f_w^s) dS \\ & + \textstyle\sum (\delta u f_u^c + \delta w f_w^c) - \int_{S_\varphi} \delta \varphi q_0 dS_\varphi \Big\} dt \end{aligned} \tag{3.17}$$

in which f^v,f^s,f^c are volume, surface, point forces, respectively; q_0 and S_φ are the surface charges and area on which charge is applied.

3.5 Derivation of Coupled Field Relations

The relationship between the field variables is established here with the help of governing equilibrium equations. For static condition without any external loading, the variational principle given in Eq. (3.11) reduces to:

$$\delta H = 0 \tag{3.18}$$

We apply a variation to the basic variables to get static equilibrium equations from expression (3.14) as:

$$\delta u_0 : \begin{pmatrix} -(\tilde{Q}_{11}^k I_0^k) u_0^{''} + \left[\tilde{Q}_{11}^k I_1^k + ((\tilde{e}_{31}^i)^2 / \tilde{\epsilon}_3^i) \, (I_1^i - I_0^i \bar{z}_i) \right] w_0^{'''} \\ - (\tilde{e}_{31}^i I_0^i / h_i) \, \tilde{\varphi}_i^{'} \end{pmatrix} = 0 \tag{3.19}$$

$$\delta w_0 : \begin{pmatrix} - \left[\tilde{Q}_{11}^k I_1^k + ((\tilde{e}_{31}^i)^2 / \tilde{\epsilon}_3^i) \, (I_1^i - I_0^i \bar{z}_i) \right] u_0^{'''} \\ + \left[\tilde{Q}_{11}^k I_2^k + ((\tilde{e}_{31}^i)^2 / \tilde{\epsilon}_3^i) \, (I_2^i - I_0^i \bar{z}_i^2) \right] w_0^{''''} \\ - (\tilde{e}_{31}^i I_0^i \bar{z}_i / h_i) \, \tilde{\varphi}_i^{''} \end{pmatrix} = 0 \tag{3.20}$$

From Eq. (3.19), we can write the relationship between axial displacement (u_0), total transverse displacement (w_0) and electric potential (φ_i) as:

$$u_0^{''} = \beta_1^u w_0^{'''} + \beta_2^{ui} \tilde{\varphi}_i^{'} \tag{3.21}$$

where $\beta_1^u = \left[\tilde{Q}_{11}^k I_1^k + ((\tilde{e}_{31}^i)^2/\tilde{\epsilon}_3^i)\,(I_1^i - I_0^i \bar{z}_i)\right]/(\tilde{Q}_{11}^k I_0^k)$ and $\beta_2^{ui} = -\,(\tilde{e}_{31}^i I_0^i/h_i)\,/(\tilde{Q}_{11}^k I_0^k)$. The constants $\beta_m^u \quad (m = 1, 2)$ which relate the field variables, are functions of geometric and material properties of the beam. It is noteworthy that their values depend on intensity of bending-extension coupling and induced potential coupling. This relation is used in the next section, to derive coupled polynomials for the interpolation of the field variables.

3.6 Finite Element Formulation

Using the variational formulation described above, a finite element model is developed here. The model consists of two mechanical variables (u_0 and w_0) and layerwise electrical variables ($\tilde{\varphi}_i$) where (i=1.....number of piezoelectric layers in the beam).

In terms of natural coordinate (ξ), a cubic polynomial for transverse displacement (w_0) and linear polynomials for layerwise electric potentials ($\tilde{\varphi}_i$) are assumed as given in Eqs. (3.22a) and (3.22b), respectively. The transformation between coordinate ξ and global coordinate (x) along the length of the beam is given as $\xi = [2(x - x_1)/(x_2 - x_1)] - 1$ and $x_2 - x_1 = l$, length of the beam element.

$$w_0 = b_0 + b_1\xi + b_2\xi^2 + b_3\xi^3 \tag{3.22a}$$

$$\tilde{\varphi}_i = c_0^i + c_1^i \xi \tag{3.22b}$$

Using these polynomials for w_0 and $\tilde{\varphi}_i$ in Eq. (3.21) and integrating with respect to ξ, we get the coupled polynomial for midplane axial displacement (u_0) as:

$$u_0 = [(6\beta_1^u/l)b_3 + (\beta_2^{ui} l/4)c_1^i]\xi^2 + a_1\xi + a_0 \tag{3.23}$$

It is noteworthy that the polynomial approximation for u_0 given by Eq. (3.23) contains, in addition to the conventional linear polynomial terms, a coupled quadratic term which takes care of the bending-extension coupling and induced potential couplings at field interpolation level itself. As seen from Eqs. (3.22a), (3.22b) and (3.23), while employing this quadratic polynomial for interpolation of axial displacement, the generalized degrees of freedom are maintained the same as that of the conventional formulation. Hence, no additional nodal degrees of freedom are introduced. Using Eqs. (3.22a), (3.22b) and (3.23), the coupled shape functions in Eq. (3.24) are derived by usual method.

$$\begin{Bmatrix} u_0 \\ w_0 \\ w_0^{'} \\ \tilde{\varphi}_i \end{Bmatrix} = \begin{bmatrix} N_1^u & N_2^u & N_3^u & N_4^{ui} & N_5^u & N_6^u & N_7^u & N_8^{ui} \\ 0 & N_1^w & N_2^w & 0 & 0 & N_3^w & N_4^w & 0 \\ 0 & N_1^{w'} & N_2^{w'} & 0 & 0 & N_3^{w'} & N_4^{w'} & 0 \\ 0 & 0 & 0 & N_1^{\varphi i} & 0 & 0 & 0 & N_2^{\varphi i} \end{bmatrix} \begin{Bmatrix} u_0^1 \\ w_0^1 \\ w_0^{'1} \\ \tilde{\varphi}_i^1 \\ u_0^2 \\ w_0^2 \\ w_0^{'2} \\ \tilde{\varphi}_i^2 \end{Bmatrix} \tag{3.24}$$

The expressions for these shape functions in the natural coordinate system are given as:

$$\begin{aligned}
&N_1^u = \frac{(1-\xi)}{2}; \quad N_2^u = \frac{3\beta_1^u}{2l}(\xi^2-1); \quad N_3^u = \frac{3\beta_1^u}{4}(\xi^2-1); \quad N_4^{ui} = \frac{\beta_2^{ui} l}{8}(1-\xi^2); \\
&N_5^u = \frac{(1+\xi)}{2}; \quad N_6^u = \frac{3\beta_1^u}{2l}(1-\xi^2); \quad N_7^u = \frac{3\beta_1^u}{4}(\xi^2-1); \quad N_8^{ui} = \frac{\beta_2^{ui} l}{8}(\xi^2-1); \\
&N_1^w = \frac{\xi}{4}(\xi^2-3)+\frac{1}{2}; \quad N_2^w = \frac{l}{8}(\xi^3-\xi^2-\xi+1); \\
&N_3^w = \frac{\xi}{4}(3-\xi^2)+\frac{1}{2}; \quad N_4^w = \frac{l}{8}(\xi^3+\xi^2-\xi-1); \\
&N_1^{w'} = \frac{3}{2l}(\xi^2-1); \quad N_2^{w'} = \frac{\xi}{2}\left(\frac{3\xi}{2}-1\right)-\frac{1}{4}; \\
&N_3^{w'} = \frac{3}{2l}(1-\xi^2); \quad N_4^{w'} = \frac{\xi}{2}\left(\frac{3\xi}{2}+1\right)-\frac{1}{4}; \\
&N_1^{\varphi i} = \frac{(1-\xi)}{2}; \quad N_2^{\varphi i} = \frac{(1+\xi)}{2}.
\end{aligned}$$

Now, the variation on the basic mechanical and electrical variables can be transferred to the nodal degrees of freedom. Substituting the shape functions from Eq. (3.24) in Eqs. (3.14), (3.16), (3.17) and using Eq. (3.11), we get the descretized from of finite element equations as:

$$\begin{bmatrix} \begin{bmatrix} M \end{bmatrix} & 0 \\ 0 & 0 \end{bmatrix} \begin{bmatrix} \begin{Bmatrix} \ddot{U} \end{Bmatrix} \\ \begin{Bmatrix} \ddot{\Phi} \end{Bmatrix} \end{bmatrix} + \begin{bmatrix} \begin{bmatrix} K_{uu} \end{bmatrix} & \begin{bmatrix} K_{u\varphi} \end{bmatrix} \\ \begin{bmatrix} K_{\varphi u} \end{bmatrix} & \begin{bmatrix} K_{\varphi\varphi} \end{bmatrix} \end{bmatrix} \begin{bmatrix} \begin{Bmatrix} U \end{Bmatrix} \\ \begin{Bmatrix} \Phi \end{Bmatrix} \end{bmatrix} = \begin{bmatrix} \begin{Bmatrix} F \end{Bmatrix} \\ \begin{Bmatrix} Q \end{Bmatrix} \end{bmatrix} \tag{3.25}$$

where M is the mass matrix. $K_{uu}, K_{u\varphi}, K_{\varphi u}, K_{\varphi\varphi}$ are the global stiffness sub-matrices. U, Φ are the global mechanical and electrical nodal degrees of freedom vectors, respectively. F, Q are global mechanical and electrical nodal force vectors, respectively. Now the general formulation has been converted to matrix equations which can be solved according to the electrical conditions (closed/open circuit), mode of operation (actuation/sensing) and type of analysis (static/dynamic).

3.7 Numerical Examples and Discussions

The proposed formulation is validated here for accuracy and efficiency in static (actuation and sensing) and modal analyses (open and closed circuit) of piezoelectric smart beams. The software implementation of the present finite element formulation has been carried out in MATLAB environment. The performance of the present formulation is compared against the conventional two-noded EBT based formulations available in the literature and 2D finite element simulation results using ANSYS software. The finite element formulations used for the comparative study are designated here as:

> **EBT-*Coupled*** : The present formulation which uses coupled polynomials (cubic for w_0 given by Eq. (3.22a), coupled quadratic for u_0 given by Eq. (3.23) and linear for $\tilde{\varphi}_i$ given by Eq. (3.22b)) for interpolation of field variables and layerwise consistent through-thickness potential (coupled quadratic in z direction given by Eq. (3.9)). It does not employ any sublayers within the piezoelectric layer, for modelling. This formulation is expected to be free from piezolocking and material locking.
>
> **EBT** : The conventional EBT-based piezoelectric beam finite element formulation (Bendary et al., 2010) which uses independent polynomials for field interpolation (Hermite cubic for w_0, linear for u_0 and $\tilde{\varphi}_i$) and assumed linear through-thickness potential. This element suffers from piezolocking and material locking.

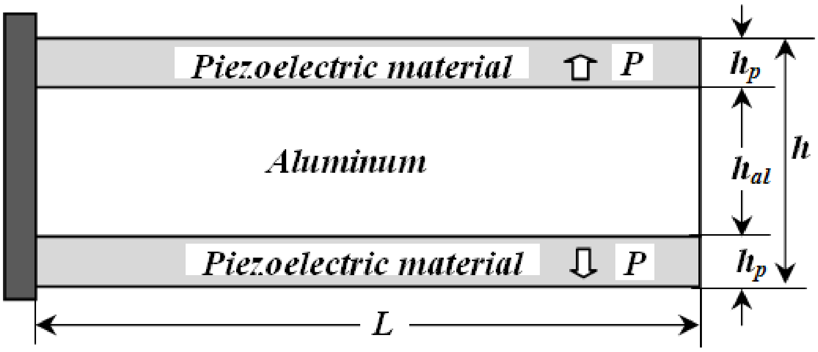

Figure 3.2: Example 1: Geometry of the three-layer cantilever beam with symmetrically bonded oppositely poled piezoelectric layers in extension mode.

EBT (with sublayers) : The piezolocking in the above EBT model may be eliminated by using a sufficient number of sublayers for modelling each piezoelectric layer. The through-thickness distribution of potential in each piezolayer is represented by sublayer-wise linear approximations. In this sublayered version of EBT, we have used *four sublayers* per physical piezoelectric layer, which are found adequate to yield reasonably accurate results. However, each sublayer would introduce an additional nodal electric potential degree of freedom and hence this element is computationally expensive.

ANSYS 2D : For a comparative evaluation of the above EBT formulations, benchmark solutions have been obtained from a refined 2-dimensional analysis using ANSYS finite element software (ANSYS-Release12, 2009), for which PLANE 183 elements are used to mesh conventional material layers, while PLANE 223 elements are used to mesh piezoelectric material layers.

3.7.1 Example 1: A three-layer symmetric piezoelectric beam

The test problem chosen here is an aluminum core with surface bonded oppositely poled piezoelectric layers of G1195N material, as shown in Fig. 3.2.
The material properties of the three layer beam are:
Aluminum (Kapuria and Hagedorn, 2007): $E = 70.3\,GPa$, $\nu = 0.345$, $\rho = 2710\,kgm^{-3}$
PZT G1195N (Peng et al., 1998): $E = 63\ GPa$, $\nu = 0.3$, $d_{31} = 254 \times 10^{-12}\ m/V$, $\epsilon_3 = 15 \times 10^{-9}\ F/m$, $\rho = 7600\ kgm^{-3}$.

This example is expected to show the adverse effects of piezolocking on the accuracy of the conventional EBT-based piezoelectric beam finite element. Material locking will be absent in this test case by virtue of the symmetry of the material distribution over the beam cross-section.

To study the performance of EBT-based smart beam formulations over a wide range of piezoelectric material proportion in the total thickness (thickness ratio: $r = (2h_p)/h$), the length (L) and total height (h) are taken as constant with values $500\ mm$ and $10\ mm$, respectively, while the thicknesses of piezoelectric layer (h_p) and aluminum layer (h_{al}) are varied for the present study. For a comparative evaluation of the various EBT formulations, converged results from ANSYS 2D analysis with a refined mesh size of 100×20 are used.

Static analysis: Actuator configuration

For actuator configuration, the interfaces of piezoelectric layers with aluminum layer are grounded and potentials of $\mp 10\ volts$ are applied on the free surfaces of the piezoelectric layer. The variation of tip deflection over a wide range of thickness ratio is plotted in Fig. 3.3. It is evident that the present EBT-*Coupled* formulation gives accurate results as that of ANSYS 2D simulation. Due to piezolocking effect, the conventional EBT formulation converges to inaccurate results and demands sublayered modelling to achieve the same level of accuracy as of the present formulation. The results clearly show the advantage of EBT-*Coupled* formulation, to efficiently handle the piezolocking effects.

The variation of error (%) in the tip deflection with thickness ratio due to piezolocking in the conventional EBT formulation is plotted in Fig. 3.4. As the proportion of piezoelectric material in the beam increases, the error due to the linear assumption of through-thickness potential becomes significant. The maximum difference is observed for a beam of pure piezoelectric material i.e. a *bimorph* configuration. Hence, the bimorph shown in Fig. 3.5 is considered for a detailed study of the induced potential effects.

Table 3.1 shows the results for the tip deflection of the bimorph for various numbers of sublayers in the modelling with EBT formulation of Bendary et al. (2010). As seen

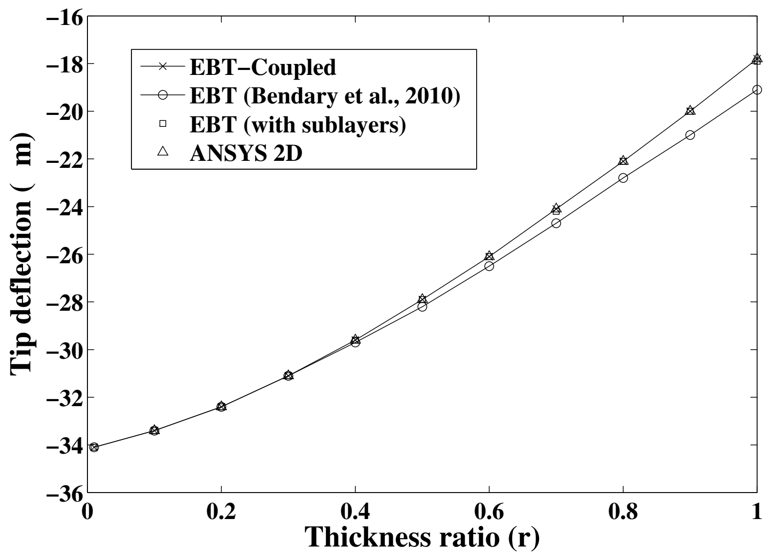

Figure 3.3: Example 1: Actuator configuration: Variation of the tip deflection with thickness ratio (r) for the three-layer cantilever beam actuated by ∓ 10 $volts$.

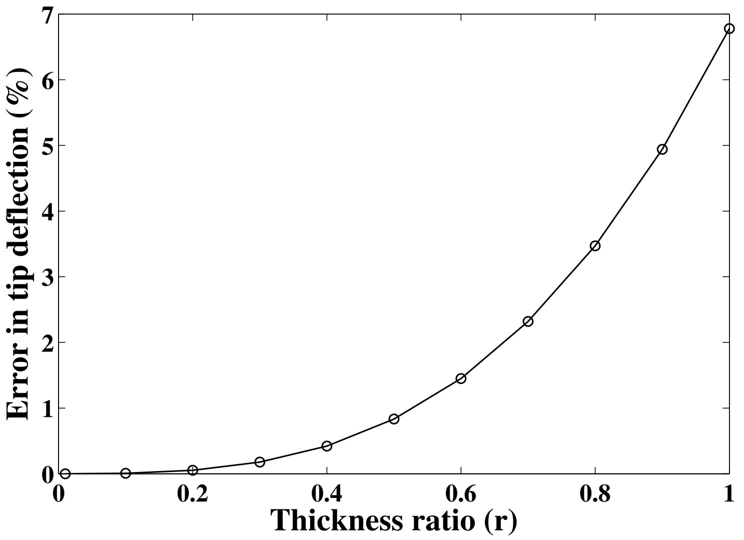

Figure 3.4: Example 1: Actuator configuration: Variation of error (%) in the tip deflection with thickness ratio (r), due to use of the conventional EBT formulation for the three-layer cantilever beam actuated by ∓ 10 $volts$.

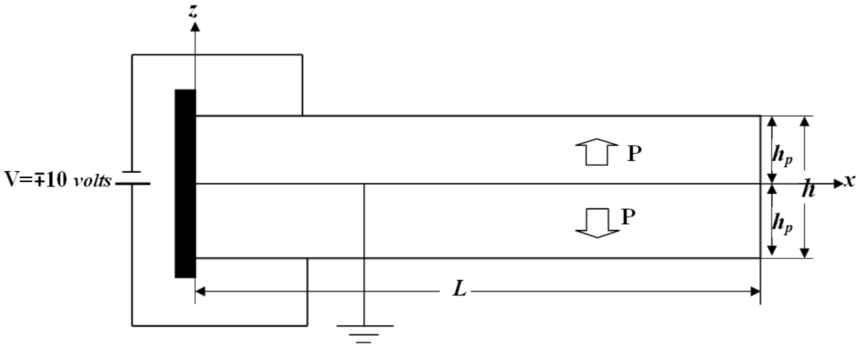

Figure 3.5: Example 1: Bimorph cantilever beam in the actuator configuration.

Table 3.1: Example 1: Actuator configuration: Tip deflection of the bimorph cantilever beam actuated by $\mp 10\,volts$ ($h = 10\,mm,\ L = 500\,mm$).

Formulation	Tip deflection (μm)
EBT (Bendary et al., 2010)	-19.05
EBT (with sublayers)	
2 sublayers/layer	-18.13
4 sublayers/layer	-17.91
ANSYS 2D	-17.84
EBT-*Coupled*	-17.84

from results, only with a sufficient number of sublayers in the modelling of piezoelectric layers, the conventional formulation converges to the accurate values as predicted by EBT-*Coupled* and ANSYS 2D simulation.

Also, the comparison of results for transverse deflection along the length, through-thickness distributions of potential and axial stress for the bimorph are plotted in Figs. 3.6, 3.7 and 3.8, respectively. The results prove the ability of EBT-*Coupled* to model the piezoelectric beam accurately as of ANSYS 2D and EBT (with sublayers). The conventional EBT formulation of Bendary et al. (2010) suffers from loss of accuracy due to piezolocking.

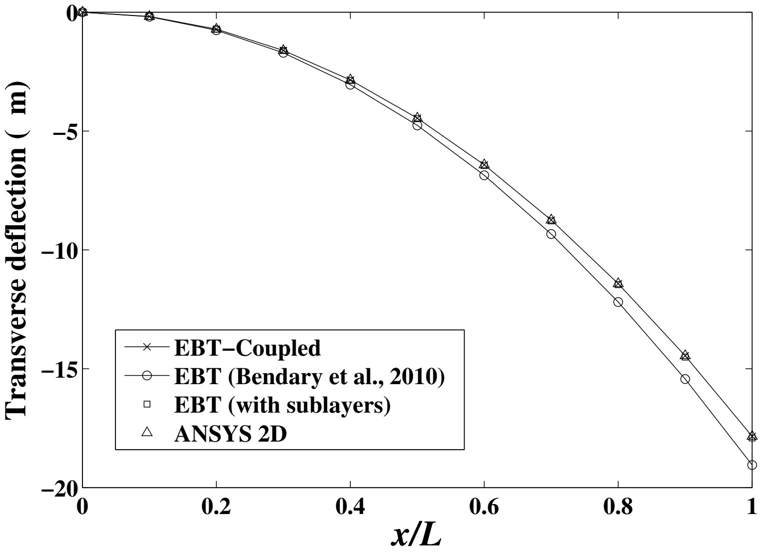

Figure 3.6: Example 1: Actuator configuration: Transverse deflection along the length of the bimorph cantilever beam actuated by ∓ 10 $volts$.

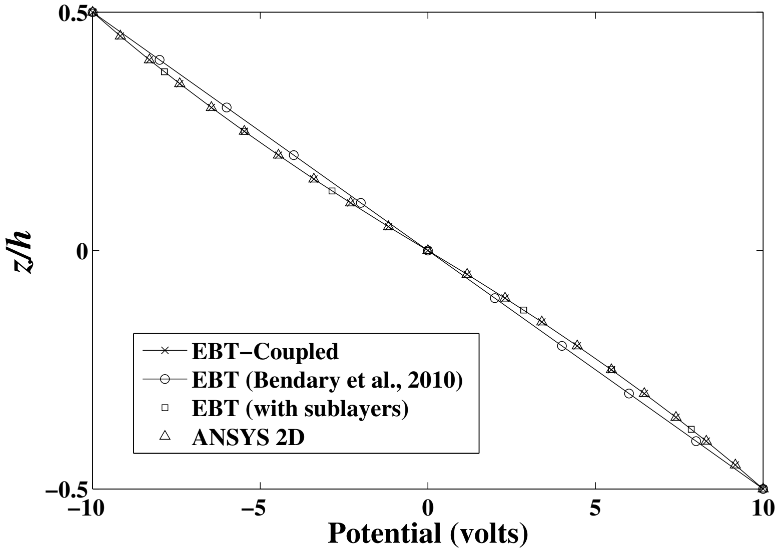

Figure 3.7: Example 1: Actuator configuration: Through-thickness potential distribution in the bimorph cantilever beam actuated by ∓ 10 $volts$.

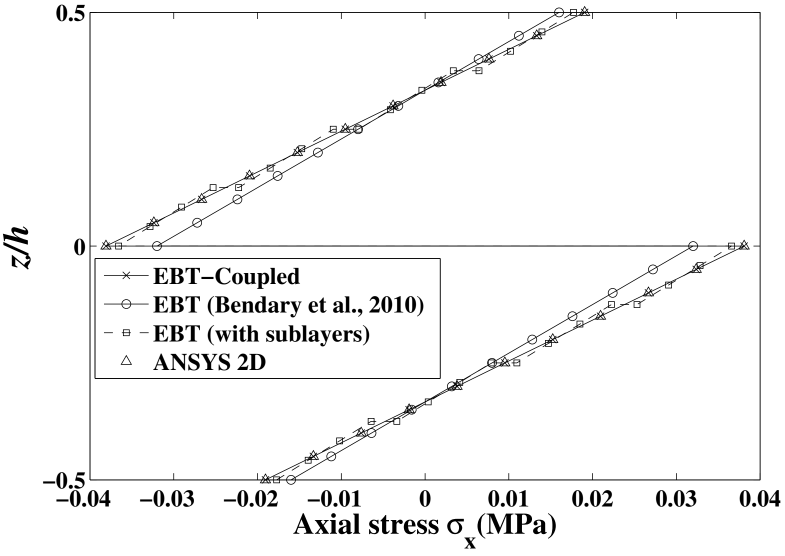

Figure 3.8: Example 1: Actuator configuration: Through-thickness axial stress distribution in the bimorph cantilever beam actuated by $\mp 10\ volts$.

Static analysis: Sensor configuration

For sensor configuration, the three-layer cantilever shown in Fig. 3.2 is subjected to a tip load of $-1000\ N$. The variations of tip deflection and potential developed across the piezoelectric layer at the root of the beam, with thickness ratio are plotted in Figs. 3.9 and 3.10, respectively. The graphs reveal the accuracy of EBT-*Coupled* to analyse piezoelectric beam in sensor configuration. It consistently produces accurate results as that of ANSYS 2D simulation, over the entire range of thickness ratio. The conventional EBT (Bendary et al., 2010) is incapable of exhibiting the desired accuracy consistently and the errors are significant for higher thickness ratios. It demands sublayered modelling to achieve same accuracy as that of EBT-*Coupled.* The inaccuracy due to piezolocking is quantified in the error (%) plotted in Fig. 3.11.

The variation of error (%) with thickness ratio shows that as we move from a beam of purely conventional material to a purely piezoelectric material beam i.e. bimorph, the error in the results increases significantly. Hence, the bimorph structure shown in Fig. 3.12 is considered here for detailed study of the induced potential effects.

Table 3.2 shows the results for the tip deflection and potential developed at the root of the bimorph for various numbers of sublayers in the modelling with conventional EBT formulation of Bendary et al. (2010). As seen from results, only with sufficient

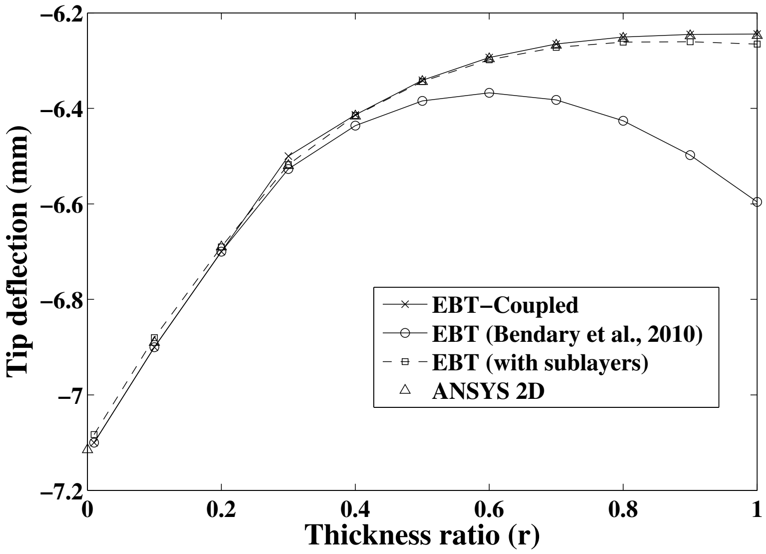

Figure 3.9: Example 1: Sensor configuration: Variation of the tip deflection with thickness ratio (r) for the three-layer cantilever beam subjected to a tip load of $-1000\ N$.

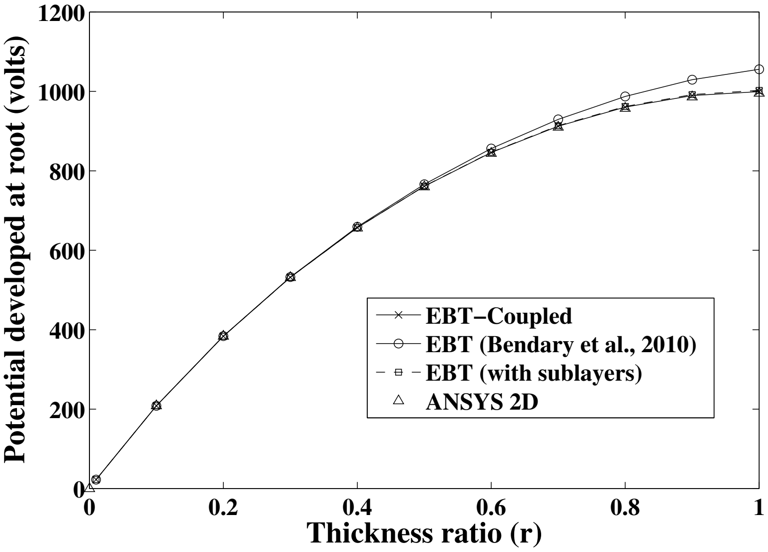

Figure 3.10: Example 1: Sensor configuration: Variation of the potential developed across each piezoelectric layer at the root with thickness ratio (r) for the three-layer cantilever beam subjected to a tip load of $-1000\ N$.

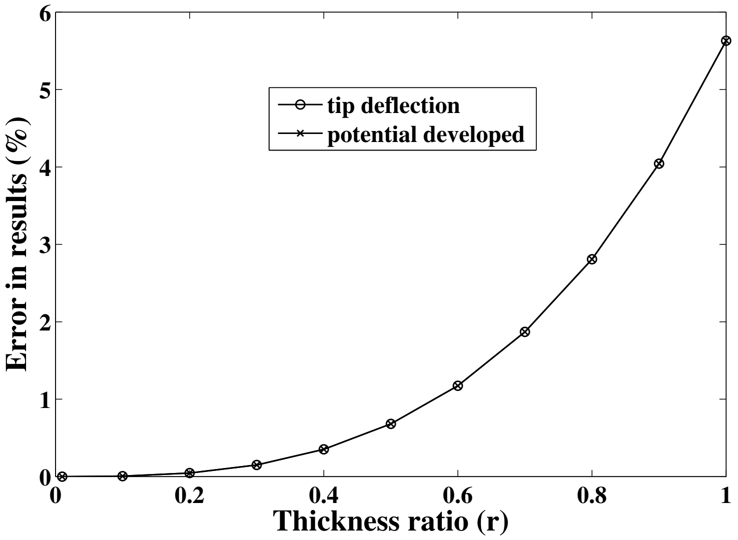

Figure 3.11: Example 1: Sensor configuration: Variation of error (%) in the tip deflection and the potential developed with thickness ratio (r), due to use of the conventional EBT formulation for the three-layer cantilever beam subjected to a tip load of $-1000\ N$.

number of sublayers in the modelling of piezoelectric layers, the conventional formulation converges to the accurate results as predicted by EBT-*Coupled* and ANSYS 2D simulation.

Also, the results for transverse deflection along the length, potential developed across each layer along the length, through-thickness potential and axial stress distributions at the root of the bimorph are plotted in Figs. 3.13 to 3.16, respectively. It is evident from the figures that results of the present EBT-*Coupled* formulation closely match with 2D simulation, while conventional EBT formulation of Bendary et al. (2010) needs sublayered model to eliminate loss of accuracy due to piezolocking. It may be noted that in Fig. 3.16, the conventional EBT formulation exhibit a large discontinuity in the axial stress at the interface, which tend to disappear with the addition of sufficient number of sublayers.

Modal analysis

The present formulation is validated here for the accuracy to predict the natural frequencies of smart cantilever shown in Fig. 3.2. The natural frequencies are evaluated for closed and open circuit electrical boundary conditions. For open circuit, only the

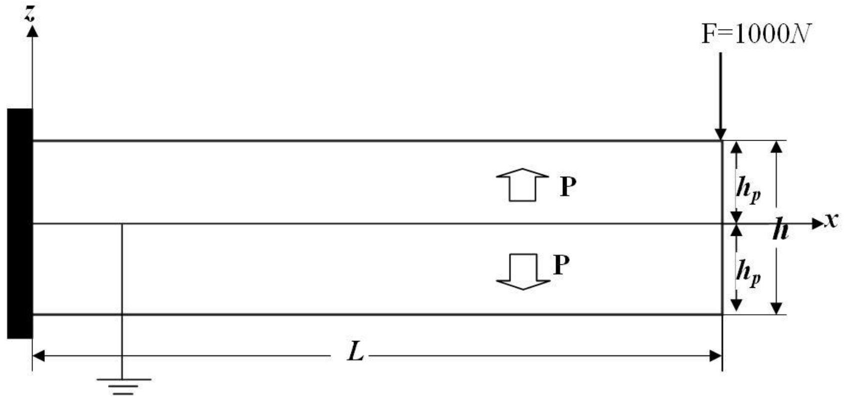

Figure 3.12: Example 1: Bimorph cantilever beam in the sensor configuration.

Table 3.2: Example 1: Sensor configuration: Tip deflection and potential developed at the root of the bimorph cantilever beam subjected to a tip load of $-1000\ N$ ($h = 10\ mm,\ L = 500\ mm$).

Formulation	Tip deflection (mm)	Potential ($volts$)
EBT (Bendary et al., 2010)	-6.60	1055
EBT (with sublayers)		
2 sublayers/layer	-6.33	1012
4 sublayers/layer	-6.26	1002
ANSYS 2D	-6.25	995.4
EBT-*Coupled*	-6.24	999.2

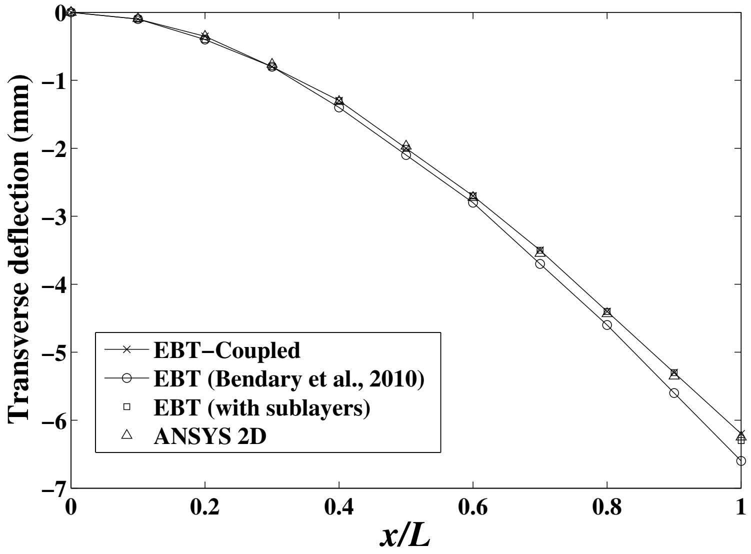

Figure 3.13: Example 1: Sensor configuration: Transverse deflection along the length of the bimorph cantilever beam subjected to a tip load of $-1000\ N$.

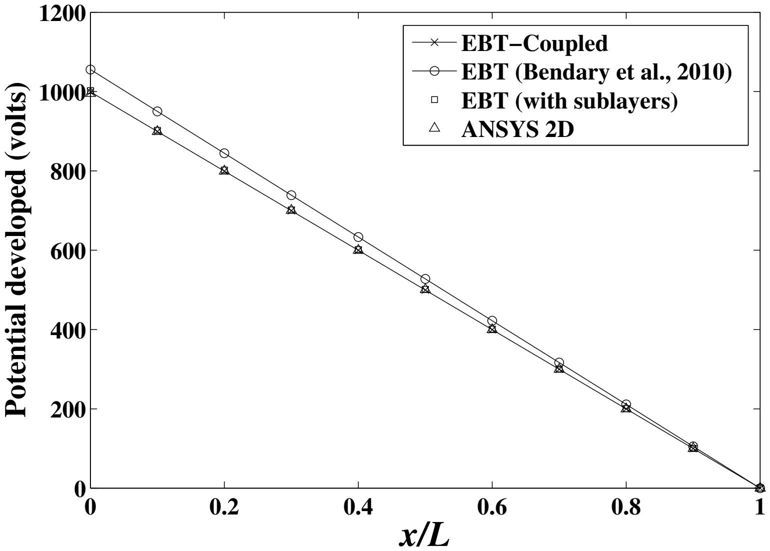

Figure 3.14: Example 1: Sensor configuration: Potential developed across each piezoelectric layer along the length of the bimorph cantilever beam subjected to a tip load of $-1000\ N$.

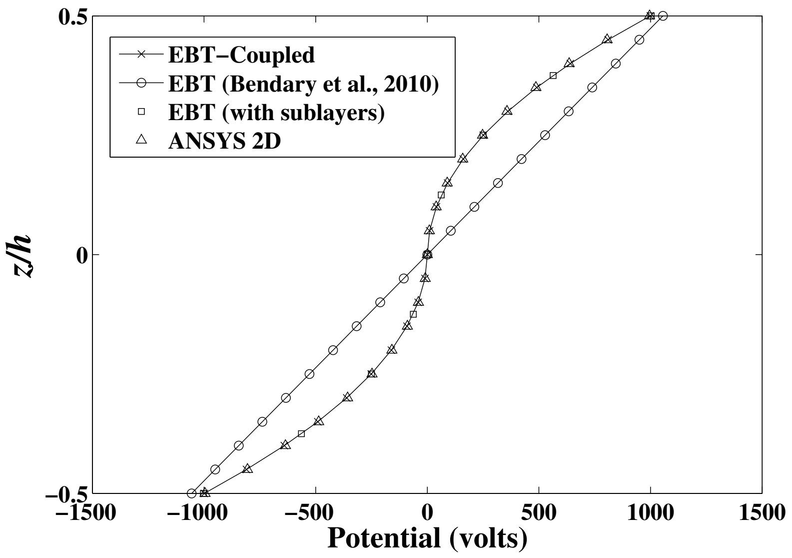

Figure 3.15: Example 1: Sensor configuration: Through-thickness potential distribution at the root of the bimorph cantilever beam subjected to a tip load of $-1000\ N$.

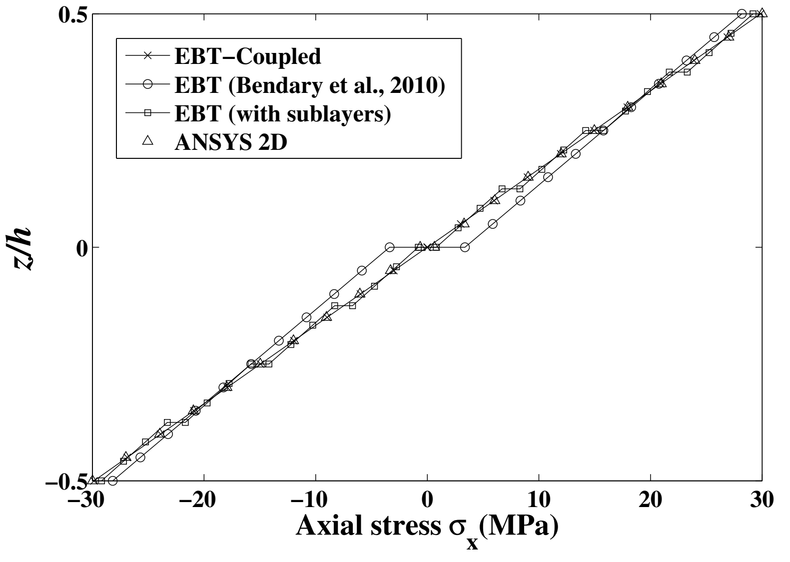

Figure 3.16: Example 1: Sensor configuration: Through-thickness axial stress distribution at the root of the bimorph cantilever beam subjected to a tip load of $-1000\ N$.

Table 3.3: Example 1: Natural frequencies in Hz for the bimorph cantilever beam ($h = 10\,mm,\ L = 500\,mm$).

Electrical Boundary condition	Mode No.	EBT (Bendary et al., 2010)	EBT (with sublayers)	ANSYS 2D	EBT-*Coupled*
Open Circuit	1^{st}	20.40	20.94	20.97	20.97
	2^{nd}	127.8	131.1	131.1	131.3
	3^{rd}	357.6	366.9	365.8	367.5
Closed Circuit	1^{st}	18.60	19.18	19.22	19.22
	2^{nd}	116.5	120.2	120.2	120.4
	3^{rd}	326.0	336.2	335.6	336.9

interfaces of piezoelectric layers with aluminum core are grounded, while for closed circuit all the faces of piezoelectric layers are grounded. The variations of first natural frequencies in open and closed circuit electrical boundary conditions, with thickness ratio are plotted in Fig. 3.17 (a) and 3.17 (b), respectively. As seen from the plots, the present EBT-*Coupled* predicts the accurate results as given by ANSYS 2D simulation. The conventional EBT formulation shows significant errors due to piezolocking and requires sublayered modelling to achieve acceptable results. The variation of errors (%) with thickness ratio is plotted in Fig. 3.18 which is maximum for bimorph configuration.

The results for the first three natural frequencies for the bimorph cantilever are tabulated in Table 3.3. As seen from the results, the conventional EBT formulation suffers form piezolocking and requires a number of sublayers to reproduce the accurate results.

3.7.2 Example 2: A two-layer asymmetric piezoelectric beam

The test problem chosen here is a two-layer asymmetric piezoelectric cantilever beam having a host layer made up of steel with a surface bonded piezoelectric layer of G1195N material at the top, as shown in Fig. 3.19. The material properties used are: Steel (Carrera and Brischetto, 2008): $E = 210\,GPa$, $\nu = 0.3$, $\rho = 7850\,kgm^{-3}$

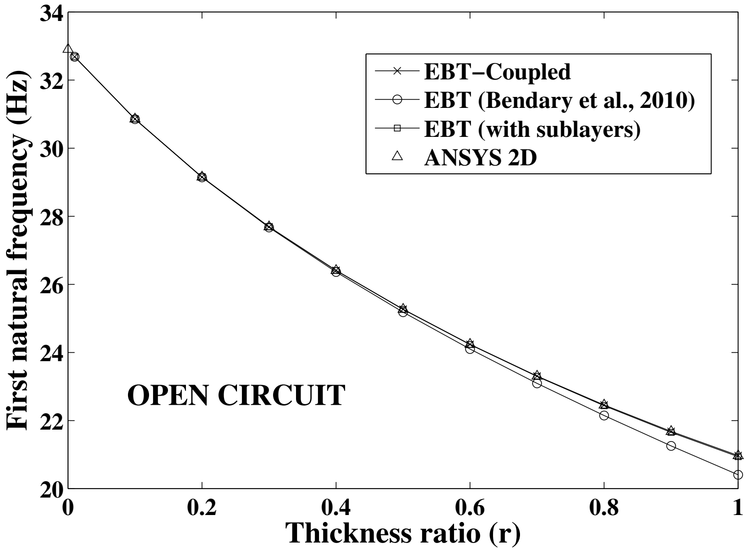

(a) Open circuit

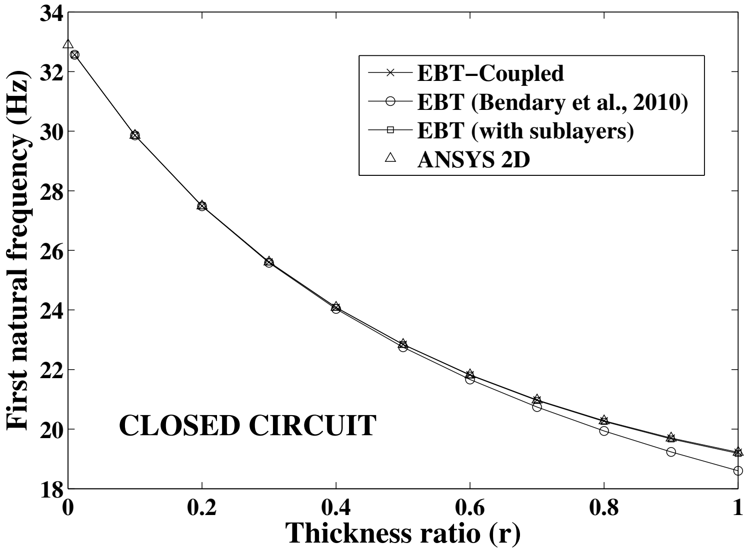

(b) Closed circuit

Figure 3.17: Example 1: Modal analysis: Variation of the first natural frequency with thickness ratio (r) for the three-layer cantilever beam.

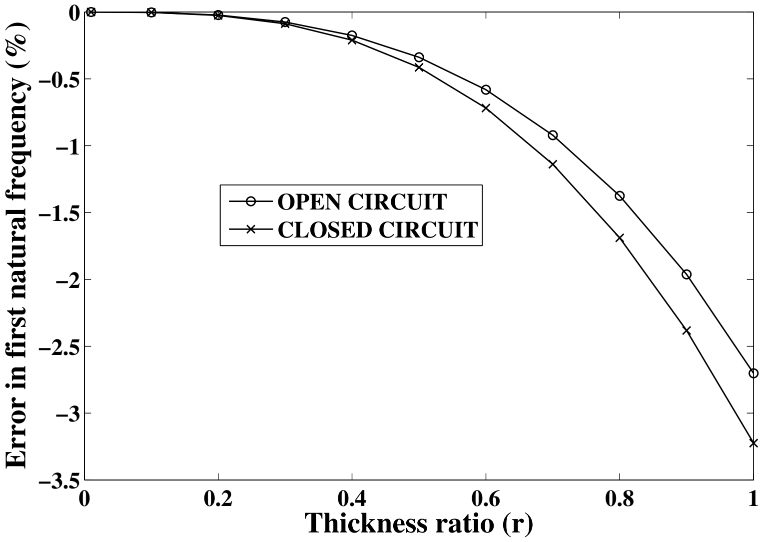

Figure 3.18: Example 1: Modal analysis: Variation of error (%) in the first natural frequency with thickness ratio (r), due to use of the conventional EBT formulation for the three-layer cantilever beam.

PZT G1195N (Peng et al., 1998): $E = 63\ GPa$, $\nu = 0.3$, $d_{31} = 254 \times 10^{-12}\ m/V$, $\epsilon_3 = 15 \times 10^{-9}\ F/m$, $\rho = 7600\ kgm^{-3}$.

This configuration is expected to show, in addition to piezolocking, the adverse effects of material locking on the convergence of the conventional EBT piezoelectric beam finite elements and improved performance of the proposed EBT-*Coupled* formulation.

For the present study, the length and total height of the beam are taken as constant

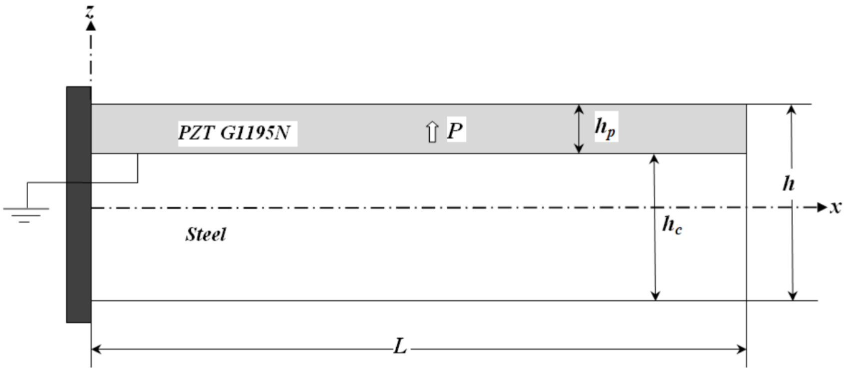

Figure 3.19: Example 2: Geometry of the two-layer cantilever beam with an asymmetrically bonded piezoelectric layer in extension mode.

($L = 100\ mm$, $h = 5\ mm$), while thicknesses of the piezoelectric layer (h_p) and the host layer (h_c) are varied. The performances of the EBT-based piezoelectric beam finite elements are evaluated over a wide range of piezoelectric material proportion in the total beam thickness (thickness ratio: $r = h_p/h$). For a comparative evaluation of various EBT-based formulations, the converged results from ANSYS 2D simulation with a mesh of 200×20 elements are used.

Static analysis: Sensor configuration

For sensor configuration, the beam shown in Fig. 3.19 is subjected to a tip load of $-1000\ N$. The variations of tip deflection, axial deflection and potential developed across the piezoelectric layer at the root of the beam with thickness ratio are plotted in Figs. 3.20, 3.21 and 3.22, respectively.

As seen from these graphs, the present EBT-*Coupled* formulation consistently gives accurate predictions of results as given by ANSYS 2D simulation, over the entire range of thickness ratio and proves the versatility of the coupled polynomial based formulation. Due to the piezolocking effects, the conventional EBT formulation (Bendary et al., 2010) does not perform consistently accurate. It demands sublayers in the modelling of piezolayer, to achieve the same consistent level of accuracy as of the present EBT-*Coupled* formulation. The error (%) due to piezolocking in the conventional EBT formulation is quantified in Fig. 3.23 for various thickness ratios. It is seen that the error increases rapidly in the higher thickness ratio regimes.

Figs. 3.24 and 3.25 show the comparison of convergence characteristics of EBT-based piezoelectric beam finite element formulations, for the tip deflection and potential developed at the root, respectively. It is noteworthy that EBT-*Coupled* exhibits single-element convergence, closely reproducing the ANSYS-2D solutions for both the tip deflection and the potential developed. As evident from these figures, the conventional EBT formulation (Bendary et al., 2010) and EBT (with sublayers) exhibit delayed convergence due to material locking effects. It is observed that the EBT-sublayered model eventually converges to the accurate results for tip deflection ($= -0.2598\ mm$) and potential ($= 376.09\ volts$). However, the conventional EBT model (Bendary et al., 2010) overestimates the response and converges to inaccurate results, due to piezolocking effects. This example clearly reveals the efficiency of the present coupled polynomial

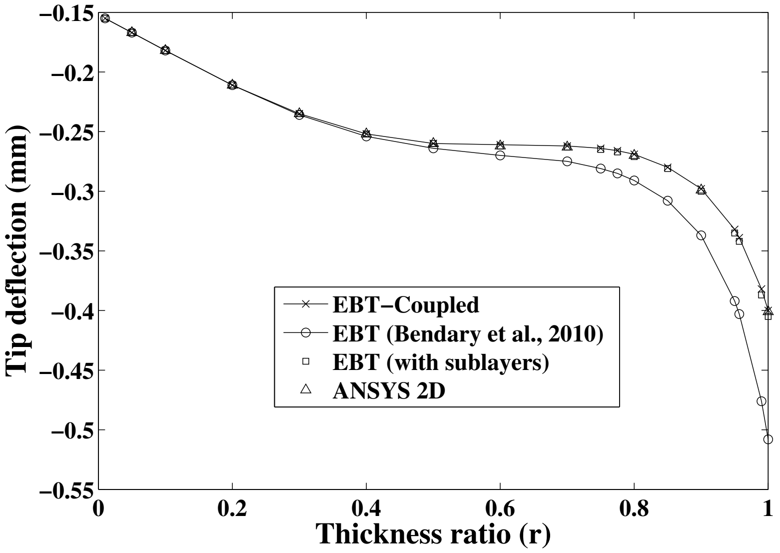

Figure 3.20: Example 2: Sensor configuration: Variation of the tip deflection with thickness ratio (r) for the asymmetric cantilever beam subjected to a tip load of -1000 N.

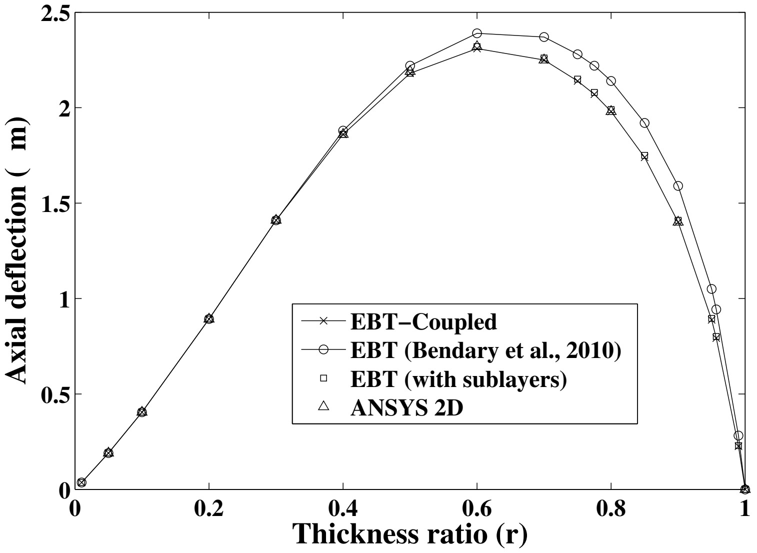

Figure 3.21: Example 2: Sensor configuration: Variation of the axial deflection with thickness ratio (r) for the asymmetric cantilever beam subjected to a tip load of -1000 N.

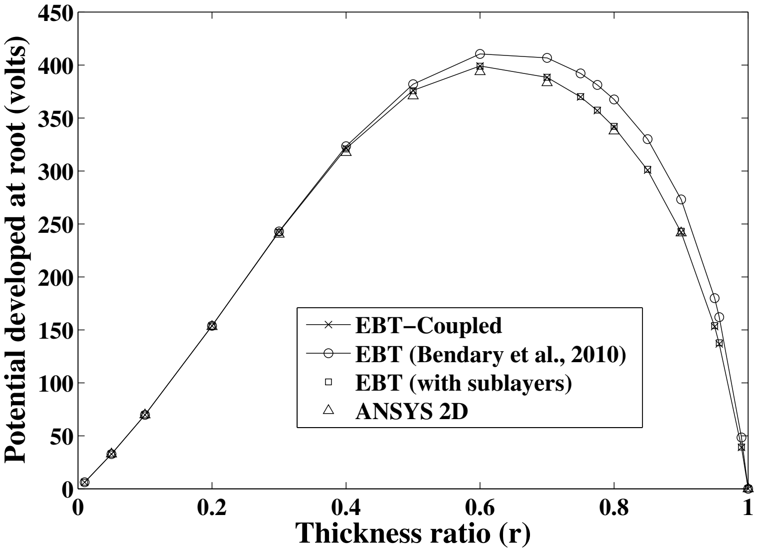

Figure 3.22: Example 2: Sensor configuration: Variation of the potential developed across piezoelectric layer at the root with thickness ratio (r) for the asymmetric cantilever beam subjected to a tip load of $-1000\ N$.

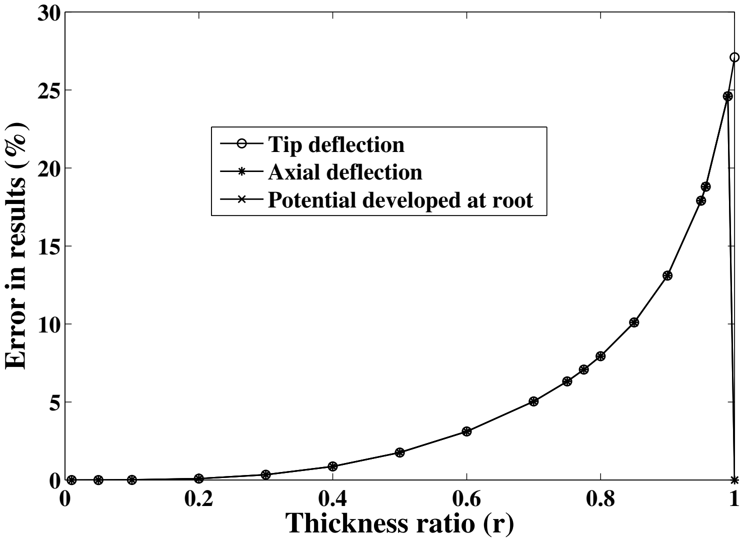

Figure 3.23: Example 2: Sensor configuration: Variation of error (%) in results with thickness ratio (r), due to use of the conventional EBT formulation.

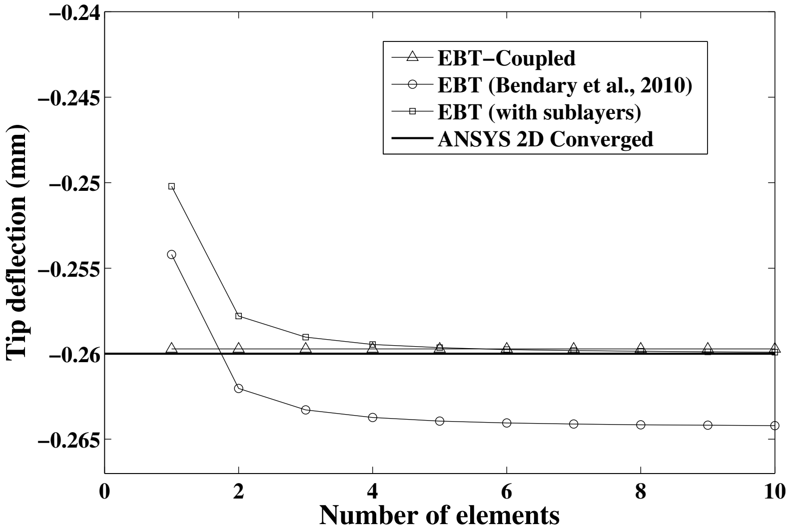

Figure 3.24: Example 2: Sensor configuration: Convergence characteristics of the EBT-based piezoelectric beam finite elements to predict the tip deflection of the asymmetric cantilever beam ($r = 0.5$) subjected to a tip load of $-1000\ N$.

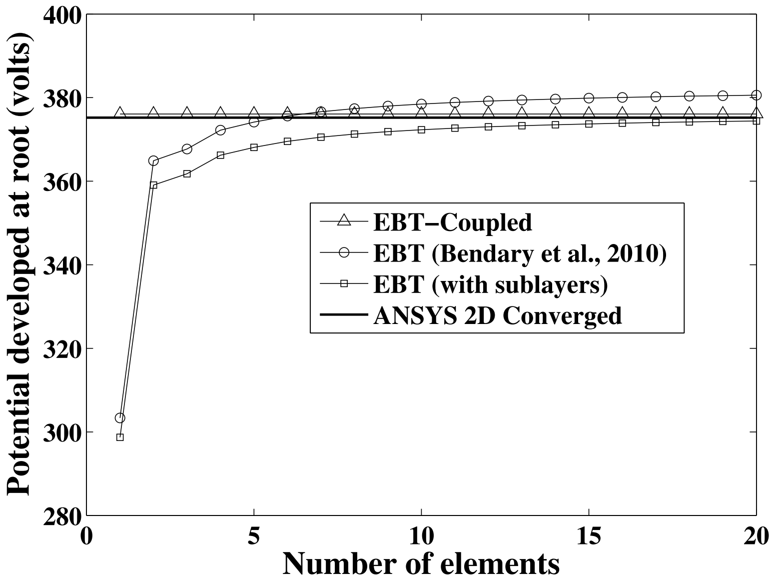

Figure 3.25: Example 2: Sensor configuration: Convergence characteristics of the EBT-based piezoelectric beam finite elements to predict the potential developed at the root of the asymmetric cantilever beam ($r = 0.5$) subjected to a tip load of $-1000\ N$.

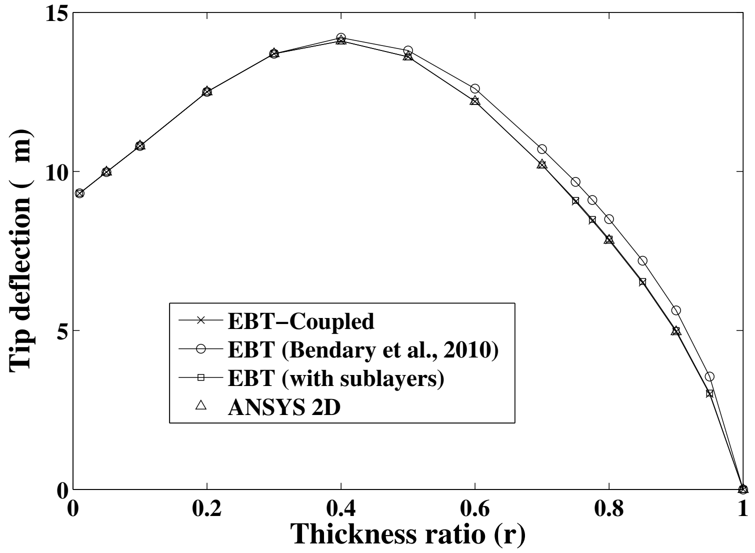

Figure 3.26: Example 2: Actuator configuration: Variation of the tip deflection with thickness ratio (r) for the asymmetric cantilever beam actuated by $100\ volts$.

interpolation over the conventional independent polynomial interpolations.

Static analysis: Actuator configuration

For actuator configuration, the beam shown in Fig. 3.19 is subjected to a voltage of $100\ volts$. The variations of tip deflection and axial deflection, with thickness ratio are plotted in Figs. 3.26 and 3.27, respectively. As seen from these graphs, the present EBT-*Coupled* formulation consistently gives accurate predictions of results as given by ANSYS 2D simulation, over the entire range of thickness ratio. Due to the piezolocking effects, the conventional EBT formulation (Bendary et al., 2010) does not yield consistently accurate results. It demands sublayers in the modelling of piezolayer, to achieve the same consistent level of accuracy as of the present EBT-*Coupled* formulation. The error (%) due to piezolocking in the conventional EBT formulation is quantified in Fig. 3.28 for various thickness ratios.

Modal analysis

The present EBT-*Coupled* formulation is evaluated here for its accuracy and efficiency to predict the natural frequencies of piezoelectric smart beams. The first natural fre-

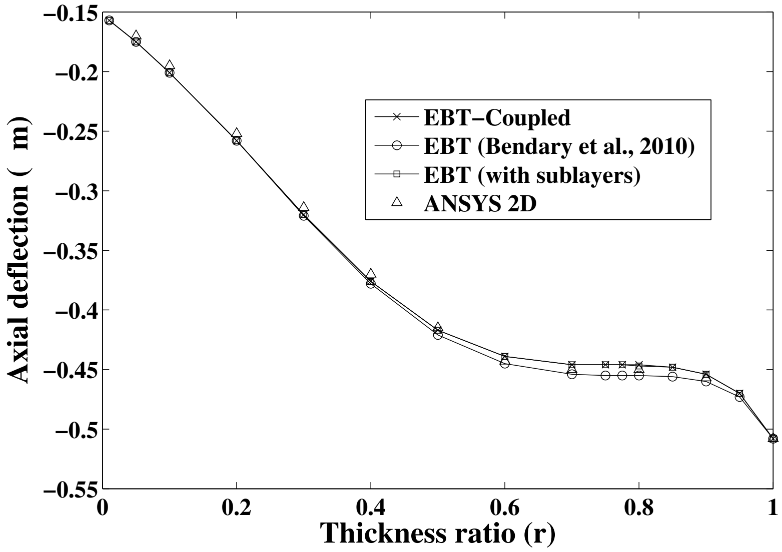

Figure 3.27: Example 2: Actuator configuration: Variation of the axial deflection with thickness ratio (r) for the asymmetric cantilever beam actuated by 100 $volts$.

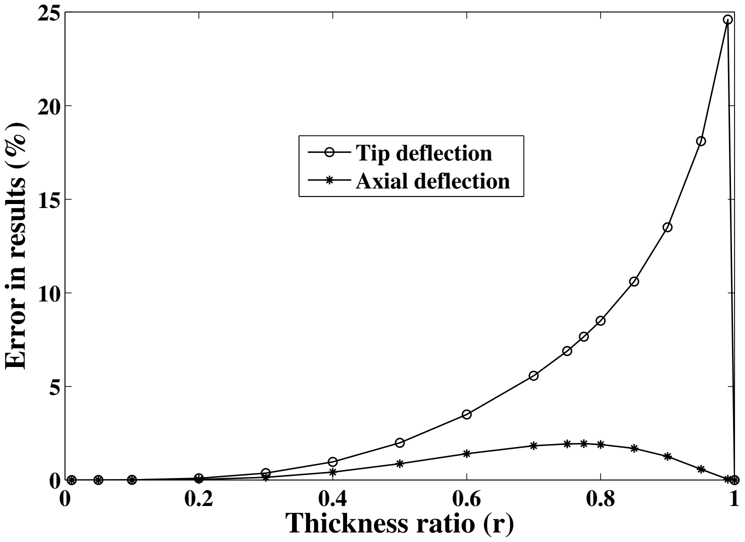

Figure 3.28: Example 2: Actuator configuration: Variation of error (%) in results with thickness ratio (r), due to use of the conventional EBT formulation.

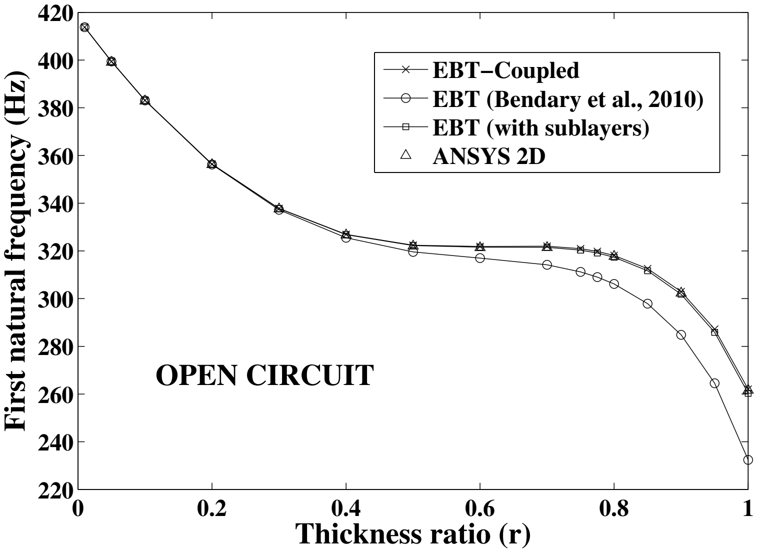

Figure 3.29: Example 2: Modal analysis: Variation of the first natural frequency with thickness ratio (r) for the asymmetric cantilever beam in open circuit electrical boundary condition.

quency of the asymmetric piezoelectric beam shown in Fig. 3.19 is evaluated for both open and closed circuit electrical boundary conditions. For open circuit, only the interface of piezoelectric layer with host layer is grounded while for closed circuit, both faces of the piezoelectric layer are grounded. The variations of first natural frequencies with thickness ratio are plotted in Figs. 3.29 and 3.30 for open and closed circuit electrical boundary conditions, respectively. The results from the present EBT-*Coupled* formulation agree very well with the results from ANSYS 2D simulation. This validates the use of the present coupled polynomial based interpolation for displacement fields, to generate consistent element mass matrix. Due to piezolocking effects, which are predominant in the higher thickness ratio regimes, the results from the conventional EBT formulation of Bendary et al. (2010) significantly deviate from the accurate results and hence requires sublayered modelling to yield acceptable level of accuracy. The error (%) due to piezolocking in the conventional EBT formulation is quantified in Fig. 3.31 for various thickness ratios.

The convergence graphs for first natural frequency in both open and closed circuit electrical boundary conditions are plotted in Figs. 3.32 and 3.33, respectively. The figures prove that the present coupled polynomial interpolation based element stiffness matrix and the corresponding consistent element mass matrix are capable of eliminat-

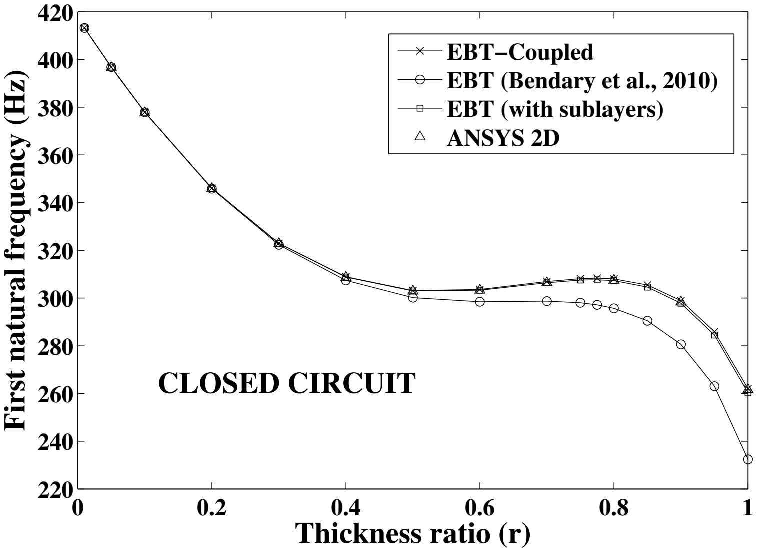

Figure 3.30: Example 2: Modal analysis: Variation of the first natural frequency with thickness ratio (r) for the asymmetric cantilever beam in closed circuit electrical boundary condition.

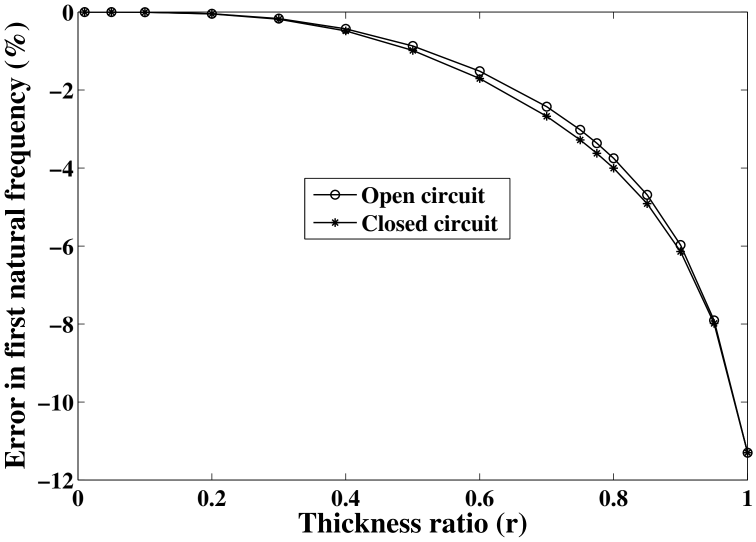

Figure 3.31: Example 2: Modal analysis: Variation of error (%) in results with thickness ratio (r), due to use of the conventional EBT formulation.

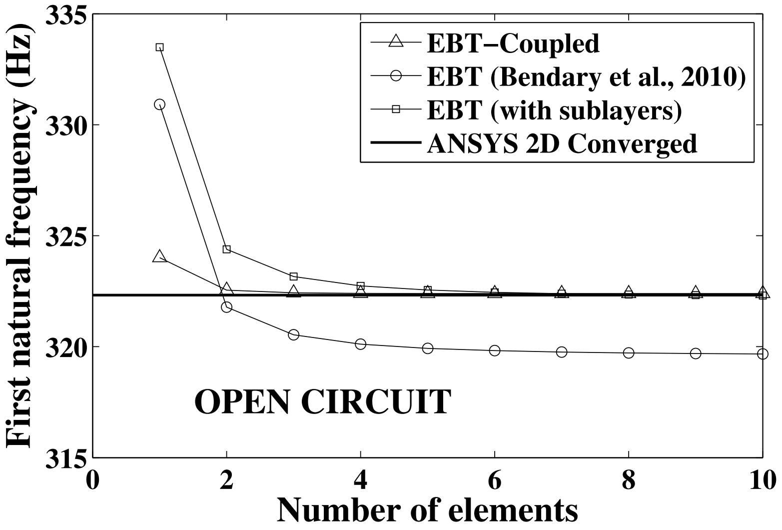

Figure 3.32: Example 2: Modal analysis: Convergence characteristics of the EBT-based piezoelectric beam finite elements to predict the first natural frequency of the asymmetric cantilever beam ($r = 0.5$) in open circuit electrical boundary condition.

ing the ill-effects of material locking on the the convergence of natural frequency. As the conventional EBT formulation (Bendary et al., 2010) suffers from piezolocking, it requires sublayers in its modelling, to converge to accurate results. Both conventional EBT and EBT-sublayered exhibit poor convergence due to material locking effects.

The role of the coupled quadratic term in the axial displacement given by Eq. (3.23), in eliminating material locking and improving the convergence is evident from the Table 3.4, where the results obtained with and without the coupled quadratic term are tabulated. The results prove the role of the coupled quadratic term in enabling EBT-*Coupled* to yield quick convergence for the natural frequencies. The results for the asymmetric beam with $r = 0.5$ given in Table 3.4 are normalized with respect to the converged values from the EBT-*Coupled*.

3.8 Summary

A coupled polynomial interpolation scheme for EBT-based piezoelectric beam finite element has been proposed here to enhance its performance by eliminating material locking and piezolocking phenomena. A consistent interpolation for through-thickness

Table 3.4: Example 2: Role of coupled quadratic term in the field interpolation for axial displacement (Eq. (3.23)) in improving the convergence characteristics of EBT-*Coupled* in modal analysis.

Number of elements	Normalized natural frequency					
	1^{st}		2^{nd}		3^{rd}	
	coupled	linear	coupled	linear	coupled	linear
			Open circuit			
1	1.005	1.035	1.649	1.735	2.130	2.136
2	1.000	1.007	1.009	1.065	1.177	1.233
4	1.000	1.002	1.001	1.012	1.006	1.032
8	1.000	1.000	1.000	1.003	1.000	1.007
16	1.000	1.000	1.000	1.001	1.000	1.002
			Closed circuit			
1	1.005	1.048	1.648	1.778	2.200	2.207
2	1.000	1.011	1.009	1.092	1.224	1.282
4	1.000	1.003	1.001	1.019	1.007	1.051
8	1.000	1.001	1.000	1.005	1.000	1.011
16	1.000	1.000	1.000	1.001	1.000	1.003

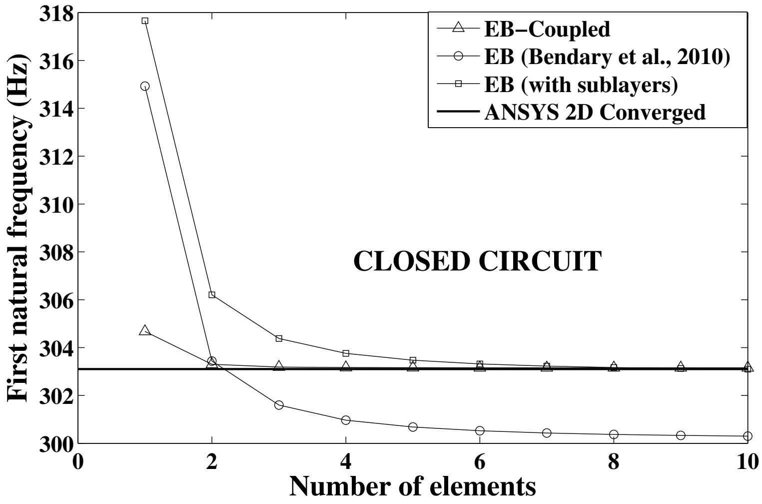

Figure 3.33: Example 2: Modal analysis: Convergence characteristics of the EBT-based piezoelectric beam finite elements to predict the first natural frequency of the asymmetric cantilever beam ($r = 0.5$) in closed circuit electrical boundary condition.

potential, derived from the electrostatic equilibrium equation has been used in the formulation to eliminate piezolocking. A coupled polynomial expression has been derived for axial displacement of the beam using the governing equilibrium equations. The resulting coupled shape functions handle bending-extension coupling in an efficient manner to eliminate material locking. The merits of the present formulation over the conventional formulations have been proved by the comparison of the results for the set of test problems.

CHAPTER 4

COUPLED FSDT PIEZOELECTRIC BEAM FINITE ELEMENT

4.1 Introduction

In this chapter, coupled polynomial interpolations are proposed for ESL-FSDT (Equivalent Single Layer First-order Shear Deformation Theory) based piezoelectric beam finite element formulation. The conventional FSDT piezoelectric beam element suffers from *loss of accuracy* due to piezolocking and *slow convergence* due to material locking as well as shear locking.

The conventional FSDT piezoelectric beam finite element formulations employ linear polynomial to approximate the through-thickness potential and hence converge to inaccurate results due to piezolocking. The traditional methods like use of higher-order approximation for through-thickness potential and the use of sublayers in the mathematical formulation of the piezoelectric layer increase the number of nodal degrees of freedom and the computational cost.

The conventional FSDT piezoelectric beam finite element which uses linear interpolation of axial displacement leads to a poor convergence of results when the beam cross-section is materially asymmetric due to material locking. The traditional method of using higher order polynomial for interpolation of axial displacement leads to increased number of nodal degrees of freedom and the computational cost.

Shear locking is due to the bending-shear coupling which originates from the definition of shear strain. According to FSDT, the shear strain is defined as the sum of the derivative of transverse deflection ($w^{'}$) and the the section rotation (θ). The conventional isoparametric two-noded FSDT beam element uses linear polynomials to interpolate both w and θ fields. Accordingly, for the shear strain field, the linear term contributed by θ field has no matching linear term from the $w^{'}$ field. In the thin limits of vanishing shear strains, the individual coefficients of the shear strain field should tend to vanish. When the unmatched coefficient of the shear strain field contributed by θ tends to zero, it acts as a spurious constraint on the bending strain where θ is primary variable. This results in a very poor bending response and demands an unacceptably high number of elements to get converged results. The shear locking can be eliminated by the use of a higher-order interpolation for the transverse deflection w, which increases computational cost. The Reduced Integration technique used in the literature, which depends on the one-order lower numerical integration of shear stiffness, is a good alternative without increasing the number of nodal degrees of freedom. However, the overall convergence behaviour of the two-noded isoparametric beam element remains unimpressive, due to constant curvature strain interpolation.

In the proposed coupled FSDT formulation presented here, a coupled consistent through-thickness potential distribution is derived using an electrostatic equilibrium equation, which eliminate piezolocking, without increasing the number of nodal degrees of freedom. A coupled quadratic polynomials for axial displacement (u_0) and section rotation (θ) of the beam are derived using governing equilibrium equations obtained from the variational formulation, which eliminate material locking and shear locking.

4.2 Theoretical Formulation

The formulation is based on ESL-FSDT with layerwise electric potential. Consider a general multilayered extension mode piezoelectric cantilever beam as shown in Fig. 4.1. The layer(s) can be host layers of conventional/composite material or bonded/embedded layer(s) of piezoelectric material. The beam layers are assumed to be made up of isotropic or specially orthotropic materials, with perfect bonding between them. The top and bottom faces of the piezoelectric layers are fully covered with electrodes. The mechanical and electrical quantities are assumed to be small enough to apply linear theories of elasticity and piezoelectricity.

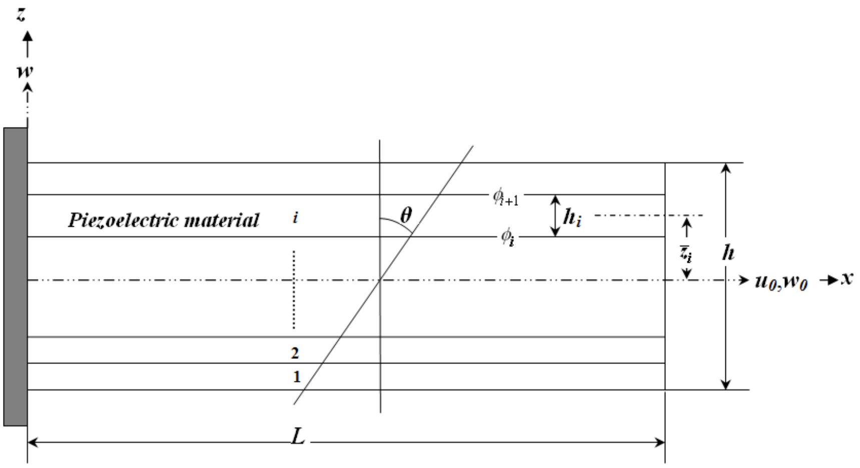

Figure 4.1: FSDT formulation: Geometry of a general multilayered extension mode piezoelectric smart beam.

4.2.1 Mechanical displacements and strains

The displacement fields in the longitudinal and transverse directions for FSDT are given as (Narayanan and Balamurugan, 2003):

$$u(x,z) = u_0(x) + z\theta(x) \tag{4.1}$$

$$w(x,z) = w_0(x) \tag{4.2}$$

The sub-functions $u_0(x)$ and $w_0(x)$ are the longitudinal and transverse displacements at the centroidal axis of the beam, respectively. θ is the section rotation of the beam. The dimensions L, b and h are the length, width and the total thickness of the beam, respectively.

Substituting Eqs. (4.1) and (4.2) in the usual strain-displacement relations, the following expressions for axial and shear strains are obtained:

$$\varepsilon_x(x,z) = \frac{\partial u(x,z)}{\partial x} = u_0^{'}(x) + z\theta^{'}(x) \tag{4.3}$$

where $()'$ denotes $\mathrm{d}/\mathrm{d}x$.

$$\gamma_{xz}(x,z) = \frac{\partial u(x,z)}{\partial z} + \frac{\partial w(x,z)}{\partial x} = \theta(x) + w_0^{'}(x) \tag{4.4}$$

4.2.2 Electric potential and electric field

The layerwise through-thickness distribution of the electric potential is assumed as shown in Fig. 4.1. The two dimensional electric potential of the i^{th} piezoelectric layer $\varphi_i(x,z)$, takes the values of $\phi_{i+1}(x)$ and $\phi_i(x)$ at the top and bottom surfaces of the piezoelectric layer with thickness h_i, respectively. The electric field in the transverse (z) direction is derived from electric potential as (Benjeddou et al., 1997):

$$E_z^i(x,z) = -\frac{\partial \varphi_i(x,z)}{\partial z} \tag{4.5}$$

4.2.3 Constitutive relations

Coupled constitutive relations for FSDT-based piezoelectric beam formulation are given as (Appendix A):

$$\begin{bmatrix} \sigma_x^k \\ \tau_{xz}^k \\ D_z^i \end{bmatrix} = \begin{bmatrix} \tilde{Q}_{11}^k & 0 & -\tilde{e}_{31}^i \\ 0 & \tilde{Q}_{55}^k & 0 \\ \tilde{e}_{31}^i & 0 & \tilde{\epsilon}_3^i \end{bmatrix} \begin{bmatrix} \varepsilon_x \\ \gamma_{xz} \\ E_z^i \end{bmatrix} \tag{4.6}$$

where (i=1......number of piezoelectric layers in the beam) and (k=1.......total number of layers in the beam).

4.3 Derivation of Potential Consistent with FSDT

For the free volumic charge density assumption, the electrostatic equilibrium equation of the i^{th} piezoelectric layer reduces to (Benjeddou et al., 1997):

$$\frac{\partial D_z^i(x,z)}{\partial z} = 0 \tag{4.7}$$

as $D_x^i = D_y^i = 0$ form Eq. (4.6).

Using Eqs. (4.3), (4.5), (4.6) and (4.7), we get:

$$\frac{\partial^2 \varphi_i(x,z)}{\partial z^2} = \frac{\tilde{e}_{31}^i}{\tilde{\epsilon}_3^i}\theta'(x) \tag{4.8}$$

On solving Eq. (4.8), we have:

$$\varphi_i(x,z) = \frac{\tilde{e}_{31}^i}{\tilde{\epsilon}_3^i}\frac{z^2}{2}\theta'(x) + C_1^i(x)z + C_2^i(x) \tag{4.9}$$

where, C_1^i and C_2^i are the constants to be obtained from boundary conditions for φ_i in z-direction. For i^{th} piezolayer boundary conditions are $\varphi_{z=z_i}(x,z) = \phi_i(x)$ and $\varphi_{z=z_{i+1}}(x,z) = \phi_{i+1}(x)$. After solving Eq. (4.9) and simplifying, we get:

$$\varphi_i(x,z) = \bar{\varphi}_i(x) + \left(\frac{z-\bar{z}_i}{h_i}\right)\tilde{\varphi}_i(x) - \frac{\tilde{e}_{31}^i}{\tilde{\epsilon}_3^i}\frac{h_i^2}{8}\left(1 - \frac{4\left(z-\bar{z}_i\right)^2}{h_i^2}\right)\theta'(x) \tag{4.10}$$

where $\bar{\varphi}_i = \left(\phi_{i+1} + \phi_i\right)/2$; $\tilde{\varphi}_i = \phi_{i+1} - \phi_i$ and $\bar{z}_i = \left(z_{i+1} + z_i\right)/2$.

Form Eq. (4.10), it is clear that, the electric potential consistent with FSDT mechanical field is quadratic in the transverse direction. The first two terms describe the conventional linear part in which $\bar{\varphi}$ and $\tilde{\varphi}$ are the mean and difference of potentials on the top and bottom faces of the i^{th} piezoelectric layer, respectively. The third term which is quadratic denotes the bending strain contribution to the potential. This nonlinear term constitutes the induced potential and plays an important role in the formulation, as it changes the stiffness of the structure. The coefficient of the induced potential term depends on the geometric and material properties of the piezoelectric layer.

The transverse electric field is derived from Eq. (4.10) as:

$$E_z^i(x,z) = -\frac{\partial\varphi_i(x,z)}{\partial z} = -\frac{\tilde{\varphi}_i(x)}{h_i} - \frac{\tilde{e}_{31}^i}{\tilde{\epsilon}_3^i}\left(z-\bar{z}_i\right)\theta'(x) \tag{4.11}$$

4.4 Variational Formulation

Hamilton's principle is used to formulate the smart beam. It is expressed as (Chee et al., 1999):

$$\delta\int_{t_1}^{t_2}\left(K - H + W\right)dt = \int_{t_1}^{t_2}\left(\delta K - \delta H + \delta W\right)dt = 0 \tag{4.12}$$

where K is the kinetic energy, H is the electric enthalpy density function for the piezoelectric material and the mechanical strain energy for the linear elastic material and W is the work done by the external forces.

4.4.1 Variation of electromechanical/strain energy

For the j^{th} conventional material layer, the variation of mechanical strain energy δH is given by:

$$\delta H_j = \int_V \left(\sigma_x^j \delta \varepsilon_x^j + \tau_{xz}^j \delta \gamma_{xz}^j \right) dV \tag{4.13}$$

The variation of electromechanical energy for the i^{th} piezoelectric layer is given by:

$$\delta H_i = \int_V \left(\sigma_x^i \delta \varepsilon_x^i + \tau_{xz}^i \delta \gamma_{xz}^i - D_z^i \delta E_z^i \right) dV \tag{4.14}$$

Substituting values of axial strain (ε_x), shear strain (γ_{xz}), transverse electric field (E_z) from Eqs. (4.3), (4.4), (4.11) and using them along with constitutive relations from Eq. (4.6) in Eqs. (4.13) and (4.14), variation on total electromechanical/strain energy of the beam is written as:

$$\begin{aligned}
\int_{t_1}^{t_2} \delta H dt = \int_{t_1}^{t_2} \int_x \Bigg\{ & \delta u_0^{'} \left[\begin{array}{c} (\tilde{Q}_{11}^k I_0^k) u_0^{'} + \left(\tilde{Q}_{11}^k I_1^k + \left(\left(\tilde{e}_{31}^i \right)^2 / \tilde{\epsilon}_3^i \right) \left(I_1^i - I_0^i \bar{z}_i \right) \right) \theta^{'} \\ + \left(\tilde{e}_{31}^i I_0^i / h_i \right) \tilde{\varphi}_i \end{array} \right] + \\
& \delta \theta^{'} \left[\begin{array}{c} \left(\tilde{Q}_{11}^k I_1^k + \left(\left(\tilde{e}_{31}^i \right)^2 / \tilde{\epsilon}_3^i \right) \left(I_1^i - I_0^i \bar{z}_i \right) \right) u_0^{'} \\ + \left(\tilde{Q}_{11}^k I_2^k + \left(\left(\tilde{e}_{31}^i \right)^2 / \tilde{\epsilon}_3^i \right) \left(I_2^i - I_0^i \bar{z}_i^2 \right) \right) \theta^{'} \\ + \left(\tilde{e}_{31}^i I_0^i \bar{z}_i / h_i \right) \tilde{\varphi}_i \end{array} \right] + \\
& \delta \theta \left[\tilde{Q}_{55}^k I_0^k \right] \left(\theta + w_0^{'} \right) + \delta w_0^{'} \left[\tilde{Q}_{55}^k I_0^k \right] \left(\theta + w_0^{'} \right) + \\
& \delta \tilde{\varphi}_i \left[\begin{array}{c} \left(\tilde{e}_{31}^i I_0^i / h_i \right) u_0^{'} + \left(\tilde{e}_{31}^i I_0^i \bar{z}_i / h_i \right) \theta^{'} \\ - (\tilde{\epsilon}_3^i I_0^i / h_i^2) \tilde{\varphi}_i \end{array} \right] \Bigg\} dx dt
\end{aligned} \tag{4.15}$$

where i=(1.....number of piezolayers), k=(1......total number of layers) and
$I_q^k = b \left(z_{k+1}^{q+1} - z_k^{q+1} \right) / (q+1)$.

4.4.2 Variation of kinetic energy

The electrical variables do not enter into the expression for kinetic energy and it is given as (Chee et al., 1999):

$$K = \frac{1}{2} b \int_x \int_{z_k}^{z_{k+1}} \rho_k \left(\dot{u}^2 + \dot{w}^2 \right) dz dx \tag{4.16}$$

where ρ_k is the mass density of k^{th} layer in kgm^{-3} and (k=1....total number of layers in beam). Substituting values of u and w from Eqs. (4.1) and (4.2) and applying variation to get:

$$
\begin{aligned}
-\int_{t1}^{t2} \delta K dt =& \rho_k \int_{t1}^{t2} \int_{x} \Big\{ \delta u_0 \left(I_0^k \ddot{u}_0 + I_1^k \ddot{\theta} \right) + \delta\theta \left(I_1^k \ddot{u}_0 + I_2^k \ddot{\theta} \right) \\
& + \delta w_0 \left(I_0^k \ddot{w}_0 \right) \Big\} \, dxdt
\end{aligned}
\tag{4.17}
$$

where $\dot{()}$ denotes $\frac{\partial}{\partial t}$.

4.4.3 Variation of the work of external forces

The total virtual work on the structure can be defined as the product of the virtual displacements with forces for the mechanical work and the product of the virtual electric potential with the charges for the electrical work. The variation of the total work done by the external mechanical and electrical loading is given as (Chee et al., 1999):

$$
\begin{aligned}
\int_{t_1}^{t_2} \delta W dt = \int_{t_1}^{t_2} \Big\{ & \int_V (\delta u f_u^v + \delta w f_w^v) dV + \int_S (\delta u f_u^s + \delta w f_w^s) dS \\
& + \sum (\delta u f_u^c + \delta w f_w^c) - \int_{S\varphi} \delta\varphi q_0 dS_\varphi \Big\} \, dt
\end{aligned}
\tag{4.18}
$$

in which f^v,f^s,f^c are volume, surface, point forces, respectively; q_0 and S_φ are the surface charges and area on which charge is applied.

4.5 Derivation of Coupled Field Relations

The relationship between the field variables is established here, using static governing equilibrium equations. For static condition without any external loading, the variational principle given in Eq. (4.12) reduces to:

$$
\delta H = 0 \tag{4.19}
$$

Applying variation to the basic variables in Eq. (4.15) and using them in Eq. (4.19), we get the static equilibrium equations as:

$$\delta u_0 : \qquad \begin{bmatrix} (\tilde{Q}^k_{11} I^k_0) u_0^{''} + \left(\tilde{Q}^k_{11} I^k_1 + \left((\tilde{e}^i_{31})^2 / \tilde{\epsilon}^i_3\right)(I^i_1 - I^i_0 \bar{z}_i)\right) \theta^{''} \\ + (\tilde{e}^i_{31} I^i_0 / h_i)\, \tilde{\varphi}_i^{'} \end{bmatrix} = 0 \tag{4.20}$$

$$\delta\theta : \quad \begin{bmatrix} -\left(\tilde{Q}^k_{11} I^k_1 + \left((\tilde{e}^i_{31})^2 / \tilde{\epsilon}^i_3\right)(I^i_1 - I^i_0 \bar{z}_i)\right) u_0^{''} \\ -\left(\tilde{Q}^k_{11} I^k_2 + \left((\tilde{e}^i_{31})^2 / \tilde{\epsilon}^i_3\right)(I^i_2 - I^i_0 \bar{z}_i^2)\right) \theta^{''} - (\tilde{e}^i_{31} I^i_0 \bar{z}_i / h_i)\, \tilde{\varphi}_i^{'} \\ + \left(\tilde{Q}^k_{55} I^k_0\right)(\theta + w_0^{'}) \end{bmatrix} = 0 \tag{4.21}$$

$$\delta w_0 : \quad \left[\left(\tilde{Q}^k_{55} I^k_0\right)(\theta^{'} + w_0^{''})\right] = 0 \tag{4.22}$$

From Eq. (4.22), we can write:

$$\theta^{''} = -w_0^{'''} \tag{4.23}$$

Using Eqs. (4.20) and (4.23), the relation between axial displacement (u_0), transverse displacement (w_0) and electric potential (φ_i) is derived as:

$$u_0^{''} = \beta_1 w_0^{'''} + \beta_2^i \tilde{\varphi}_i^{'} \tag{4.24}$$

where

$$\beta_1 = \frac{\left(\tilde{Q}^k_{11} I^k_1 + \left((\tilde{e}^i_{31})^2 / \tilde{\epsilon}^i_3\right)(I^i_1 - I^i_0 \bar{z}_i)\right)}{(\tilde{Q}^k_{11} I^k_0)}; \quad \beta_2^i = -\frac{(\tilde{e}^i_{31} I^i_0 / h_i)}{(\tilde{Q}^k_{11} I^k_0)}$$

Using Eqs. (4.20), (4.21) and (4.23), we can write the relation between section rotation (θ), transverse displacement (w_0) and electric potential (φ_i) as:

$$\theta = -w_0^{'} + \beta_3 w_0^{'''} + \beta_4^i \tilde{\varphi}_i^{'} \tag{4.25}$$

where

$$\beta_3 = \frac{\left(\tilde{Q}_{11}^k I_1^k + \left(\left(\tilde{e}_{31}^i\right)^2 / \tilde{\epsilon}_3^i\right)\left(I_1^i - I_0^i \bar{z}_i\right)\right)^2}{\left(\tilde{Q}_{11}^k I_0^k\right)\left(\tilde{Q}_{55}^k I_0^k\right)} - \frac{\left(\tilde{Q}_{11}^k I_2^k + \left(\left(\tilde{e}_{31}^i\right)^2 / \tilde{\epsilon}_3^i\right)\left(I_2^i - I_0^i \bar{z}_i^2\right)\right)}{\left(\tilde{Q}_{55}^k I_0^k\right)}$$

$$\beta_4^i = \frac{\left(\tilde{e}_{31}^i I_0^i \bar{z}_i / h_i\right)}{\left(\tilde{Q}_{55}^k I_0^k\right)} - \frac{\left[\tilde{Q}_{11}^k I_1^k + \left(\sum_{j=1}^{n_p} \left(\left(\tilde{e}_{31}^j\right)^2 / \tilde{\epsilon}_3^j\right)\left(I_1^j - I_0^j \bar{z}_j\right)\right)\right]}{\left(\tilde{Q}_{55}^k I_0^k\right)} \frac{\left(\tilde{e}_{31}^i I_0^i / h_i\right)}{\left(\tilde{Q}_{11}^k I_0^k\right)}$$

where n_p=total number of piezoelectric layers in the beam.

From Eqs. (4.24) and (4.25), it is clear that the coupling constants $\beta_m, (m = 1...4)$ depend on the geometric and material properties of the beam and these constants relate all field variables by properly accommodating bending-extension, bending-shear and induced potential couplings. These expressions are used in the next section to derive coupled polynomial expressions for field variables.

4.6 Finite Element Formulation

Using the variational formulation described above, a finite element model is developed here. For the two-noded finite element model developed here, the degrees of freedom consist of three mechanical (u_0, w_0 and θ) and layerwise electric potential variables ($\tilde{\varphi}_i$) where (i=1.....number of piezoelectric layers in the beam).

In terms of the natural coordinate (ξ), a cubic polynomial for transverse displacement (w_0) and linear polynomials for layerwise electric potentials ($\tilde{\varphi}_i$) are assumed as given in Eqs. (4.26a) and (4.26b), respectively. The transformation between coordinate ξ and global coordinate (x) along the length of the beam is given as $\xi = [2(x - x_1)/(x_2 - x_1)] - 1$ and $x_2 - x_1 = l$, length of the beam element.

$$w_0 = b_0 + b_1\xi + b_2\xi^2 + b_3\xi^3 \tag{4.26a}$$

$$\tilde{\varphi}_i = c_0^i + c_1^i\xi \tag{4.26b}$$

Using these polynomials for w_0 and $\tilde{\varphi}_i$ in equation (4.24) and integrating with respect to ξ, we get the coupled polynomial for midplane axial displacement (u_0) as:

$$u_0 = [(6\beta_1/l)b_3 + (\beta_2^i l/4)c_1^i]\xi^2 + a_1\xi + a_0 \tag{4.27}$$

Using Eqs. (4.26a) and (4.26b) in Eq. (4.25), the coupled polynomial for section rotation (θ) is obtained as:

$$\theta = -b_1(2/l) - b_2(2\xi(2/l)) - b_3\left(3\xi^2(2/l) - 6\beta_3(2/l)^3\right) + c_1^i(\beta_4^i(2/l)) \tag{4.28}$$

It is noteworthy that Eqs. (4.27) and (4.28) take care of bending-extension and bending-shear couplings along with the change in stiffness due to induced potential, in a variationally consistent manner. Although an assumed cubic polynomial for transverse displacement and quadratic polynomials for axial displacement and section rotation of the beam are used in the formulation, the number of nodal degrees of freedom are maintained the same as of the conventional formulation. The elemental shear strain field is given as:

$$\gamma_{xz} = \theta + w_0^{'} = b_3(6\beta_3(2/l)^3) + c_1^i(\beta_4^i(2/l)) \tag{4.29}$$

The above shear strain is constant over the element. Also, it does not lead to any spurious constraints in the thin limits, as the coefficients β_3 and β_4 tend to vanish as beam thickness approaches zero. Hence, no shear locking shall be experienced.

Using Eqs. (4.26a), (4.26b), (4.27) and (4.28), the coupled shape functions in Eq. (4.30) are derived by usual method.

$$\begin{Bmatrix} u_0 \\ w_0 \\ \theta \\ \tilde{\varphi}_i \end{Bmatrix} = \begin{bmatrix} N_1^u & N_2^u & N_3^u & N_4^{ui} & N_5^u & N_6^u & N_7^u & N_8^{ui} \\ 0 & N_1^w & N_2^w & N_3^{wi} & 0 & N_4^w & N_5^w & N_6^{wi} \\ 0 & N_1^\theta & N_2^\theta & N_3^{\theta i} & 0 & N_4^\theta & N_5^\theta & N_6^{\theta i} \\ 0 & 0 & 0 & N_1^{\varphi i} & 0 & 0 & 0 & N_2^{\varphi i} \end{bmatrix} \begin{Bmatrix} u_0^1 \\ w_0^1 \\ \theta^1 \\ \tilde{\varphi}_i^1 \\ u_0^2 \\ w_0^2 \\ \theta^2 \\ \tilde{\varphi}_i^2 \end{Bmatrix} \tag{4.30}$$

The expressions for these shape functions in natural coordinate system are given as:

$$\begin{aligned}
N_1^u &= \frac{(1-\xi)}{2}; & N_2^u &= \frac{3\beta_1 l}{24\beta_3 - 2l^2}(1-\xi^2);\\
N_3^u &= \frac{3\beta_1 l^2}{48\beta_3 - 4l^2}(\xi^2-1); & N_4^{ui} &= \frac{\beta_2^i l^3 + 12l(\beta_1\beta_4^i - \beta_2^i\beta_3)}{96\beta_3 - 8l^2}(\xi^2-1);\\
N_5^u &= \frac{(1+\xi)}{2} & N_6^u &= \frac{3\beta_1 l}{24\beta_3 - 2l^2}(\xi^2-1);\\
N_7^u &= \frac{3\beta_1 l^2}{48\beta_3 - 4l^2}(\xi^2-1); & N_8^{ui} &= \frac{\beta_2^i l^3 + 12l(\beta_1\beta_4^i - \beta_2^i\beta_3)}{96\beta_3 - 8l^2}(1-\xi^2);
\end{aligned}$$

$$\begin{aligned}
N_1^w &= \frac{1}{2} - \frac{l^2\xi^3 + \xi(24\beta_3 - 3l^2)}{48\beta_3 - 4l^2}; & N_2^w &= \left[\frac{l}{8} + \frac{l^3\xi}{96\beta_3 - 8l^2}\right](\xi^2-1);\\
N_3^{wi} &= \frac{\beta_4^i l^2\xi}{48\beta_3 - 4l^2}(\xi^2-1); & N_4^w &= \frac{1}{2} + \frac{l^2\xi^3 + \xi(24\beta_3 - 3l^2)}{48\beta_3 - 4l^2};\\
N_5^w &= \left[\frac{l}{8} - \frac{l^3\xi}{96\beta_3 - 8l^2}\right](1-\xi^2); & N_6^{wi} &= \frac{\beta_4^i l^2\xi}{48\beta_3 - 4l^2}(1-\xi^2);
\end{aligned}$$

$$\begin{aligned}
N_1^\theta &= \frac{3l}{24\beta_3 - 2l^2}(\xi^2-1); & N_2^\theta &= \frac{24\beta_3 + l^2(1-3\xi^2)}{48\beta_3 - 4l^2} - \frac{\xi}{2};\\
N_3^{\theta i} &= \frac{3\beta_4^i l}{24\beta_3 - 2l^2}(1-\xi^2); & N_4^\theta &= \frac{3l}{24\beta_3 - 2l^2}(1-\xi^2);\\
N_5^\theta &= \frac{24\beta_3 + l^2(1-3\xi^2)}{48\beta_3 - 4l^2} + \frac{\xi}{2}; & N_6^{\theta i} &= \frac{3\beta_4^i l}{24\beta_3 - 2l^2}(\xi^2-1);
\end{aligned}$$

$$N_1^{\varphi i} = \frac{(1-\xi)}{2}; \qquad N_2^{\varphi i} = \frac{(1+\xi)}{2};$$

Now, the variation on the basic mechanical and electrical variables can be transferred to nodal degrees of freedom. Substituting Eq. (4.30) in Eqs. (4.15), (4.17), (4.18) and using them in equation (4.12), we get the descretized form of finite element equations as:

$$\begin{bmatrix} \begin{bmatrix} M \end{bmatrix} & 0 \\ 0 & 0 \end{bmatrix} \begin{bmatrix} \left\{\ddot{U}\right\} \\ \left\{\ddot{\Phi}\right\} \end{bmatrix} + \begin{bmatrix} \begin{bmatrix} K_{uu} \end{bmatrix} & \begin{bmatrix} K_{u\varphi} \end{bmatrix} \\ \begin{bmatrix} K_{\varphi u} \end{bmatrix} & \begin{bmatrix} K_{\varphi\varphi} \end{bmatrix} \end{bmatrix} \begin{bmatrix} \left\{U\right\} \\ \left\{\Phi\right\} \end{bmatrix} = \begin{bmatrix} \left\{F\right\} \\ \left\{Q\right\} \end{bmatrix} \tag{4.31}$$

where M is the mass matrix. $K_{uu}, K_{u\varphi}, K_{\varphi u}, K_{\varphi\varphi}$ are the global stiffness sub-matrices. U, Φ are the global mechanical and electrical nodal degrees of freedom vectors, respectively. F and Q are global mechanical and electrical nodal force vectors, respectively. These matrix equations now can be solved according to the electrical conditions (closed/open circuit) and mode of operation (actuation/sensing) for static/dynamic analyses.

4.7 Numerical Examples and Discussions

The proposed formulation is validated here for accuracy and efficiency in static (actuation and sensing) and modal analyses (open and closed circuit) of piezoelectric smart beams. The software implementation has been carried out in MATLAB environment. The performance of the present formulation is compared against the conventional two-noded isoparametric FSDT formulations available in the literature and 2D finite element simulation using ANSYS software. The finite element formulations used for the comparative study are designated here as:

> **FSDT-*Coupled*** : The present formulation which uses coupled polynomials (cubic for w_0 given by Eq. (4.26a), coupled quadratic for u_0 given by Eq. (4.27), coupled quadratic for θ given by Eq. (4.28) and linear for $\tilde{\varphi}_i$ given by Eq. (4.26b)) for interpolation of field variables and layerwise consistent through-thickness potential (coupled quadratic approximation in z direction given by Eq. (4.10)). It does not employ any sublayers within the piezoelectric layer, for modelling. This formulation is expected to be free from piezolocking, shear locking and material locking.
>
> **FSDT** : The conventional FSDT formulation (Narayanan and Balamurugan, 2003) which uses independent polynomials for field interpolation (linear for u_0, w_0, θ and $\tilde{\varphi}_i$) and assumed linear through-thickness potential in each physical piezoelectric layer. This element suffers from piezolocking, shear locking and material locking. The traditional *Reduced Integration* technique has been used to eliminate shear locking in this element.
>
> **FSDT (with sublayers)** : The piezolocking in the above FSDT model may be eliminated by using a sufficient number of sublayers for modelling each piezoelectric layer. The through-thickness distribution of potential in each piezolayer

is represented by sublayer-wise linear approximations. In this sublayered version of FSDT, we have used *four sublayers* per physical piezoelectric layer, which are found adequate to yield reasonably accurate results. However, each sublayer would introduce an additional nodal electric potential degree of freedom and hence this element is computationally expensive.

ANSYS 2D : For a comparative evaluation of the above FSDT formulations, benchmark solutions have been obtained from a refined 2-dimensional analysis using ANSYS finite element software (ANSYS-Release12, 2009), for which PLANE 183 elements are used to mesh conventional material layers, while PLANE 223 elements are used to mesh piezoelectric material layers.

4.7.1 Example 1: A three-layer symmetric piezoelectric beam

The example chosen here is an aluminum core with surface bonded oppositely poled piezoelectric layers of PZT 5H material, as shown in Fig. 4.2. The material properties of the beam are (Kapuria and Hagedorn, 2007):
Aluminum: $E = 70.3\ GPa$, $\nu = 0.345$, $\rho = 2710\ kgm^{-3}$
PZT 5H: $C_{11} = C_{22} = 126\ GPa$, $C_{12} = 79.5\ GPa$, $C_{13} = C_{23} = 84.1\ GPa$, $C_{33} = 117\ GPa$, $C_{44} = C_{55} = 23\ GPa, C_{66} = 23.25\ GPa$, $e_{31} = e_{32} = -6.5\ Cm^{-2}$, $e_{33} = 23.3\ Cm^{-2}$, $\epsilon_{33} = 1.3 \times 10^{-8}\ Fm^{-1}$, $\rho = 7500\ kgm^{-3}$ (The reduced properties used are: $\tilde{Q}_{11} = 60.013\ GPa, \tilde{Q}_{55} = 23\ GPa, \tilde{e}_{31} = -16.4921\ Cm^{-2}, \tilde{\epsilon}_3 = 2.5885 \times 10^{-8}\ Fm^{-1}$)

This example is expected to show the improvement in terms of accuracy and efficiency of the present FSDT-*Coupled* formulation over the conventional FSDT. To study the performance of the FSDT-based smart beam formulations over a wide range of piezoelectric material proportion in the total thickness (Thickness ratio: $r = (2h_p)/h$), the length (L) and total height (h) are taken as constant with values $100\ mm$ and $10\ mm$, respectively, while the thicknesses of piezoelectric layer (h_p) and aluminum layer (h_{al}) are varied. For a comparative evaluation of the various FSDT formulations, converged results from ANSYS 2D analysis with a refined mesh size of 100×40 are used.

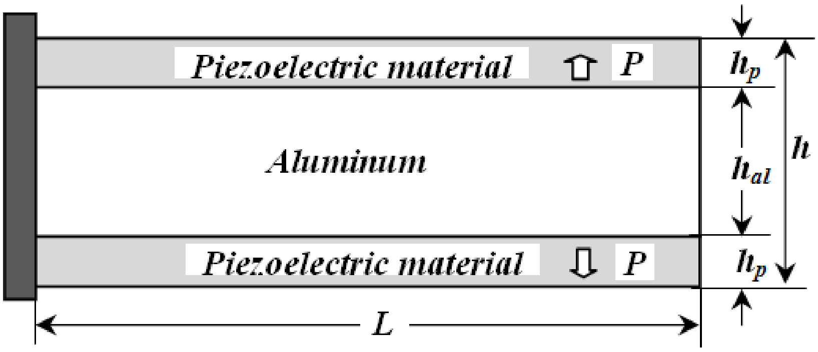

Figure 4.2: Example 1: Geometry of the three-layer cantilever beam with symmetrically bonded oppositely poled piezoelectric layers in extension mode.

Static analysis: Actuator configuration

For actuator configuration, the interfaces of piezoelectric layers with aluminum layer are grounded and potentials of $\pm 10\ volts$ are applied on the free surfaces of the piezoelectric layer. The variation of tip deflection over a wide range of thickness ratio is plotted in Fig. 4.3.

It is evident that the present FSDT-*Coupled* formulation gives accurate results as that of ANSYS 2D simulation. In the higher thickness ratio regimes, the conventional FSDT formulation converges to inaccurate results due to piezolocking effect. It demands sublayered modelling to achieve the same level of accuracy as of the present formulation. The results clearly show the advantage of FSDT-*Coupled* formulation, to efficiently handle the piezolocking effects.

The variation of error (%) in the tip deflection due to use of conventional FSDT formulation with thickness ratio is plotted in Fig. 4.4. As the proportion of piezoelectric material in the beam increases, the error due to the linear assumption of through-thickness potential becomes significant. The maximum difference is observed for a beam of pure piezoelectric material i.e. a *bimorph* configuration. Hence, the bimorph shown in Fig. 4.5 is considered for a detailed study of the induced potential effects.

Table 4.1 shows the results for the tip deflection of the bimorph for various numbers of sublayers in the modelling with FSDT formulation of Narayanan and Balamurugan (2003). As seen from results, only with sufficient number of sublayers in the modelling of piezoelectric layers, the conventional FSDT formulation converges to the accurate

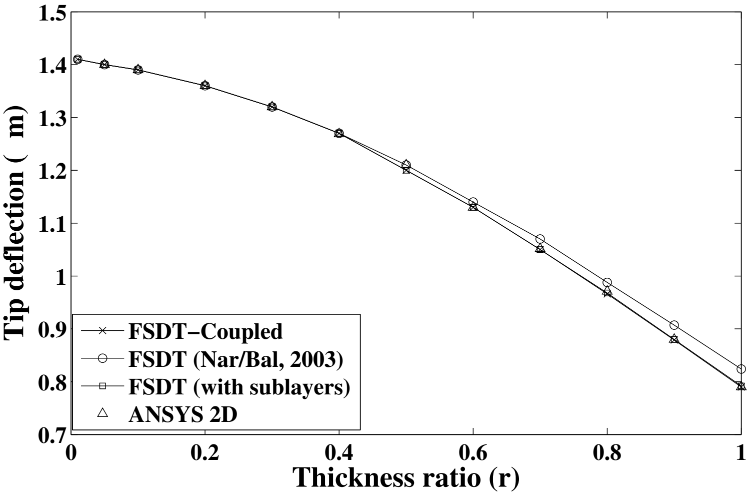

Figure 4.3: Example 1: Actuator configuration: Variation of the tip deflection with thickness ratio (r) for the three-layer cantilever beam actuated by $\pm 10\ volts$.

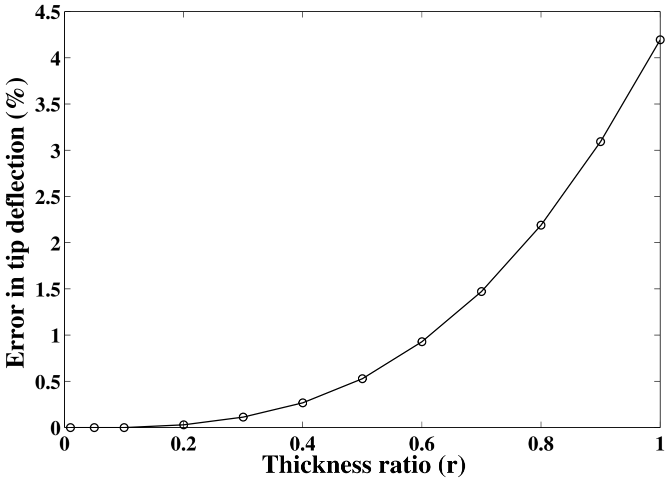

Figure 4.4: Example 1: Actuator configuration: Variation of error (%) in the tip deflection with thickness ratio (r), due to use of the conventional FSDT formulation for the three-layer cantilever beam actuated by $\pm 10\ volts$.

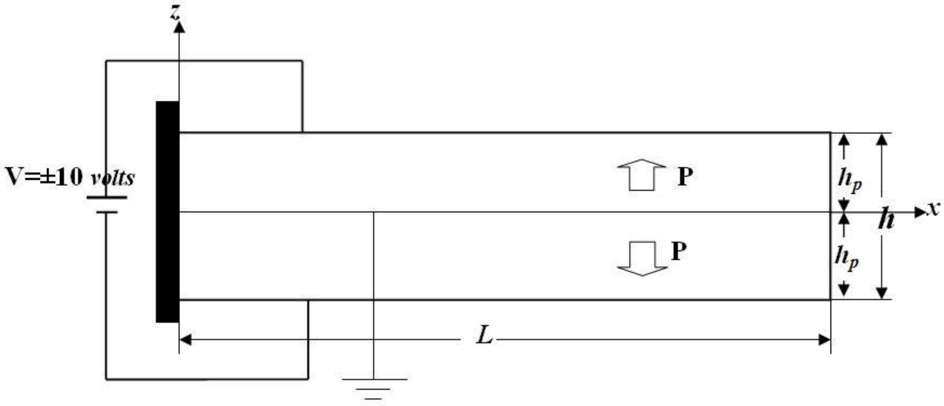

Figure 4.5: Example 1: Bimorph cantilever beam in the actuator configuration.

Table 4.1: Example 1: Actuator configuration: Tip deflection of the bimorph cantilever beam actuated by $\pm 10\, volts$ ($h = 10\, mm,\ L = 100\, mm$).

Formulation	Tip deflection (μm)
FSDT (Nar/Bal, 2003)	0.824
FSDT (with sublayers)	
2 sublayers/layer	0.798
4 sublayers/layer	0.792
ANSYS 2D	0.790
FSDT-*Coupled*	0.789

values as predicted by FSDT-*Coupled* and ANSYS 2D simulation.

Also, the comparison of results for transverse deflection along the length, through-thickness distributions of potential and axial stress for the bimorph are plotted in Figs. 4.6, 4.7 and 4.8, respectively. The results prove the ability of FSDT-*Coupled* to model the piezoelectric beam accurately as of ANSYS 2D and FSDT (with sublayers). The conventional FSDT formulation of Narayanan and Balamurugan (2003) suffers from loss of accuracy due to piezolocking.

Static analysis: Sensor configuration

For sensor configuration, the three-layer cantilever beam shown in Fig. 4.2 is subjected to a tip load of $-1000\ N$. The results for tip deflection and potential developed at mid-

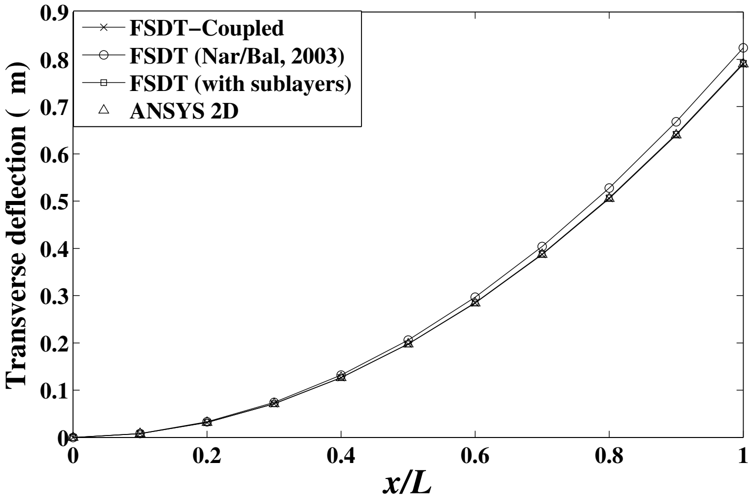

Figure 4.6: Example 1: Actuator configuration: Transverse deflection along the length of the bimorph cantilever beam actuated by ±10 $volts$.

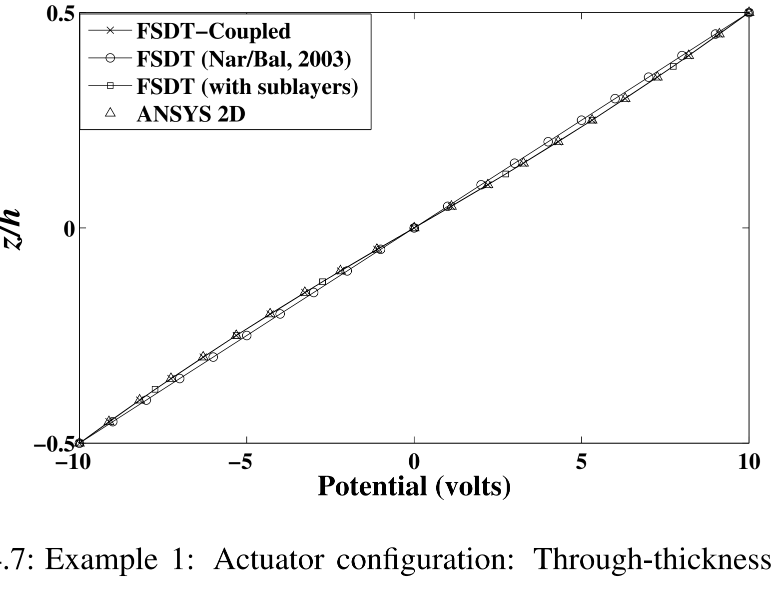

Figure 4.7: Example 1: Actuator configuration: Through-thickness potential distribution in the bimorph cantilever beam actuated by ±10 $volts$.

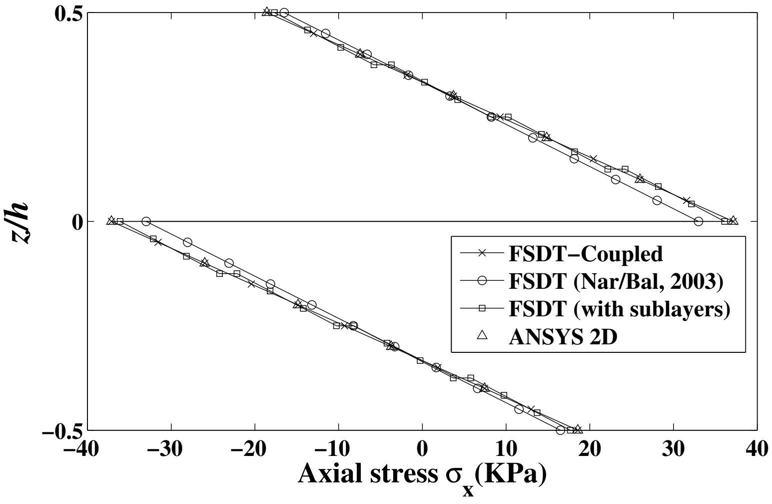

Figure 4.8: Example 1: Actuator configuration: Through-thickness axial stress distribution in the bimorph cantilever beam actuated by $\pm 10\ volts$.

span are plotted in Figs. 4.9 and 4.10, for various thickness ratios. From these plots, it is clear that present FSDT-*Coupled* formulation is able to yield accurate results as that of ANSYS 2D simulation over the entire range of thickness ratio. The conventional FSDT formulation of Narayanan and Balamurugan (2003) suffers form piezolocking and does not maintain the accuracy consistently. It demands sublayered modelling to achieve same accuracy as that of FSDT-*Coupled*. The inaccuracy due to piezolocking is quantified in the error (%) plotted in Fig. 4.11. The variation of error (%) with thickness ratio shows that as we move from a beam of purely conventional material to a purely piezoelectric material beam i.e. bimorph, the error in the results increases significantly. Hence, the bimorph structure shown in Fig. 4.12 is considered here for detailed study of the induced potential effects.

Table 4.2 shows the results for tip deflection and potential developed across each piezoelectric layer at mid-span of the bimorph, for different number of sublayers in the modelling with conventional FSDT formulation of Narayanan and Balamurugan (2003). As seen from results, only with a sufficient number of sublayers in the modelling of piezoelectric layers, the conventional formulation converges to the accurate results as predicted by FSDT-*Coupled* and ANSYS 2D simulation.

Also, the results for transverse deflection along the length, potential developed across each layer along the length, through-thickness potential at mid-span and axial stress distributions at the root of the bimorph are plotted in Figs. 4.13, 4.14, 4.15

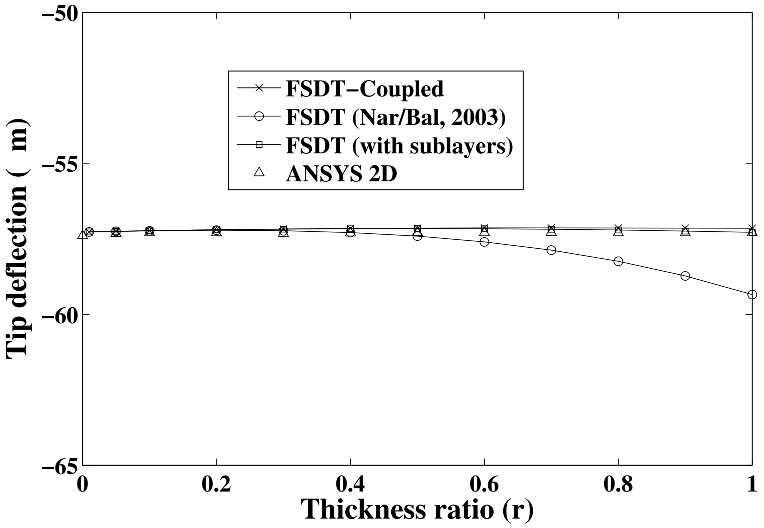

Figure 4.9: Example 1: Sensor configuration: Variation of the tip deflection with thickness ratio (r) for the three-layer cantilever beam subjected to a tip load of $-1000\ N$.

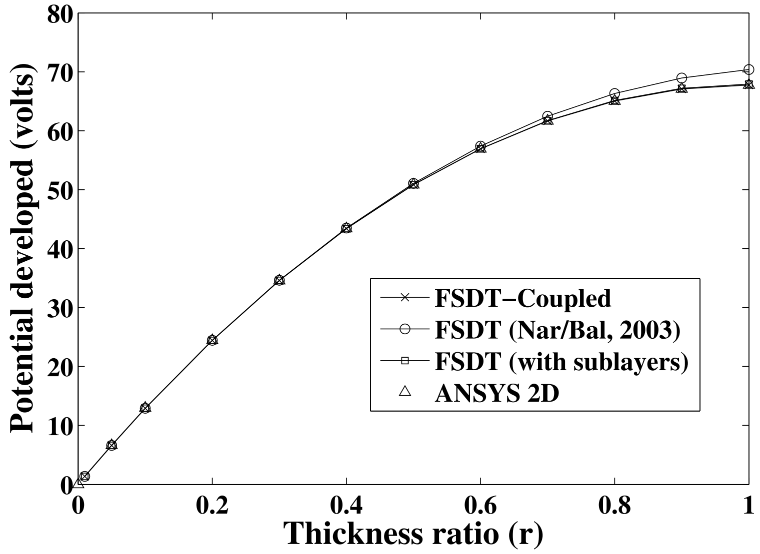

Figure 4.10: Example 1: Sensor configuration: Variation of the potential developed across each piezoelectric layer at the mid-span with thickness ratio (r) for the three-layer cantilever beam subjected to a tip load of $-1000\ N$.

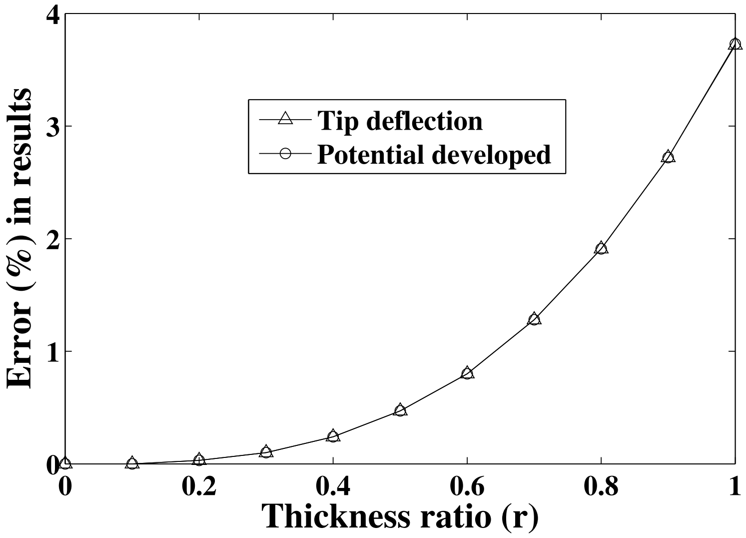

Figure 4.11: Example 1: Sensor configuration: Variation of error ($\%$) in the tip deflection and the potential developed with thickness ratio (r), due to use of the conventional FSDT formulation for the three-layer cantilever beam subjected to a tip load of $-1000\ N$.

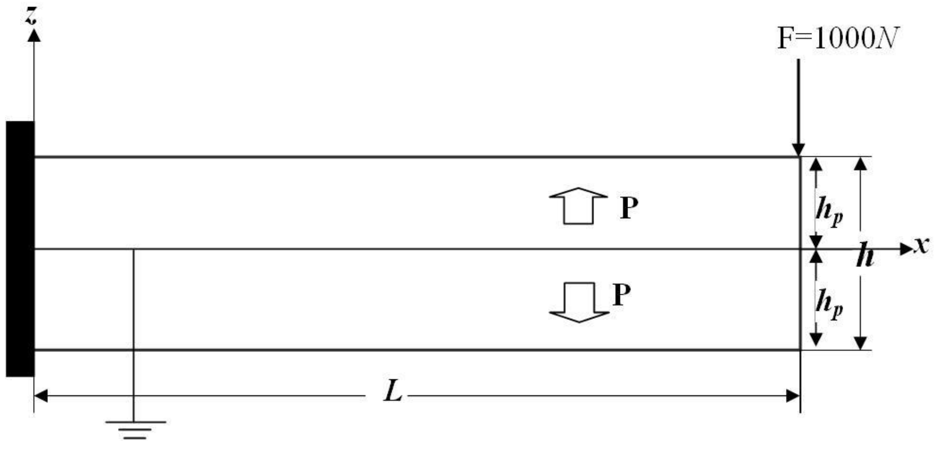

Figure 4.12: Example 1: Bimorph cantilever beam in the sensor configuration.

Table 4.2: Example 1: Sensor configuration: Tip deflection and potential developed at the mid-span of the bimorph cantilever beam subjected to a tip load of $-1000\ N$ ($h = 10\ mm,\ L = 100\ mm$).

Formulation	Tip deflection (μm)	Potential ($volts$)
FSDT (Nar/Bal, 2003)	-59.3	70.38
FSDT (with sublayers)		
2 sublayers/layer	-57.7	68.40
4 sublayers/layer	-57.3	67.91
ANSYS 2D	-57.2	67.76
FSDT-*Coupled*	-57.2	67.75

and 4.16, respectively. It is evident from the figures that results of the present FSDT-*Coupled* formulation closely match with 2D simulation, while conventional FSDT formulation of Narayanan and Balamurugan (2003) needs sublayered model to eliminate loss of accuracy due to piezolocking. It may be noted that in Fig. 4.16, the conventional FSDT formulation exhibit a large discontinuity in the axial stress at the interface which tend to disappear with addition of sufficient number of sublayers.

Figs. 4.17 and 4.18 show the comparison of convergence characteristics of the FSDT-based piezoelectric beam finite element formulations, for the tip deflection and potential developed at the root of the bimorph, respectively. It is noteworthy that FSDT-*Coupled* shows single-element convergence, closely reproducing the ANSYS-2D solutions for both the tip deflection and the potential developed. As evident from these figures, both the conventional FSDT (Narayanan and Balamurugan, 2003) and FSDT (with sublayers) models show a similar pattern of slow convergence. It is observed that the sublayered FSDT model eventually converges to the accurate results for tip deflection ($= -57.213\ \mu m$) and potential ($= 135.52\ volts$). However, the conventional FSDT (Narayanan and Balamurugan, 2003) model overestimates the response and converges to inaccurate results, due to piezolocking effects. This example clearly reveals the role of the coupled polynomial interpolation in improving the accuracy and efficiency of the FSDT-based piezoelectric beam finite elements.

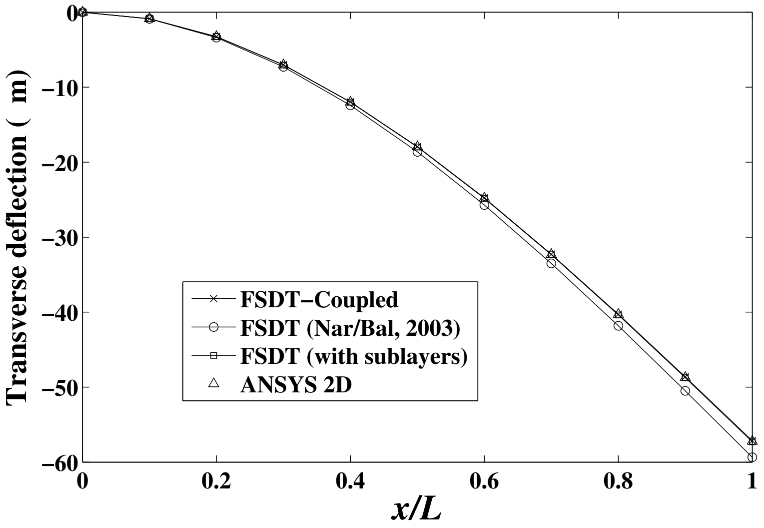

Figure 4.13: Example 1: Sensor configuration: Transverse deflection along the length of the bimorph cantilever beam subjected to a tip load of $-1000\ N$.

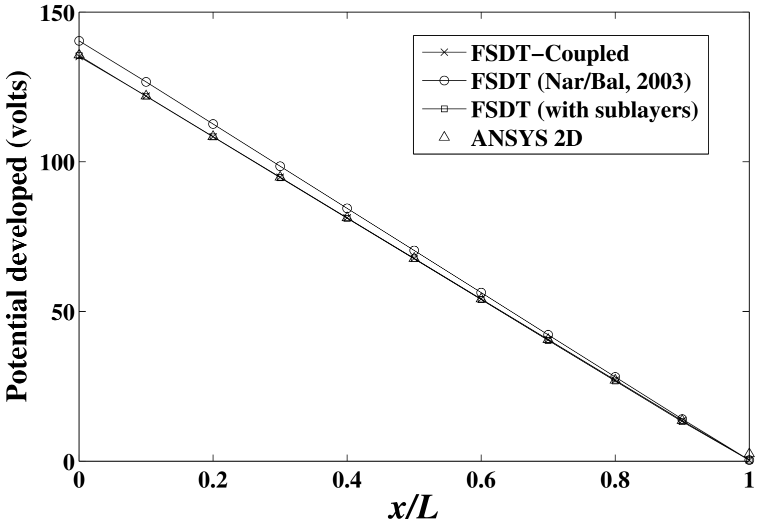

Figure 4.14: Example 1: Sensor configuration: Potential developed across each piezoelectric layer along the length of the bimorph cantilever beam subjected to a tip load of $-1000\ N$.

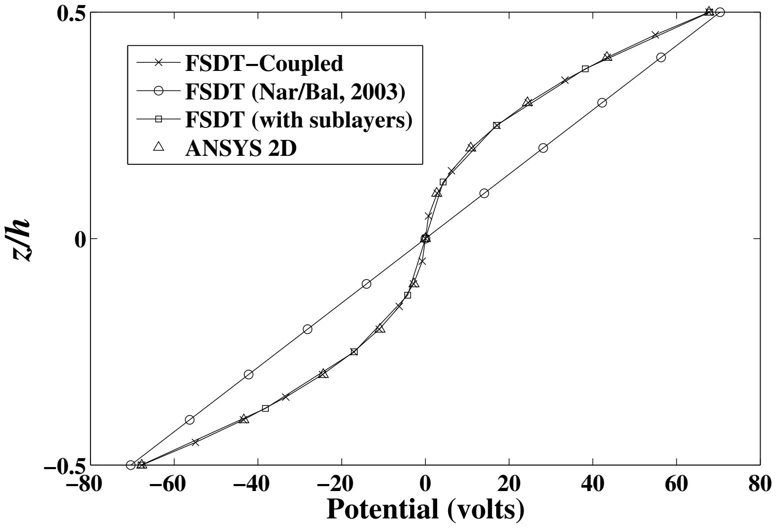

Figure 4.15: Example 1: Sensor configuration: Through-thickness potential distribution at the mid-span of the bimorph cantilever beam subjected to a tip load of $-1000\ N$.

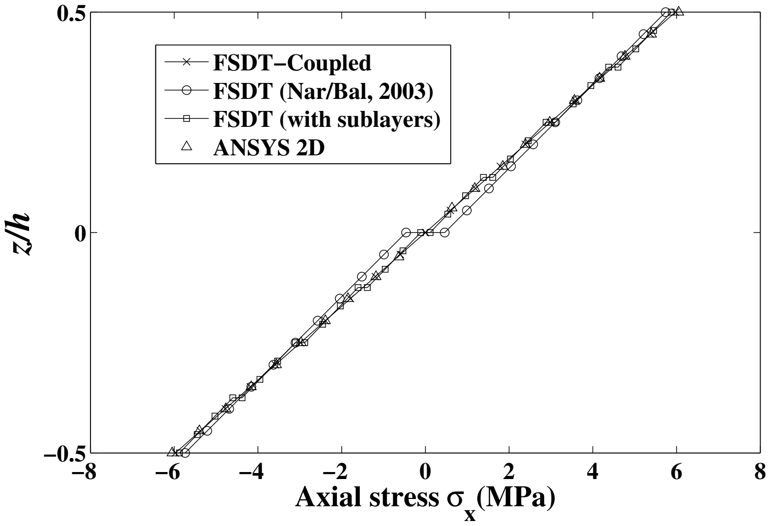

Figure 4.16: Example 1: Sensor configuration: Through-thickness axial stress distribution at the root of the bimorph cantilever beam subjected to a tip load of $-1000\ N$.

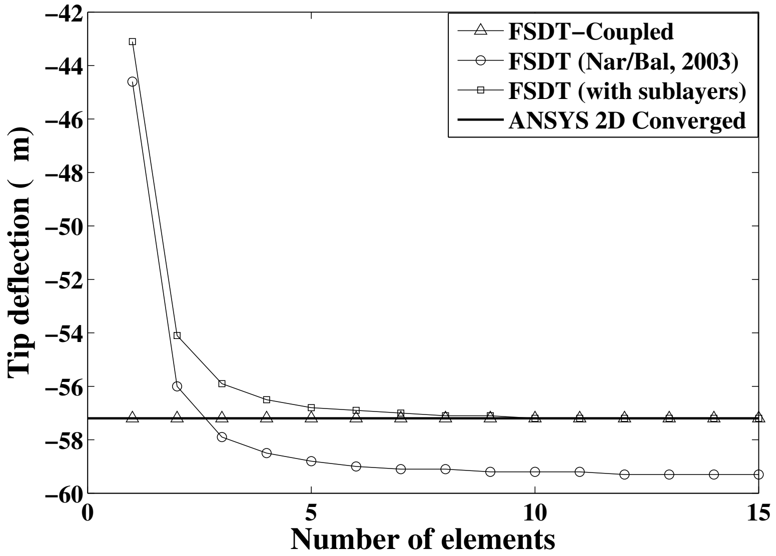

Figure 4.17: Example 1: Sensor configuration: Convergence characteristics of the FSDT-based piezoelectric beam finite elements to predict the tip deflection of the bimorph cantilever beam subjected to a tip load of $-1000\ N$.

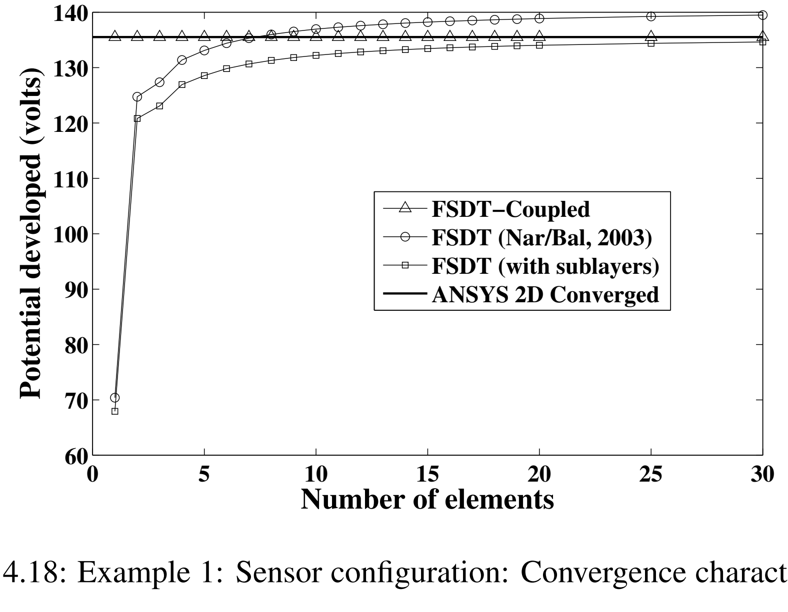

Figure 4.18: Example 1: Sensor configuration: Convergence characteristics of the FSDT-based piezoelectric beam finite elements to predict the potential developed across a piezoelectric layer at the root of the bimorph cantilever beam subjected to a tip load of $-1000\ N$.

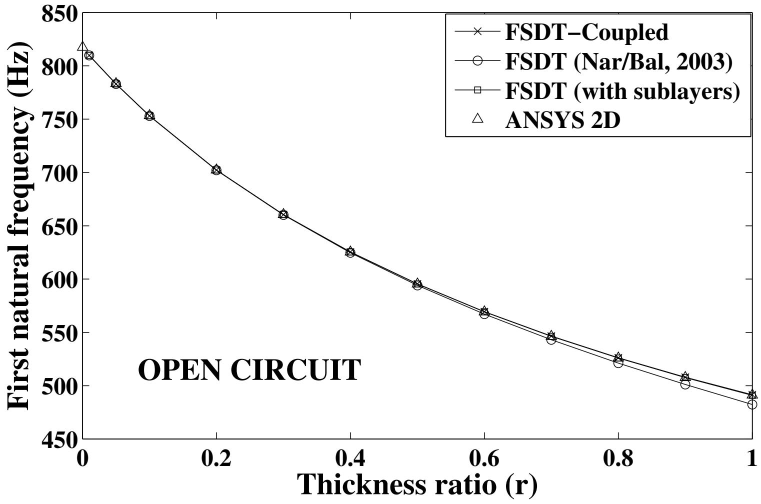

Figure 4.19: Example 1: Modal analysis: Variation of the first natural frequency with thickness ratio (r) for the three-layer cantilever beam in open circuit electrical boundary condition.

Modal analysis

The present formulation is validated here for accuracy and efficiency to predict natural frequencies of the smart cantilever shown in Fig. 4.2. The natural frequencies are evaluated for closed and open circuit electrical boundary conditions. For open circuit, only the interfaces of piezoelectric layers with aluminum core are grounded while, for closed circuit all the faces of piezoelectric layers are grounded. The variations of first natural frequencies in open and closed circuit electrical boundary conditions, with thickness ratio are plotted in Figs. 4.19 and 4.20, respectively. As seen from the figures, the present FSDT-*Coupled* predicts the accurate results as given by ANSYS 2D simulation over the entire range of thickness ratio. The conventional FSDT formulation shows significant errors due to piezolocking in the higher thickness ratio regimes and requires sublayered modelling to achieve accurate results. The variation of errors (%) with thickness ratio is plotted in Fig. 4.21. As seen from the figure, the bimorph configuration shows maximum error.

The results for first three natural frequencies for the bimorph cantilever are tabulated in Table 4.3. As seen from the results the conventional FSDT formulation suffers form piezolocking and requires a number of sublayers to reproduce accurate results.

Figs. 4.22 and 4.23 show the comparison of convergence characteristics of FSDT-

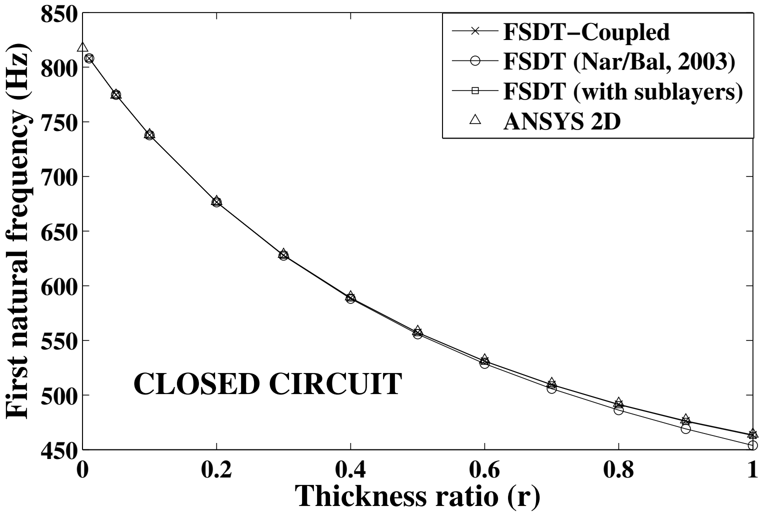

Figure 4.20: Example 1: Modal analysis: Variation of the first natural frequency with thickness ratio (r) for the three-layer cantilever beam in closed circuit electrical boundary condition.

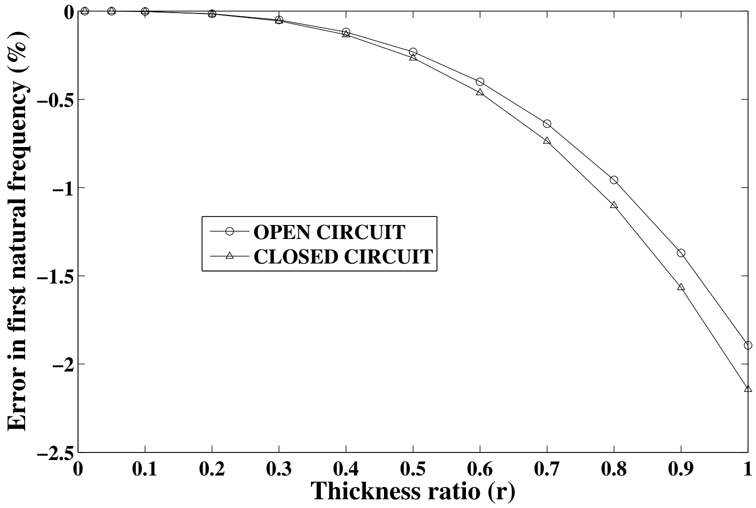

Figure 4.21: Example 1: Modal analysis: Variation of error (%) in the first natural frequency with thickness ratio (r), due to use of the conventional FSDT formulation for the three-layer cantilever beam.

Table 4.3: Example 1: Natural frequencies in Hz for the bimorph cantilever beam ($h = 10\,mm,\ L = 100\,mm$).

Electrical Boundary condition	Mode No	FSDT (Nar/Bal, 2003)	FSDT (with sublayers)	ANSYS 2D	FSDT *Coupled*
Open	1^{st}	482.4	491.0	491.2	491.5
Circuit	2^{nd}	2898	2944	2929	2949
	3^{rd}	7650	7666	7658	7666
Closed	1^{st}	453.8	462.9	464.3	463.5
Circuit	2^{nd}	2736	2788	2783	2792
	3^{rd}	7072	7072	7093	7072

based piezoelectric beam finite element formulations, to predict the first natural frequency in open and closed circuit electrical boundary conditions, respectively. It is noteworthy that FSDT-*Coupled* shows very fast convergence, accurately reproducing the ANSYS-2D solutions. As evident from these figures, the conventional FSDT and FSDT (with sublayers) formulations exhibit poor convergence. Both conventional FSDT and subalyered FSDT models show the similar pattern of slow convergence. It is observed that the sublayered FSDT model eventually converges to the accurate results for open circuit ($= 491.23\ Hz$) and closed circuit ($= 464.29\ Hz$). However, the conventional FSDT model (Narayanan and Balamurugan, 2003) underestimates the response and converges to inaccurate results, due to piezolocking effects. This example clearly reveals the efficiency of the present coupled polynomial interpolation over the conventional independent polynomial interpolations.

4.7.2 Example 2: A two-layer asymmetric piezoelectric beam

The test problem chosen here is a two-layer asymmetric piezoelectric cantilever beam having a host layer made up of steel with a surface bonded piezoelectric layer of G1195N material at the top, as shown in Fig. 4.24. The material properties used are:
Steel (Carrera and Brischetto, 2008): $E = 210\ GPa$, $\nu = 0.3$, $\rho = 7850\ kgm^{-3}$
PZT G1195N (Peng et al., 1998): $E = 63\ GPa$, $\nu = 0.3$, $d_{31} = 254 \times 10^{-12}\ m/V$,

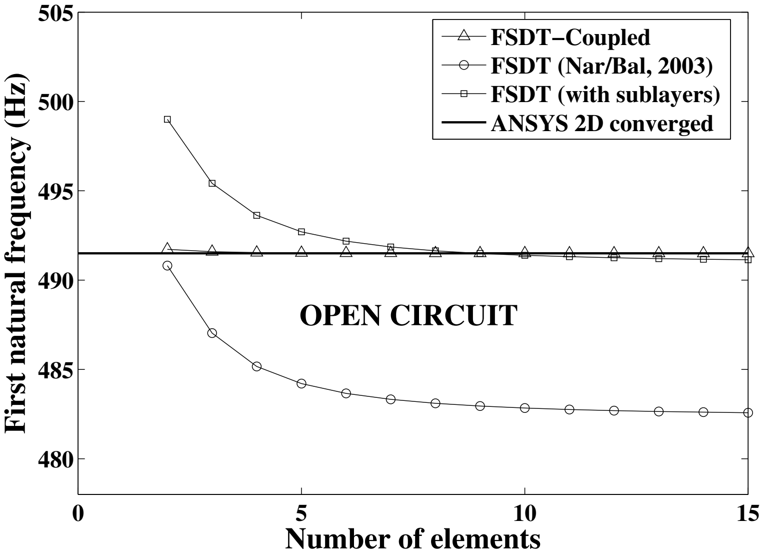

Figure 4.22: Example 1: Modal analysis: Convergence characteristics of the FSDT-based piezoelectric beam finite elements to predict the first natural frequency of the bimorph cantilever beam in open circuit electrical boundary condition.

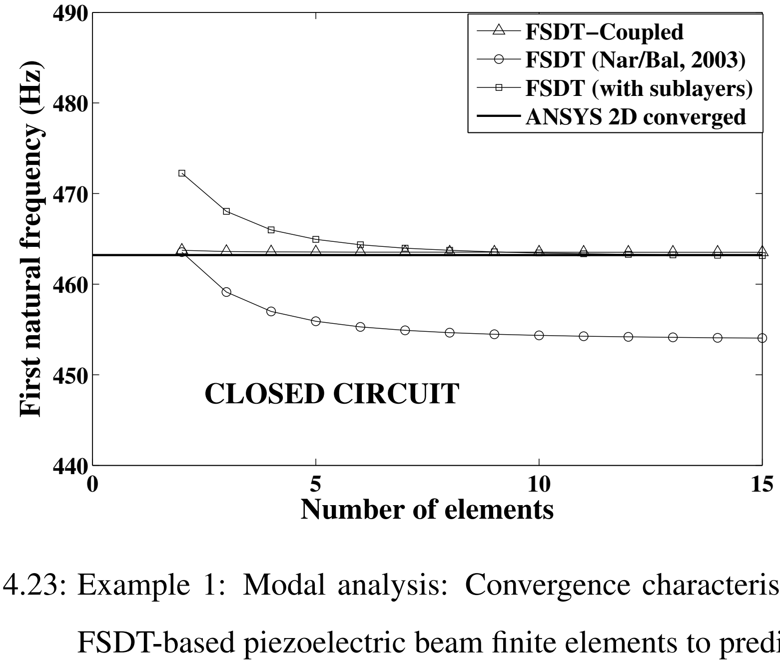

Figure 4.23: Example 1: Modal analysis: Convergence characteristics of the FSDT-based piezoelectric beam finite elements to predict the first natural frequency of the bimorph cantilever beam in closed circuit electrical boundary condition.

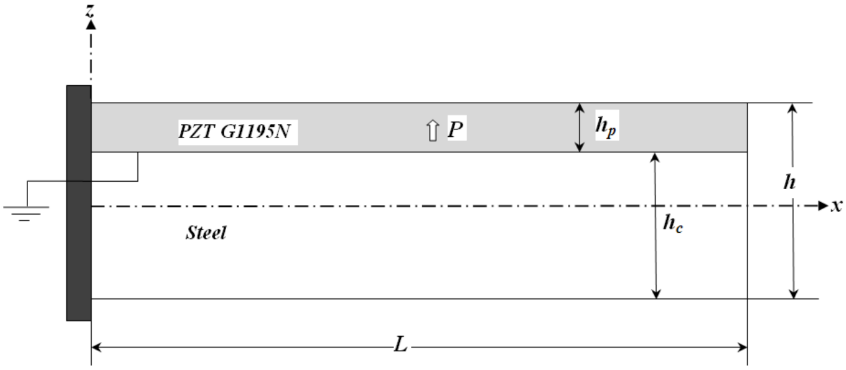

Figure 4.24: Example 2: Geometry of the two-layer cantilever beam with an asymmetrically bonded piezoelectric layer in extension mode.

$\epsilon_3 = 15 \times 10^{-9}\ F/m$, $\rho = 7600\ kgm^{-3}$.

This configuration is expected to show, in addition to piezolocking, the adverse effects of material locking on the convergence of the conventional FSDT piezoelectric beam finite elements and improved performance of the proposed FSDT-*Coupled* formulation.

For the present study, the length and total height of the beam are taken as constant ($L = 100\ mm$, $h = 5\ mm$), while thicknesses of the piezoelectric layer (h_p) and the host layer (h_c) are varied. The performances of the FSDT-based piezoelectric beam finite elements are evaluated over a wide range of piezoelectric material proportion in the total beam thickness (thickness ratio: $r = h_p/h$). For a comparative evaluation of various FSDT-based formulations, the converged results from ANSYS 2D simulation with a mesh of 200×20 elements are used.

Static analysis: Sensor configuration

For sensor configuration, the beam shown in Fig. 4.24 is subjected to a tip load of $-1000\ N$. The variations of tip deflection, axial deflection and potential developed across the piezoelectric layer at the root of the beam, with thickness ratio are plotted in Figs. 4.25, 4.26 and 4.27, respectively.

As seen from these graphs, the present FSDT-*Coupled* formulation consistently gives accurate predictions of the results as given by ANSYS 2D simulation, over the

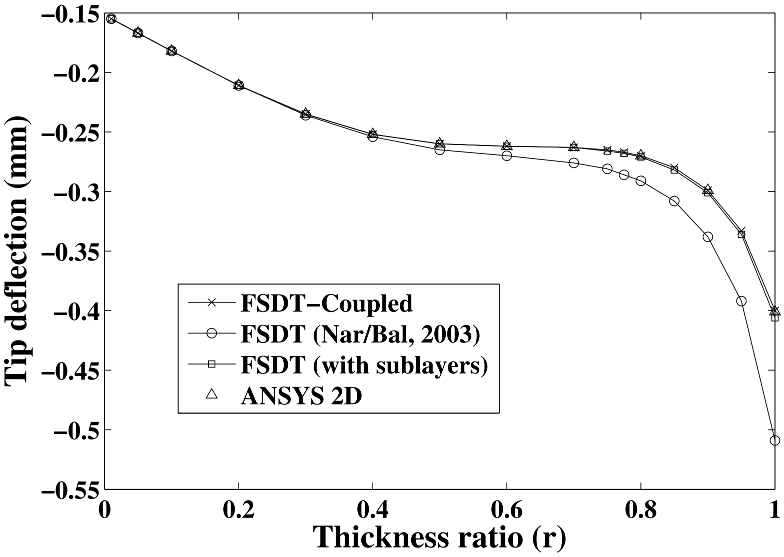

Figure 4.25: Example 2: Sensor configuration: Variation of the tip deflection with thickness ratio (r) for the asymmetric cantilever beam subjected to a tip load of $-1000N$.

entire range of thickness ratio and proves the versatility of the coupled polynomial based formulation. Due to the piezolocking effects, the conventional FSDT formulation (Narayanan and Balamurugan, 2003) does not perform consistently accurate. It demands sublayers in the modelling of piezolayer, to achieve the same consistent level of accuracy as of the present FSDT-*Coupled* formulation. The error ($\%$) due to piezolocking in the conventional FSDT formulation is quantified in Fig. 4.28 for various thickness ratios. It is seen that the error increases rapidly in the higher thickness ratio regimes.

Figs. 4.29 and 4.30 show the comparison of convergence characteristics of FSDT-based piezoelectric beam finite element formulations, for the tip deflection and the potential developed at the root, respectively. It is noteworthy that FSDT-*Coupled* shows single-element convergence, closely reproducing the ANSYS-2D solutions. Both conventional FSDT (Narayanan and Balamurugan, 2003) and FSDT (with sublayers) models show slow convergence patterns which are similar. It is observed that the sublayered FSDT model eventually converges to the accurate results for tip deflection ($= -0.2598\ mm$) and potential ($= 376.09\ volts$). However, the conventional FSDT model (Narayanan and Balamurugan, 2003) overestimates the response and converges to inaccurate results, due to piezolocking effects. This example clearly reveals the efficiency of the present coupled polynomial interpolation over the conventional indepen-

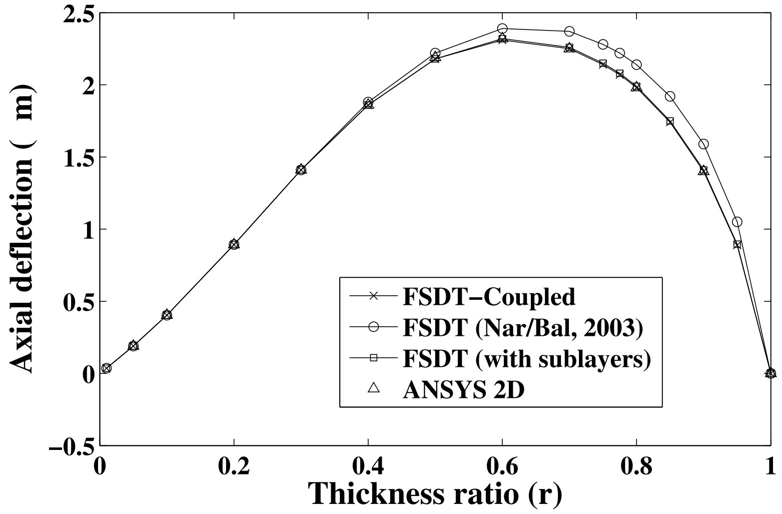

Figure 4.26: Example 2: Sensor configuration: Variation of the axial deflection with thickness ratio (r) for the asymmetric cantilever beam subjected to a tip load of $-1000N$.

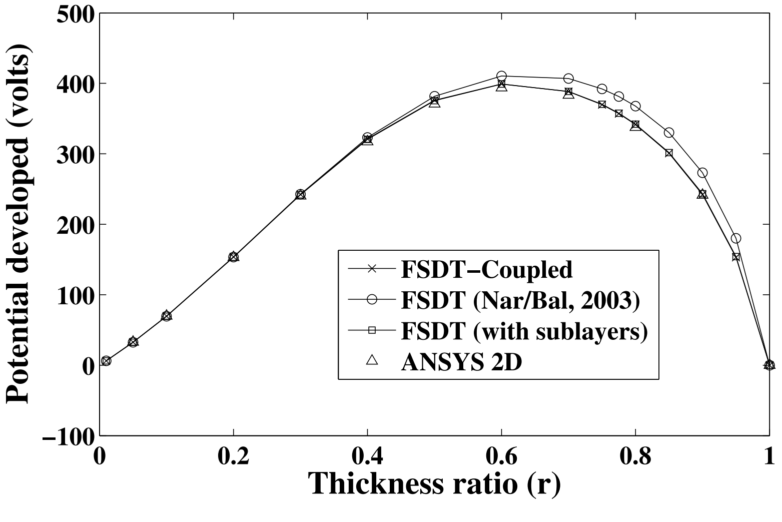

Figure 4.27: Example 2: Sensor configuration: Variation of the potential developed across piezoelectric layer at the root with thickness ratio (r) for the asymmetric cantilever beam subjected to a tip load of $-1000\ N$.

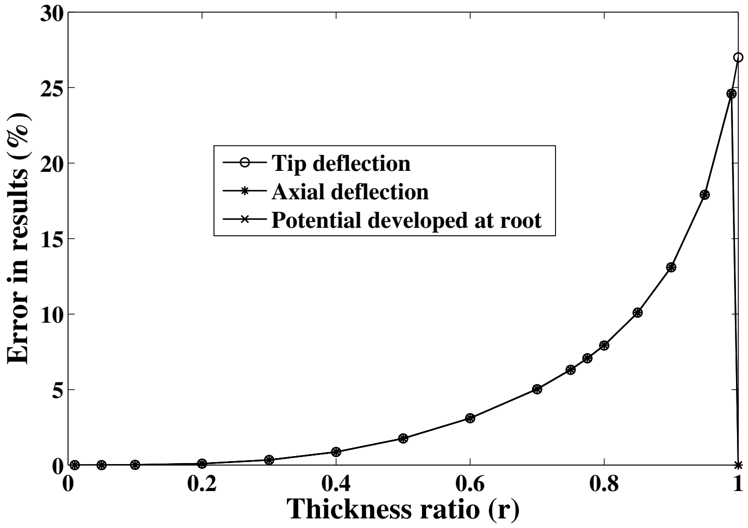

Figure 4.28: Example 2: Sensor configuration: Variation of error $(\%)$ in results with thickness ratio (r), due to use of the conventional FSDT formulation.

dent polynomial interpolations.

The improved performance of the FSDT-*Coupled* can be attributed to the coupled polynomial representations of section rotation and axial displacement. The role of the coupled quadratic term in the axial displacement given by Eq. (4.27), in eliminating material locking is evident from the Table 4.4, where the results obtained with and without the coupled quadratic term are tabulated. The results prove the role of the coupled quadratic term in enabling FSDT-*Coupled* to yield single element convergence for the tip deflection and the potential developed. The results of asymmetric beam with $r = 0.5$ given in Table 4.4 are normalized with respect to the converged values obtained from ANSYS 2D simulation, $-0.2598\ mm$ for the tip deflection and $376.09\ volts$ for the potential developed at the root.

Static analysis: Actuator configuration

For actuator configuration, the beam shown in Fig. 4.24 is subjected to a voltage of $100\ volts$. The variations of tip deflection and axial deflection, with thickness ratio are plotted in Figs. 4.31 and 4.32, respectively. As seen from these graphs, the present FSDT-*Coupled* formulation consistently gives accurate predictions of results as given by ANSYS 2D simulation, over the entire range of thickness ratio. Due to

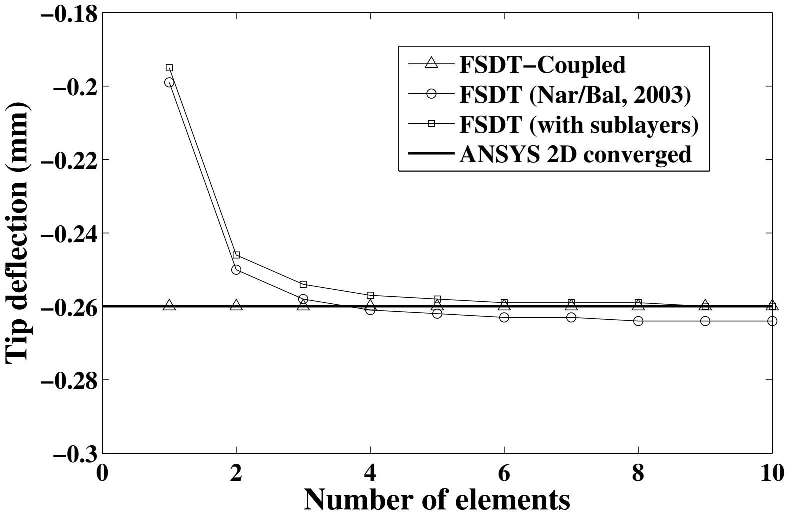

Figure 4.29: Example 2: Sensor configuration: Convergence characteristics of the FSDT-based piezoelectric beam finite elements to predict the tip deflection of the asymmetric cantilever beam ($r = 0.5$) subjected to a tip load of $-1000\ N$.

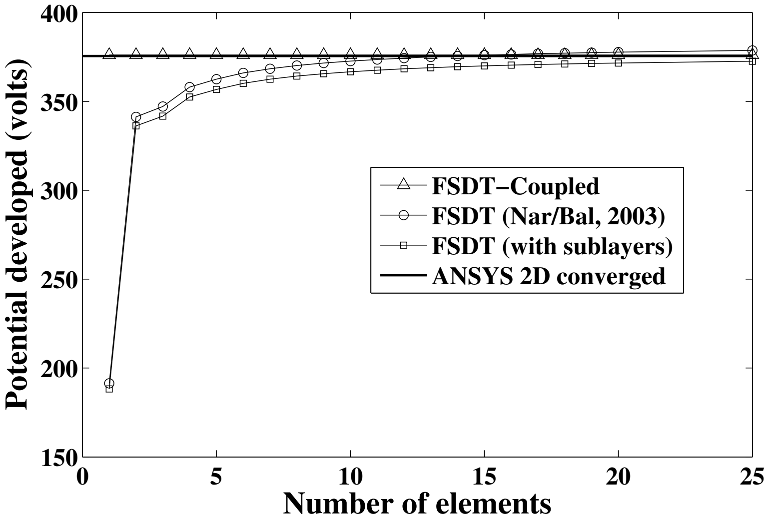

Figure 4.30: Example 2: Sensor configuration: Convergence characteristics of the FSDT-based piezoelectric beam finite elements to predict the potential developed at the root of the asymmetric cantilever beam ($r = 0.5$) subjected to a tip load of $-1000\ N$.

Table 4.4: Example 2: Role of coupled quadratic term in the field interpolation for axial displacement (Eq. (4.27)) in improving the convergence characteristics of FSDT-*Coupled* in static analysis.

Number of elements	Normalized tip deflection		Normalized potential developed at root	
	(with coupled quadratic term)	(without coupled quadratic term)	(with coupled quadratic term)	(without coupled quadratic term)
1	1.000	0.962	1.000	0.793
2	1.000	0.992	1.000	0.953
4	1.000	0.998	1.000	0.972
8	1.000	0.999	1.000	0.985
16	1.000	1.000	1.000	0.992

the piezolocking effects, the conventional FSDT formulation (Narayanan and Balamurugan, 2003) does not yield consistently accurate results. It demands sublayers in the modelling of piezolayer, to achieve the same consistent level of accuracy as of the present FSDT-*Coupled* formulation. The error due to piezolocking in the conventional FSDT formulation is quantified in Fig. 4.33 for various thickness ratios.

Modal analysis

The present FSDT-*Coupled* formulation is evaluated here for its accuracy and efficiency to predict the natural frequencies of piezoelectric smart beams. The first natural frequency of the asymmetric piezoelectric beam shown in Fig. 4.24 is evaluated for both open and closed circuit electrical boundary conditions. For open circuit, only the interface of piezoelectric layer with host layer is grounded while for closed circuit, both faces of the piezoelectric layer are grounded. The variations of first natural frequencies with thickness ratio are plotted in Figs. 4.34 and 4.35 for open and closed circuit electrical boundary conditions, respectively. The results from the present FSDT-*Coupled* formulation agree very well with the results from ANSYS 2D simulation. This validates the use of the present coupled polynomial based interpolation displacement fields, to generate consistent element mass matrix. Due to piezolocking effects which are predominant in the higher thickness ratio regimes, the results from the conventional FSDT formu-

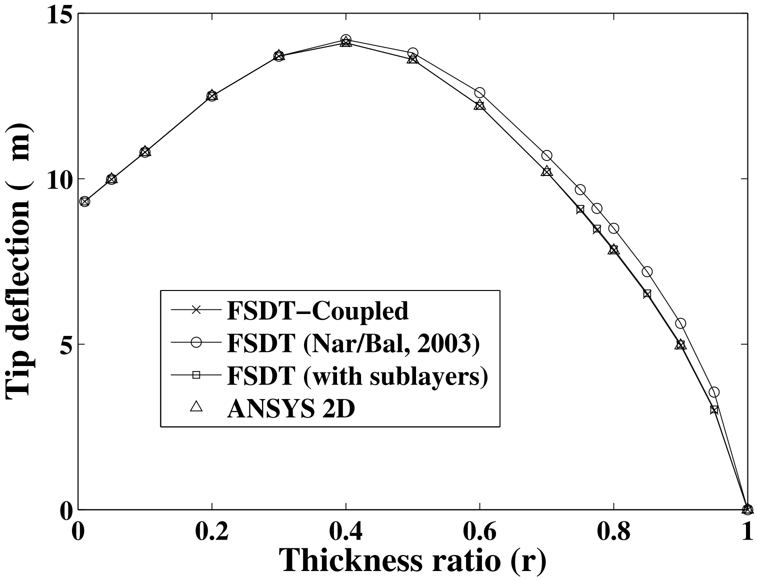

Figure 4.31: Example 2: Actuator configuration: Variation of the tip deflection with thickness ratio (r) for the asymmetric cantilever beam actuated by 100 $volts$.

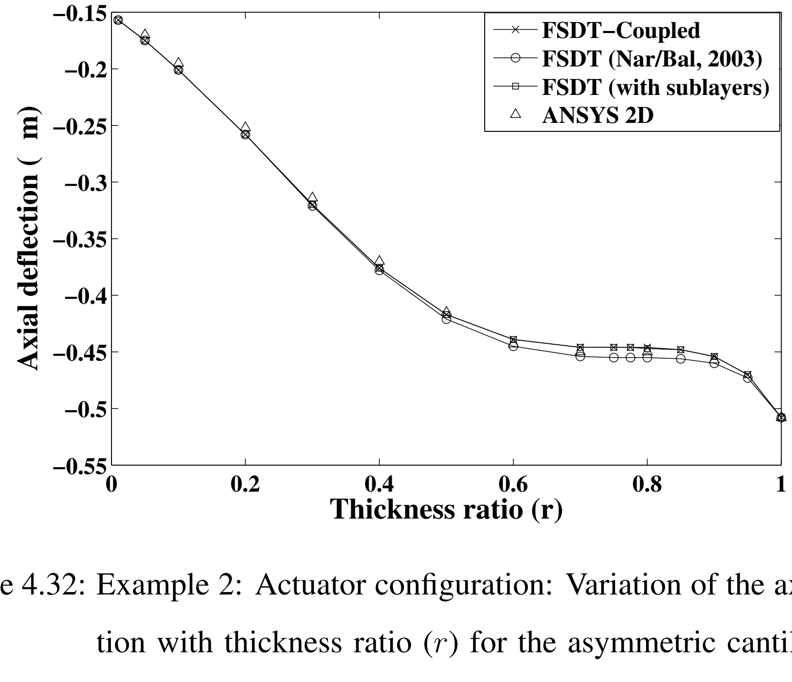

Figure 4.32: Example 2: Actuator configuration: Variation of the axial deflection with thickness ratio (r) for the asymmetric cantilever beam actuated by 100 $volts$.

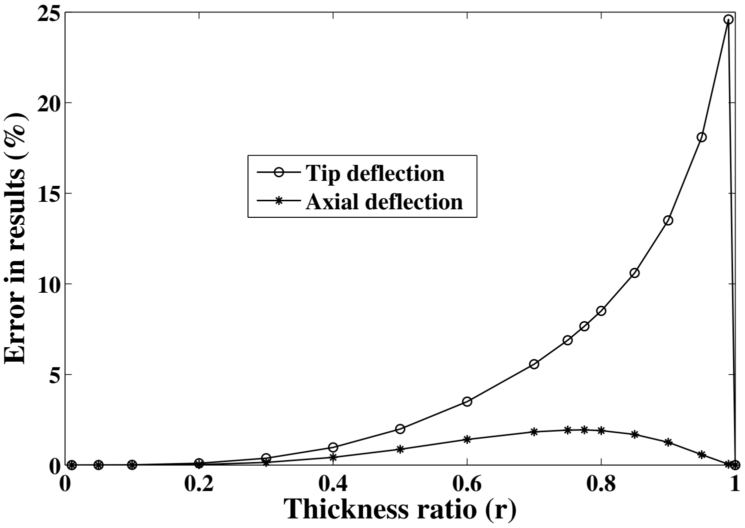

Figure 4.33: Example 2: Actuator configuration: Variation of error ($\%$) in results with thickness ratio (r), due to use of the conventional FSDT formulation.

lation of Narayanan and Balamurugan (2003) significantly deviate from the accurate results and hence requires sublayered modelling to yield acceptable level of accuracy. The error ($\%$) due to piezolocking in the conventional formulation is plotted in Fig. 4.36 for various thickness ratios.

The convergence graphs for first natural frequency in both open and closed circuit electrical boundary conditions are plotted in Figs. 4.37 and 4.38, respectively. The figures prove the efficacy of the present coupled polynomial interpolation based element stiffness matrix and the corresponding consistent element mass matrix in achieving improved convergence of natural frequencies. Both conventional FSDT and FSDT (with sublayers) models show slow and similar convergence patterns. As the conventional FSDT formulation (Narayanan and Balamurugan, 2003) suffers from piezolocking, it requires sublayers in its modelling, to converge to accurate results.

The role of the coupled quadratic term in the axial displacement given by Eq. (4.27), in eliminating material locking and improving the convergence is evident from the Table 4.5, where the results obtained with and without the coupled quadratic term are tabulated. The results prove the role of the coupled quadratic term in enabling FSDT-*Coupled* to yield quick convergence for natural frequencies. The results of asymmetric beam with $r = 0.5$ given in Table 4.5 are normalized with respect to the converged values from FSDT-*Coupled*.

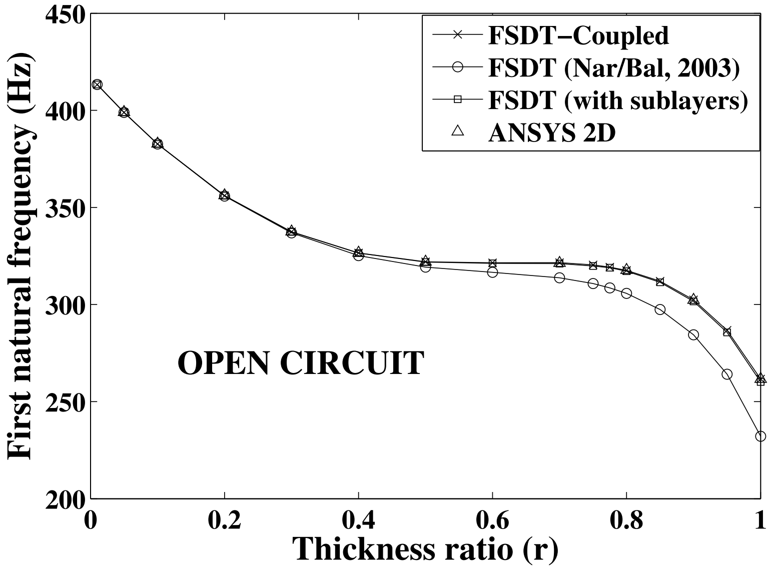

Figure 4.34: Example 2: Modal analysis: Variation of the first natural frequency with thickness ratio (r) for the asymmetric cantilever beam in open circuit electrical boundary condition.

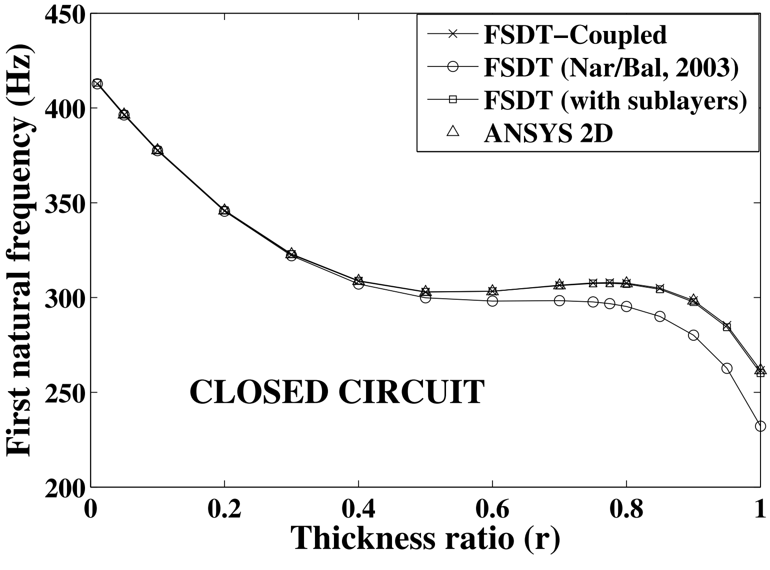

Figure 4.35: Example 2: Modal analysis: Variation of the first natural frequency with thickness ratio (r) for the asymmetric cantilever beam in closed circuit electrical boundary condition.

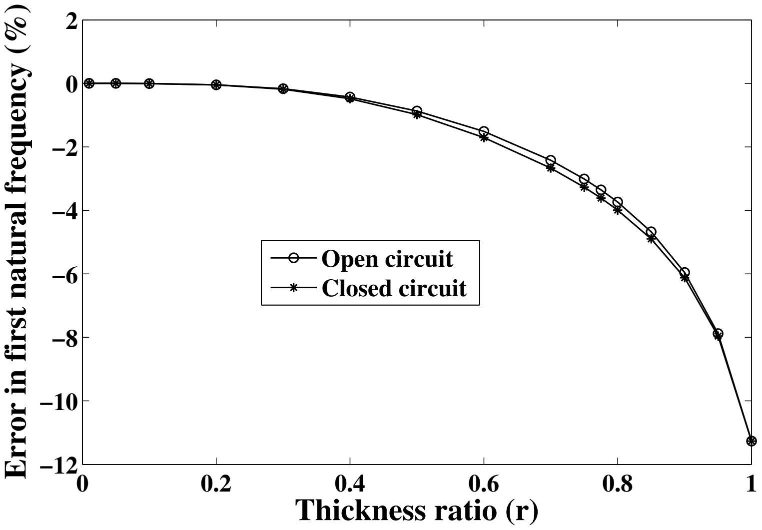

Figure 4.36: Example 2: Modal analysis: Variation of error (%) in results with thickness ratio (r), due to use of the conventional FSDT formulation.

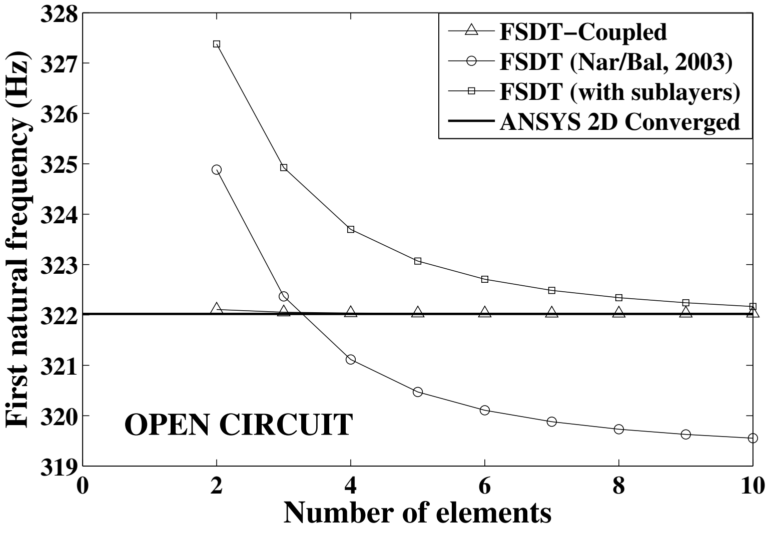

Figure 4.37: Example 2: Modal analysis: Convergence characteristics of the FSDT-based piezoelectric beam finite elements to predict the first natural frequency of the asymmetric cantilever beam ($r = 0.5$) in open circuit electrical boundary condition.

Table 4.5: Example 2: Role of coupled quadratic term in the field interpolation for axial displacement (Eq. (4.27)) in improving the convergence characteristics of FSDT-*Coupled* in modal analysis.

Number of elements	Normalized natural frequency					
	1^{st}		2^{nd}		3^{rd}	
	coupled	linear	coupled	linear	coupled	linear
			Open circuit			
1	0.995	1.027	5.170	5.066	2.198	2.366
2	1.000	1.007	0.983	1.040	1.300	1.384
4	1.000	1.002	1.000	1.012	1.002	1.029
8	1.000	1.000	1.000	1.003	1.001	1.008
16	1.000	1.000	1.000	1.001	1.000	1.002
			Closed circuit			
1	0.995	1.041	5.102	5.079	2.294	2.491
2	1.000	1.011	0.983	1.068	1.369	1.449
4	1.000	1.002	1.001	1.019	1.003	1.048
8	1.000	1.000	1.000	1.005	1.001	1.012
16	1.000	1.000	1.000	1.001	1.000	1.003

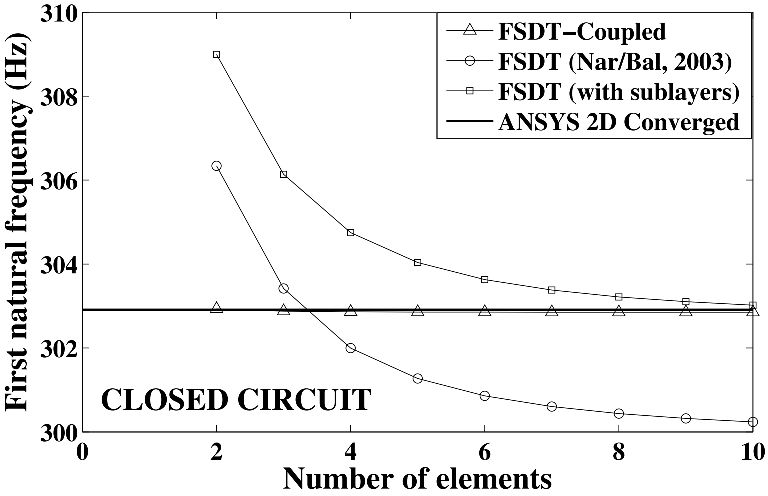

Figure 4.38: Example 2: Modal analysis: Convergence characteristics of the FSDT-based piezoelectric beam finite elements to predict the first natural frequency of the asymmetric cantilever beam ($r = 0.5$) in closed circuit electrical boundary condition.

4.8 Summary

A coupled polynomial interpolation scheme for FSDT-based piezoelectric beam finite element has been proposed here to enhance its performance by eliminating material locking, shear locking and piezolocking phenomena. A consistent interpolation for through-thickness potential derived from an electrostatic equilibrium equation has been proposed to eliminate piezolocking. A polynomial expression with a coupled quadratic term has been derived for axial displacement using the governing equilibrium equations. Similarly, a fully coupled quadratic polynomial expression has been derived for section rotation of the beam. The resulting coupled shape functions handle bending-extension coupling and bending-shear coupling in an efficient manner to eliminate material locking and shear locking. The merits of the present formulation over the conventional formulations have been proved by the comparison of the results for a set of test problems.

CHAPTER 5

COUPLED HSDT PIEZOELECTRIC BEAM FINITE ELEMENT

5.1 Introduction

In this chapter, coupled polynomial interpolations are proposed for ESL-HSDT (Equivalent Single Layer Higher-order Shear Deformation Theory) based piezoelectric beam finite element formulation. The conventional HSDT piezoelectric beam element suffers from *loss of accuracy* due to piezolocking and *slow convergence* due to material locking. The conventional HSDT piezoelectric beam finite element formulations employ linear polynomial to approximate the through-thickness potential and hence converge to inaccurate results, due to piezolocking. The traditional methods like use of higher-order approximation for through-thickness potential and the use of sublayers in the mathematical modelling of the piezoelectric layer in the conventional HSDT formulation increase number of nodal degrees of freedom and the computational cost.

In HSDT-based beam finite elements, shear locking effects are insignificant and hence negligible. The conventional HSDT piezoelectric beam finite elements which use linear interpolation of axial displacement lead to poor convergence due to material locking, when the beam cross-section is materially asymmetric. The traditional method of using higher order polynomial for interpolation of axial displacement leads to increased nodal degrees of freedom and the computational cost.

To eliminate piezolocking effects, instead of the conventional linear polynomial, a coupled *quartic* consistent through-thickness potential distribution derived using an electrostatic equilibrium equation is proposed. Coupled quadratic polynomials for axial displacement and section rotation of the beam are derived using governing equilibrium equations obtained from the variational formulation, which eliminate material locking and improves the convergence. While adopting coupled polynomials for field interpolations, the number of mechanical degrees of freedom are effectively reduced from

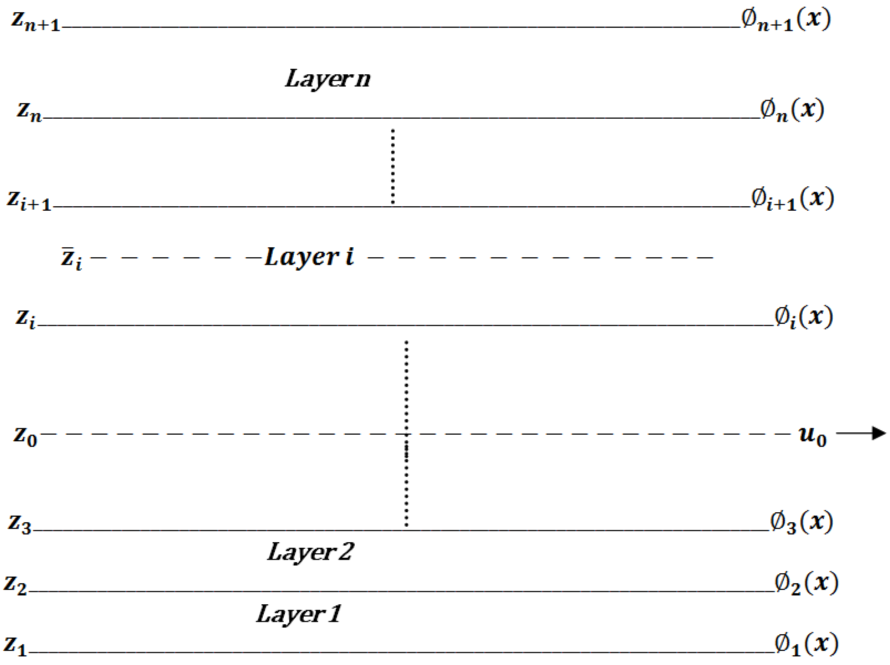

Figure 5.1: HSDT formulation: Geometry of a general multilayered extension mode piezoelectric smart beam.

four for conventional formulation to three for the present formulation, without affecting applicability of the element.

5.2 Theoretical Formulation

The formulation is based on ESL-HSDT beam theory with layerwise electric potential. Consider a general multilayered extension mode piezoelectric smart beam as shown in Fig. 5.1. The layer(s) can be host layers of conventional/composite material or bonded/embedded layer(s) of piezoelectric material. The beam layers are assumed to be made up of isotropic or specially orthotropic materials, with perfect bonding between them. The top and bottom faces of the piezoelectric layers are fully covered with electrodes. The mechanical and electrical quantities are assumed to be small enough to apply linear theories of elasticity and piezoelectricity.

5.2.1 Mechanical displacements and strains

The displacement fields in the longitudinal and transverse directions for Reddy's HSDT are given as (Heyliger and Reddy, 1988):

$$u(x,z) = u_0(x) + z\theta(x) - z^3\frac{4}{3h^2}\Big(w_0^{'}(x) + \theta(x)\Big) \tag{5.1}$$

$$w(x,z) = w_0(x) \tag{5.2}$$

where $()'$ denotes $\mathrm{d}/\mathrm{d}x$. The sub-functions $u_0(x)$ and $w_0(x)$ are the longitudinal and transverse displacements at the centroidal axis of the beam, respectively. θ is the section rotation of the beam. The dimensions L, b and h are the length, width and the total thickness of the beam, respectively.

Substituting Eqs. (5.1) and (5.2) in the usual strain-displacement relations, the following expressions for axial and shear strains are obtained:

$$\varepsilon_x(x,z) = \frac{\partial u(x,z)}{\partial x} = u_0^{'}(x) + z\theta^{'}(x) - z^3\frac{4}{3h^2}\Big(w_0^{''}(x) + \theta^{'}(x)\Big) \tag{5.3}$$

$$\gamma_{xz}(x,z) = \frac{\partial u(x,z)}{\partial z} + \frac{\partial w(x,z)}{\partial x} = \left(1 - z^2\frac{4}{h^2}\right)\Big(w_0^{'}(x) + \theta(x)\Big) \tag{5.4}$$

5.2.2 Electric potential and electric field

The layerwise through-thickness distribution of the electric potential is assumed as shown in Fig. 5.1. The two dimensional electric potential of the i^{th} piezoelectric layer $\varphi_i(x,z)$, takes the values of $\phi_{i+1}(x)$ and $\phi_i(x)$ at the top and bottom surfaces of the piezoelectric layer with thickness h_i, respectively. The electric field in the transverse (z) direction is derived from electric potential as (Benjeddou et al., 1997):

$$E_z^i(x,z) = -\frac{\partial \varphi_i(x,z)}{\partial z} \tag{5.5}$$

5.2.3 Constitutive relations

Constitutive relations for HSDT based piezoelectric beam formulation are given as (Appendix A):

$$\begin{bmatrix} \sigma_x^k \\ \tau_{xz}^k \\ D_z^i \end{bmatrix} = \begin{bmatrix} \tilde{Q}_{11}^k & 0 & -\tilde{e}_{31}^i \\ 0 & \tilde{Q}_{55}^k & 0 \\ \tilde{e}_{31}^i & 0 & \tilde{\epsilon}_3^i \end{bmatrix} \begin{bmatrix} \varepsilon_x \\ \gamma_{xz} \\ E_z^i \end{bmatrix} \tag{5.6}$$

where (i=1......number of piezoelectric layers in the beam) and (k=1.......total number of layers in the beam).

5.3 Derivation of Potential Consistent with HSDT

For the free volumic charge density assumption, the electrostatic equilibrium equation of the i^{th} piezoelectric layer reduces to (Benjeddou et al., 1997):

$$\frac{\partial D_z^i(x,z)}{\partial z} = 0 \tag{5.7}$$

as $D_x^i = D_y^i = 0$ from Eq. (5.6).

Using Eqs. (5.3), (5.5), (5.6) and (5.7), we get:

$$\frac{\partial^2 \varphi_i}{\partial z^2}(x,z) = \frac{\tilde{e}_{31}^i}{\tilde{\epsilon}_3^i}\theta^{'}(x) - \frac{\tilde{e}_{31}^i}{\tilde{\epsilon}_3^i}3\alpha z^2\left(\theta^{'}(x) + w_0^{''}(x)\right) \tag{5.8}$$

where, $\alpha = 4/(3h^2)$.

On solving Eq.(5.8), we get:

$$\varphi_i(x,z) = \frac{\tilde{e}_{31}^i}{\tilde{\epsilon}_3^i}\frac{z^2}{2}\theta^{'}(x) - \frac{\tilde{e}_{31}^i}{\tilde{\epsilon}_3^i}\alpha\frac{z^4}{4}\left(\theta^{'}(x) + w_0^{''}(x)\right) + C_1^i(x)z + C_2^i(x) \tag{5.9}$$

where C_1^i and C_2^i are the constants to be obtained from boundary condition for φ in z-direction. For i^{th} layer boundary conditions are $\varphi_{(z=z_{i+1})}(x,z) = \phi_{i+1}(x)$ and $\varphi_{(z=z_i)}(x,z) = \phi_i(x)$. After solving Eq. (5.9) and simplifying, we obtain the expression for electric potential as:

$$\varphi_i(x,z) = \bar{\varphi}_i(x) + \left(\frac{(z-\bar{z}_i)}{h_i}\right)\tilde{\varphi}_i(x) + K_1^i\theta^{'}(x) - K_2^i\left(\theta^{'}(x) + w_0^{''}(x)\right) \tag{5.10}$$

where

$$\begin{aligned}
K_1^i &= \frac{\tilde{e}_{31}^i}{\tilde{\epsilon}_3^i}\frac{h_i^2}{8}\left(\frac{(z-\bar{z}_i)^2}{(h_i/2)^2} - 1\right); \\
K_2^i &= \frac{\tilde{e}_{31}^i}{\tilde{\epsilon}_3^i}\alpha\frac{h_i^4}{64}\left\{\left(\frac{z}{h_i/2}\right)^4 - \left(\frac{\bar{z}_i}{h_i/2}\right)^4 - 4\left[\left(\frac{\bar{z}_i}{h_i/2}\right)^3 + \left(\frac{\bar{z}_i}{h_i/2}\right)\right]\frac{(z-\bar{z}_i)}{(h_i/2)}\right. \\
&\qquad \left. -6\left(\frac{\bar{z}_i}{h_i/2}\right)^2 - 1\right\}; \\
\bar{\varphi}_i &= (\phi_{i+1} + \phi_i)/2; \qquad \tilde{\varphi}_i = (\phi_{i+1} - \phi_i); \qquad \bar{z}_i = (z_{i+1} + z_i)/2
\end{aligned}$$

From Eq. (5.10), it is clear that the consistent electric potential is of *fourth*-order for HSDT. The first two terms of expression (5.10) describe the conventional linear part in which $\bar{\varphi}_i$ and $\tilde{\varphi}_i$ are the mean and difference, respectively, of the top and bottom surface potentials. The last two terms constitute the induced part of the potential which plays an important role as it changes the stiffness of the piezoelectric layer. These quadratic and quartic terms represent the contribution to induced potential by bending strain and shear strain, respectively. The coefficients of induced potential terms depend on geometric and material properties of the piezoelectric layer.

The electric field can be obtained from Eq. (5.10) as:

$$\begin{aligned}
E_z^i(x,z) = -\frac{\partial\varphi_i(x,z)}{\partial z} &= -\frac{\tilde{\varphi}_i(x)}{h_i} - \frac{\tilde{e}_{31}^i}{\tilde{\epsilon}_3^i}\left[\left(z - \alpha z^3\right) - \bar{z}_i\left(1 - \alpha K_3^i\right)\right]\theta^{'}(x) \\
&\quad - \frac{\tilde{e}_{31}^i}{\tilde{\epsilon}_3^i}\left(-\alpha z^3 + \alpha\bar{z}_i K_3^i\right)w_0^{''}(x)
\end{aligned} \tag{5.11}$$

where

$$K_3^i = \frac{h_i^2}{4}\left[\left(\frac{\bar{z}_i}{h_i/2}\right)^2 + 1\right]$$

5.4 Variational Formulation

Hamilton's principle is used to formulate the smart beam. It is expressed as (Chee et al., 1999):

$$\delta \int_{t_1}^{t_2} (K - H + W)\, dt = \int_{t_1}^{t_2} (\delta K - \delta H + \delta W)\, dt = 0 \tag{5.12}$$

where K is the kinetic energy, H is the electric enthalpy density function for the piezoelectric material and the mechanical strain energy for the linear elastic material and W is the work done by the external forces.

5.4.1 Variation of electromechanical/strain energy

For the j^{th} conventional material layer, the variation of mechanical strain energy δH is given by:

$$\delta H_j = \int_V \left(\sigma_x^j \delta\varepsilon_x^j + \tau_{xz}^j \delta\gamma_{xz}^j \right) dV \tag{5.13}$$

The variation of electromechanical energy for the i^{th} piezoelectric layer is given by:

$$\delta H_i = \int_V \left(\sigma_x^i \delta\varepsilon_x^i + \tau_{xz}^i \delta\gamma_{xz}^i - D_z^i \delta E_z^i \right) dV \tag{5.14}$$

Substituting values of axial strain (ε_x), shear strain (γ_{xz}), transverse electric field (E_z) from Eqs. (5.3), (5.4), (5.11) and using them along with constitutive relations from (5.6) in Eqs. (5.13) and (5.14), variation on total electromechanical/strain energy of beam can be written as:

$$\int_{t_1}^{t_2} \delta H dt = \int_{t_1}^{t_2} \int_x \left\{ \delta u_0^{'} \left(\begin{array}{c} (\tilde{Q}_{11}^k I_0^k) u_0^{'} + \\ \left[\tilde{Q}_{11}^k (I_1^k - \alpha I_3^k) + \frac{(\tilde{e}_{31}^i)^2}{\tilde{\epsilon}_3^i} \left(I_1^i - \alpha I_3^i - I_0^i \bar{z}_i \left(1 - \alpha K_3^i \right) \right) \right] \theta^{'} \\ - \left[\tilde{Q}_{11}^k \alpha I_3^k + \frac{(\tilde{e}_{31}^i)^2}{\tilde{\epsilon}_3^i} \alpha \left(I_3^i - I_0^i \bar{z}_i K_3^i \right) \right] w_0^{''} \\ + \left(\tilde{e}_{31}^i I_0^i / h_i \right) \tilde{\varphi}_i \end{array} \right) + \right.$$

$$
\begin{aligned}
&\delta\theta^{'}\left(\begin{array}{c}
\left[\tilde{Q}_{11}^{k}(I_1^k-\alpha I_3^k)+\frac{(\tilde{e}_{31}^{i})^2}{\tilde{\epsilon}_3^i}\left(I_1^i-\alpha I_3^i-I_0^i\bar{z}_i\left(1-\alpha K_3^i\right)\right)\right]u_0^{'}\\
+\left(\begin{array}{c}\tilde{Q}_{11}^{k}(I_2^k-2\alpha I_4^k+\alpha^2 I_6^k)+\\ \frac{(\tilde{e}_{31}^{i})^2}{\tilde{\epsilon}_3^i}\left[I_2^i-2\alpha I_4^i+\alpha^2 I_6^i-I_0^i\left(\bar{z}_i-\alpha\bar{z}_iK_3^i\right)^2\right]\end{array}\right)\theta^{'}\\
-\left(\begin{array}{c}\tilde{Q}_{11}^{k}(\alpha I_4^k-\alpha^2 I_6^k)\\ +\frac{(\tilde{e}_{31}^{i})^2}{\tilde{\epsilon}_3^i}\left[\alpha I_4^i-\alpha^2 I_6^i-I_0^i\alpha\bar{z}_i^2K_3^i\left(1-\alpha K_3^i\right)\right]\end{array}\right)w_0^{''}\\
+\left(\tilde{e}_{31}^iI_0^i\left(\bar{z}_i-\alpha\bar{z}_iK_3^i\right)/h_i\right)\tilde{\varphi}_i
\end{array}\right)+\\
&\delta w_0^{''}\left(\begin{array}{c}
-\left[\tilde{Q}_{11}^{k}\alpha I_3^k+\frac{(\tilde{e}_{31}^{i})^2}{\tilde{\epsilon}_3^i}\alpha\left(I_3^i-I_0^i\bar{z}_iK_3^i\right)\right]u_0^{'}-\\
\left(\begin{array}{c}\tilde{Q}_{11}^{k}(\alpha I_4^k-\alpha^2 I_6^k)\\ +\frac{(\tilde{e}_{31}^{i})^2}{\tilde{\epsilon}_3^i}\left[\alpha I_4^i-\alpha^2 I_6^i-I_0^i\alpha\bar{z}_i^2K_3^i\left(1-\alpha K_3^i\right)\right]\end{array}\right)\theta^{'}\\
+\left[\tilde{Q}_{11}^{k}\alpha^2 I_6^k+\frac{(\tilde{e}_{31}^{i})^2}{\tilde{\epsilon}_3^i}\alpha^2\left(I_6^i-I_0^i\bar{z}_i^2K_3^{i2}\right)\right]w_0^{''}\\
-\left(\tilde{e}_{31}^i\alpha I_0^i\bar{z}_iK_3^i/h_i\right)\tilde{\varphi}_i
\end{array}\right)+\\
&\delta\theta\left(\tilde{Q}_{55}^{k}(I_0^k-2\beta I_2^k+\beta^2 I_4^k)\right)(\theta+w_0^{'})+\\
&\delta w_0^{'}\left(\tilde{Q}_{55}^{k}(I_0^k-2\beta I_2^k+\beta^2 I_4^k)\right)(\theta+w_0^{'})+\\
&\delta\tilde{\varphi}_i\left(\begin{array}{c}
\left(\tilde{e}_{31}^iI_0^i/h_i\right)u_0^{'}+\left(\tilde{e}_{31}^iI_0^i\left(\bar{z}_i-\alpha\bar{z}_iK_3^i\right)/h_i\right)\theta^{'}\\
-\left(\tilde{e}_{31}^i\alpha I_0^i\bar{z}_iK_3^i/h_i\right)w_0^{''}-(\tilde{\epsilon}_3^iI_0^i/h_i^2)\tilde{\varphi}_i
\end{array}\right)\left.\vphantom{\begin{array}{c}a\\b\end{array}}\right\}dxdt
\end{aligned}
\tag{5.15}
$$

where i=(1.....number of piezolayers), k=(1......total number of layers); $\beta = 4/h^2$ and $I_q^k = b(z_{k+1}^{q+1} - z_k^{q+1})/(q+1)$. From Eq. (5.15), it is clear that induced potential changes the stiffness of the structure.

5.4.2 Variation of kinetic energy

The electrical variables do not enter into the expression for kinetic energy and it is given as (Chee et al., 1999):

$$
K = \frac{1}{2}b\int_x\int_{z_k}^{z_{k+1}} \rho_k\left(\dot{u}^2+\dot{w}^2\right)dzdx \tag{5.16}
$$

where ρ_k is mass density of k^{th} layer in kgm^{-3} and (k=1....total number of layers in beam). Substituting values of u and w from Eqs. (5.1) and (5.2) and applying variation to get:

$$
\begin{aligned}
-\int_{t1}^{t2}\delta K dt = &\rho_k \int_{t1}^{t2}\int_x \Big\{ \delta u_0 \left(I_0^k \ddot{u}_0 + (I_1^k - \alpha I_3^k)\ddot{\theta} - \alpha I_3^k \ddot{w}_0^{'} \right) + \\
&\delta\theta \begin{pmatrix} (I_1^k - \alpha I_3^k)\ddot{u}_0 + (I_2^k - 2\alpha I_4^k + \alpha^2 I_6^k)\ddot{\theta} \\ -(\alpha I_4^k - \alpha^2 I_6^k)\ddot{w}_0^{'} \end{pmatrix} + \\
&\delta w_0^{'} \left(-\alpha I_3^k \ddot{u}_0 - (\alpha I_4^k - \alpha^2 I_6^k)\ddot{\theta} + \alpha^2 I_6^k \ddot{w}_0^{'} \right) + \\
&\delta w_0 \left(I_0^k \ddot{w}_0 \right) \Big\} dxdt
\end{aligned} \tag{5.17}
$$

where, $\dot{()}$ denotes $\frac{\partial}{\partial t}$.

5.4.3 Variation of the work of external forces

The total virtual work on the structure can be defined as the product of the virtual displacements with forces for the mechanical work and the product of the virtual electric potential with the charges for the electrical work. The variation of the total work done by the external mechanical and electrical loading is given as (Chee et al., 1999):

$$
\begin{aligned}
\int_{t_1}^{t_2}\delta W dt = \int_{t_1}^{t_2} \Big\{ &\int_V (\delta u f_u^v + \delta w f_w^v) dV + \int_S (\delta u f_u^s + \delta w f_w^s) dS \\
&+ \sum (\delta u f_u^c + \delta w f_w^c) - \int_{S\varphi} \delta\varphi q_0 dS_\varphi \Big\} dt
\end{aligned} \tag{5.18}
$$

in which f^v,f^s,f^c are volume, surface, point forces, respectively; q_0 and S_φ are the surface charges and area on which charge is applied.

5.5 Derivation of Coupled Field Relations

For static condition without any external loading, the variational principle given in Eq. (5.12) reduces to:

$$\delta H = 0 \tag{5.19}$$

Applying variation to the basic variables in Eq. (5.15) and using them in Eq. (5.19), we get the static equilibrium equations as:

$$\delta u_0 : \quad \begin{pmatrix} (\tilde{Q}_{11}^k I_0^k) u_0^{''} + \\ \left[\tilde{Q}_{11}^k (I_1^k - \alpha I_3^k) + \frac{(\tilde{e}_{31}^i)^2}{\tilde{\epsilon}_3^i} \left(I_1^i - \alpha I_3^i - I_0^i \bar{z}_i \left(1 - \alpha K_3^i\right)\right)\right] \theta^{''} \\ - \left[\tilde{Q}_{11}^k \alpha I_3^k + \frac{(\tilde{e}_{31}^i)^2}{\tilde{\epsilon}_3^i} \alpha \left(I_3^i - I_0^i \bar{z}_i K_3^i\right)\right] w_0^{'''} \\ + \left(\tilde{e}_{31}^i I_0^i / h_i\right) \tilde{\varphi}_i^{'} \end{pmatrix} = 0 \tag{5.20}$$

$$\delta \theta : \quad \begin{pmatrix} - \left[\tilde{Q}_{11}^k (I_1^k - \alpha I_3^k) + \frac{(\tilde{e}_{31}^i)^2}{\tilde{\epsilon}_3^i} \left(I_1^i - \alpha I_3^i - I_0^i \bar{z}_i \left(1 - \alpha K_3^i\right)\right)\right] u_0^{''} \\ - \begin{pmatrix} \tilde{Q}_{11}^k (I_2^k - 2\alpha I_4^k + \alpha^2 I_6^k) + \\ \frac{(\tilde{e}_{31}^i)^2}{\tilde{\epsilon}_3^i} \left[I_2^i - 2\alpha I_4^i + \alpha^2 I_6^i - I_0^i \left(\bar{z}_i - \alpha \bar{z}_i K_3^i\right)^2\right] \end{pmatrix} \theta^{''} \\ + \left[\tilde{Q}_{11}^k (\alpha I_4^k - \alpha^2 I_6^k) + \frac{(\tilde{e}_{31}^i)^2}{\tilde{\epsilon}_3^i} \left(\alpha I_4^i - \alpha^2 I_6^i - I_0^i \alpha \bar{z}_i^2 K_3^i \left(1 - \alpha K_3^i\right)\right)\right] w_0^{'''} \\ + \left(\tilde{Q}_{55}^k (I_0^k - 2\beta I_2^k + \beta^2 I_4^k)\right) (\theta + w_0^{'}) \\ - \left(\tilde{e}_{31}^i I_0^i \left(\bar{z}_i - \alpha \bar{z}_i K_3^i\right) / h_i\right) \tilde{\varphi}_i^{'} \end{pmatrix} = 0 \tag{5.21}$$

$$\delta w_0 : \quad \begin{pmatrix} - \left[\tilde{Q}_{11}^k \alpha I_3^k + \frac{(\tilde{e}_{31}^i)^2}{\tilde{\epsilon}_3^i} \alpha \left(I_3^i - I_0^i \bar{z}_i K_3^i\right)\right] u_0^{'''} - \\ \left[\tilde{Q}_{11}^k (\alpha I_4^k - \alpha^2 I_6^k) + \frac{(\tilde{e}_{31}^i)^2}{\tilde{\epsilon}_3^i} \left(\alpha I_4^i - \alpha^2 I_6^i - I_0^i \alpha \bar{z}_i^2 K_3^i \left(1 - \alpha K_3^i\right)\right)\right] \theta^{'''} \\ + \left[\tilde{Q}_{11}^k \alpha^2 I_6^k + \frac{(\tilde{e}_{31}^i)^2}{\tilde{\epsilon}_3^i} \alpha^2 \left(I_6^i - I_0^i \bar{z}_i^2 K_3^{i2}\right)\right] w_0^{''''} \\ - \left(\tilde{Q}_{55}^k (I_0^k - 2\beta I_2^k + \beta^2 I_4^k)\right) (\theta^{'} + w_0^{''}) \\ - \left(\tilde{e}_{31}^i \alpha I_0^i \bar{z}_i K_3^i / h_i\right) \tilde{\varphi}_i^{''} \end{pmatrix} = 0 \tag{5.22}$$

These equations can be written in simplified form as:

$$\delta u_0 : \qquad A_1^u u_0^{''} + A_2^u \theta^{''} + A_3^u w_0^{'''} + A_4^{ui} \tilde{\varphi}_i^{'} = 0 \tag{5.23}$$

$$\delta \theta : \qquad A_1^\theta u_0^{''} + A_2^\theta \theta^{''} + A_3^\theta w_0^{'''} + A_4^\theta (\theta + w_0^{'}) + A_5^{\theta i} \tilde{\varphi}_i^{'} = 0 \tag{5.24}$$

$$\delta w_0 : \qquad A_1^w u_0^{'''} + A_2^w \theta^{'''} + A_3^w w_0^{''''} + A_4^w (\theta^{'} + w_0^{''}) + A_5^{wi} \tilde{\varphi}_i^{''} = 0 \tag{5.25}$$

From equation (5.25), neglecting higher order terms, we can write:

$$\theta^{''} = -w_0^{'''} \tag{5.26}$$

Using Eqs. (5.23) and (5.26), the relation between axial displacement (u_0), transverse displacement (w_0) and electric potential (φ_i) is derived as:

$$u_0^{''} = \lambda_1 w_0^{'''} + \lambda_2^i \tilde{\varphi}_i^{'} \tag{5.27}$$

where $\lambda_1 = (A_2^u - A_3^u)/A_1^u$ and $\lambda_2^i = -A_4^{ui}/A_1^u$.

Using Eqs. (5.23), (5.24) and (5.26), we can write the relation between section rotation (θ), transverse displacement (w_0) and electric potential (φ_i) as:

$$\theta = -w_0^{'} + \lambda_3 w_0^{'''} + \lambda_4^i \tilde{\varphi}_i^{'} \tag{5.28}$$

where

$$\begin{aligned} \lambda_3 &= \frac{A_3^u - A_2^u}{A_1^u}\frac{A_1^\theta}{A_4^\theta} + \frac{A_2^\theta - A_3^\theta}{A_4^\theta} \\ \lambda_4^i &= \frac{A_4^{ui}}{A_1^u}\frac{A_1^\theta}{A_4^\theta} - \frac{A_5^{\theta i}}{A_4^\theta} \end{aligned}$$

From Eqs. (5.27) and (5.28), it is clear that the constants λ_m (m=1,2,3,4) depends on geometric and material properties of the beam and these constants relates all the field variables by properly accommodating bending-extension, bending-shear and induced potential couplings. These expressions are used in next section to derive coupled polynomial expressions for the field variables.

5.6 Finite Element Formulation

Using the variational formulation described above, a finite element model is developed here. The model consists of three mechanical variables (u_0, w_0 and θ) and layerwise electrical variables ($\tilde{\varphi}_i$) where (i=1.....number of piezoelectric layers in the beam).

In terms of natural coordinate (ξ), a cubic polynomial for transverse displacement

(w_0) and linear polynomials for electric potentials ($\tilde{\varphi}_i$) are assumed as given in Eqs. (5.29a) and (5.29b), respectively. The transformation between coordinate ξ and global coordinate (x) along the length of the beam is given as $\xi = [2(x - x_1)/(x_2 - x_1)] - 1$ and $x_2 - x_1 = l$, length of the beam element.

$$w_0 = b_0 + b_1\xi + b_2\xi^2 + b_3\xi^3 \tag{5.29a}$$

$$\tilde{\varphi}_i = c_0^i + c_1^i\xi \tag{5.29b}$$

Using these polynomials for w_0 and $\tilde{\varphi}_i$ in Eq. (5.27), and integrating with respect to ξ, we get the coupled polynomial for midplane axial displacement (u_0) as:

$$u_0 = [(6\lambda_1/l)b_3 + (\lambda_2^i l/4)c_1^i]\xi^2 + a_1\xi + a_0 \tag{5.30}$$

Using Eqs. (5.29a) and (5.29b) in Eq. (5.28), the coupled polynomial for section rotation (θ) is obtained as:

$$\theta = -b_1(2/l) - b_2(2\xi(2/l)) - b_3\left(3\xi^2(2/l) - 6\lambda_3(2/l)^3\right) + c_1^i(\lambda_4^i(2/l)) \tag{5.31}$$

It is noteworthy that the coefficients λ_i (i=1,2,3,4) present in Eqs. (5.30) and (5.31) takes care of bending-shear, bending-extension and induced potential couplings in a variationally consistent manner.

Using Eq. (5.4), the shear strain field (at midplane) is derived as:

$$\gamma_{xz}(x,0) = \theta + w_0^{'} = b_3(6\lambda_3(2/l)^3) + c_1^i(\lambda_4^i(2/l)) \tag{5.32}$$

The above variationally consistent shear strain field is constant over the element. Also, it does not lead to any spurious constraints in the thin limits, as the coefficients λ_3 and λ_4 tend to vanish as beam thickness approaches zero. Hence no shear locking shall be experienced.

Using Eqs. (5.29a), (5.29b), (5.30) and (5.31) the coupled shape functions in Eq.

(5.33) are derived by usual method.

$$\begin{Bmatrix} u_0 \\ \\ w_0 \\ \\ \theta \\ \\ \tilde{\varphi}_i \end{Bmatrix} = \begin{bmatrix} N_1^u & N_2^u & N_3^u & N_4^{ui} & N_5^u & N_6^u & N_7^u & N_8^{ui} \\ \\ 0 & N_1^w & N_2^w & N_3^{wi} & 0 & N_4^w & N_5^w & N_6^{wi} \\ \\ 0 & N_1^\theta & N_2^\theta & N_3^{\theta i} & 0 & N_4^\theta & N_5^\theta & N_6^{\theta i} \\ \\ 0 & 0 & 0 & N_1^{\varphi i} & 0 & 0 & 0 & N_2^{\varphi i} \end{bmatrix} \begin{Bmatrix} u_0^1 \\ w_0^1 \\ \theta^1 \\ \tilde{\varphi}_i^1 \\ u_0^2 \\ w_0^2 \\ \theta^2 \\ \tilde{\varphi}_i^2 \end{Bmatrix} \tag{5.33}$$

The expressions for these shape functions in natural coordinate system are:

$$N_1^u = \frac{(1-\xi)}{2}; \qquad N_2^u = \frac{3\lambda_1 l}{24\lambda_3 - 2l^2}(1-\xi^2);$$

$$N_3^u = \frac{3\lambda_1 l^2}{48\lambda_3 - 4l^2}(\xi^2 - 1); \qquad N_4^{ui} = \frac{\lambda_2^i l^3 + 12l(\lambda_1 \lambda_4^i - \lambda_2^i \lambda_3)}{96\lambda_3 - 8l^2}(\xi^2 - 1);$$

$$N_5^u = \frac{(1+\xi)}{2} \qquad N_6^u = \frac{3\lambda_1 l}{24\lambda_3 - 2l^2}(\xi^2 - 1);$$

$$N_7^u = \frac{3\lambda_1 l^2}{48\lambda_3 - 4l^2}(\xi^2 - 1); \qquad N_8^{ui} = \frac{\lambda_2^i l^3 + 12l(\lambda_1 \lambda_4^i - \lambda_2^i \lambda_3)}{96\lambda_3 - 8l^2}(1-\xi^2);$$

$$N_1^w = \frac{1}{2} - \frac{l^2\xi^3 + \xi(24\lambda_3 - 3l^2)}{48\lambda_3 - 4l^2}; \qquad N_2^w = (\xi^2 - 1)\left[\frac{l}{8} + \frac{l^3\xi}{96\lambda_3 - 8l^2}\right];$$

$$N_3^{wi} = (\xi^2 - 1)\frac{\lambda_4^i l^2 \xi}{48\lambda_3 - 4l^2}; \qquad N_4^w = \frac{1}{2} + \frac{l^2\xi^3 + \xi(24\lambda_3 - 3l^2)}{48\lambda_3 - 4l^2};$$

$$N_5^w = (1-\xi^2)\left[\frac{l}{8} - \frac{l^3\xi}{96\lambda_3 - 8l^2}\right]; \qquad N_6^{wi} = (1-\xi^2)\frac{\lambda_4^i l^2 \xi}{48\lambda_3 - 4l^2}$$

$$N_1^\theta = \frac{3l}{24\lambda_3 - 2l^2}(\xi^2 - 1); \qquad N_2^\theta = \frac{24\lambda_3 + l^2(1 - 3\xi^2)}{48\lambda_3 - 4l^2} - \frac{\xi}{2};$$

$$N_3^{\theta i} = \frac{3\lambda_4^i l}{24\lambda_3 - 2l^2}(1-\xi^2); \qquad N_4^\theta = \frac{3l}{24\lambda_3 - 2l^2}(1-\xi^2);$$

$$N_5^\theta = \frac{24\lambda_3 + l^2(1 - 3\xi^2)}{48\lambda_3 - 4l^2} + \frac{\xi}{2}; \qquad N_6^{\theta i} = \frac{3\lambda_4^i l}{24\lambda_3 - 2l^2}(\xi^2 - 1);$$

$$N_1^{\varphi i} = \frac{(1-\xi)}{2}; \qquad N_2^{\varphi i} = \frac{(1+\xi)}{2};$$

As noted from Eq. (5.33), the present formulation uses only three mechanical degrees of freedom i.e. $\{u_0, w_0, \theta\}$, while the conventional HSDT based formulations uses four eg. Peng et al. (1998) and Elshafei and Alraiess (2013) uses $\{u_0, w_0, w_0^{'}, \theta\}$ and Chee et al. (1999) uses $\{u_0, w_0, w_0^{'}, \gamma_0\}$. The present formulation saves one nodal degree of freedom without affecting the applicability of the element because all the three engineering degrees of freedom corresponding to axial force, shear force and bending moment are retained.

Now, the variation on the basic mechanical and electrical variables can be transferred to nodal degrees of freedom. Substituting Eq. (5.33) in Eqs. (5.15), (5.17), (5.18) and using equation (5.12), we get the descretized form of finite element equations as:

$$\begin{bmatrix} \begin{bmatrix} M \end{bmatrix} & 0 \\ 0 & 0 \end{bmatrix} \begin{bmatrix} \begin{Bmatrix} \ddot{U} \end{Bmatrix} \\ \begin{Bmatrix} \ddot{\Phi} \end{Bmatrix} \end{bmatrix} + \begin{bmatrix} \begin{bmatrix} K_{uu} \end{bmatrix} & \begin{bmatrix} K_{u\varphi} \end{bmatrix} \\ \begin{bmatrix} K_{\varphi u} \end{bmatrix} & \begin{bmatrix} K_{\varphi\varphi} \end{bmatrix} \end{bmatrix} \begin{bmatrix} \begin{Bmatrix} U \end{Bmatrix} \\ \begin{Bmatrix} \Phi \end{Bmatrix} \end{bmatrix} = \begin{bmatrix} \begin{Bmatrix} F \end{Bmatrix} \\ \begin{Bmatrix} Q \end{Bmatrix} \end{bmatrix} \tag{5.34}$$

where M is the mass matrix. $K_{uu}, K_{u\varphi}, K_{\varphi u}, K_{\varphi\varphi}$ are the global stiffness sub-matrices. U, Φ are the global mechanical and electrical nodal degrees of freedom vectors, respectively. F and Q are global mechanical and electrical nodal force vectors, respectively. These matrix equations now can be solved according to the electrical conditions (closed/open circuit) and mode of operation (actuation/sensing) for static/dynamic analyses.

5.7 Numerical Examples and Discussions

The proposed formulation is validated here for accuracy and efficiency in static (actuation and sensing) and modal analyses (open and closed circuit) of piezoelectric smart beams. The software implementation has been carried out in MATLAB environment. The performance of the present formulation is compared against the conventional two-noded HSDT formulations available in the literature and 2D finite element simulation using ANSYS software. The finite element formulations used for the comparative study are designated here as:

HSDT-*Coupled* : The present formulation which uses coupled polynomials (cubic for w_0 given by Eq. (5.29a), coupled quadratic for u_0 given by Eq. (5.30), coupled quadratic for θ given by Eq. (5.31) and linear for $\tilde{\varphi}_i$ given by Eq. (5.29b)) for interpolation of field variables and layerwise consistent through-thickness potential (coupled quartic approximation in z direction given by Eq. (5.10)). This formulation is expected to be free from piezolocking and material locking. The element has three mechanical nodal degrees of freedom: u_0, w_0, θ and i electrical nodal degrees of freedom: $\tilde{\varphi}_i$ (i=1....number of piezoelectric layers). It does not employ any sublayers within the piezoelectric layer, for modelling.

HSDT-1 : The conventional HSDT formulation of Elshafei and Alraiess (2013) which uses independent polynomials for field interpolation (linear for u_0, θ and $\tilde{\varphi}_i$, Hermite cubic for w_0) and assumed linear through-thickness potential. This element suffers from piezolocking and material locking. The element has four mechanical nodal degrees of freedom: u_0, w_0, $w_0^{'}$, θ and i electrical nodal degrees of freedom: $\tilde{\varphi}_i$ (i=1....number of piezoelectric layers).

HSDT-2 : The modified form of conventional HSDT formulation (Chee et al., 1999) which uses shear angle (γ_0) as a nodal variable instead of section rotation (θ). This formulation uses independent polynomials for field interpolation (linear for u_0,γ_0 and $\tilde{\varphi}_i$, Hermite cubic for w_0) and assumed linear through-thickness potential. This element suffers from piezolocking and material locking. The element has four mechanical nodal degrees of freedom: u_0, w_0, $w_0^{'}$, γ_0 and i electrical nodal degrees of freedom: $\tilde{\varphi}_i$ (i=1....number of piezoelectric layers).

Though both HSDT-1 and HSDT-2 converges to same results, HSDT-2 has better convergence characteristic than HSDT-1.

HSDT-1 (with sublayers) and HSDT-2 (with sublayers) : The piezolocking in the above HSDT-1 and HSDT-2 models may be eliminated by using a sufficient number of sublayers for modelling each piezoelectric layer. The through-thickness distribution of potential in each piezolayer is represented by sublayer-wise linear approximations. In these sublayered versions of conventional HSDT beam elements, we have used *five sublayers* per physical piezoelectric layer, which are found adequate to yield reasonably accurate results. However, each sublayer would introduce an additional nodal electric potential degree of freedom and hence these elements are computationally expensive.

ANSYS 2D : For a comparative evaluation of the above HSDT formulations,

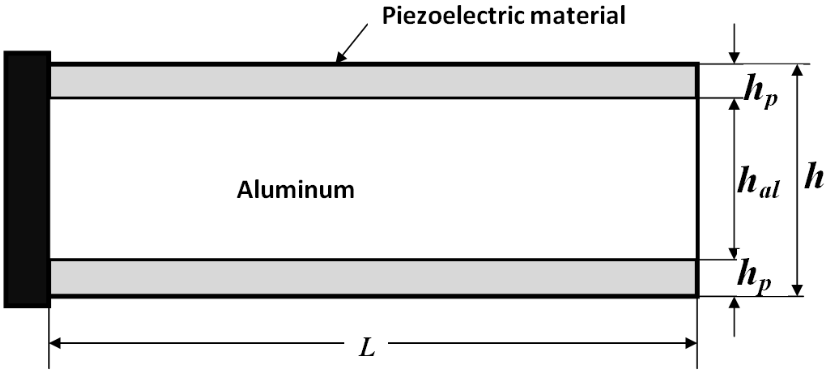

Figure 5.2: Example 1: Geometry of the three-layer cantilever beam with symmetrically bonded oppositely poled piezoelectric layers in extension mode.

benchmark solutions have been obtained from a refined 2-dimensional analysis using ANSYS finite element software (ANSYS-Release12, 2009), for which PLANE 183 elements are used to mesh conventional material layers, while PLANE 223 elements are used to mesh piezoelectric material layers.

5.7.1 Example 1: A three-layer symmetric piezoelectric beam

The example chosen here is an aluminum core with surface bonded oppositely poled piezoelectric layers of G1195N material, as shown in Fig. 5.2. The material properties of the beam are:
Aluminum (Kapuria and Hagedorn, 2007): $E = 70.3\,GPa$, $\nu = 0.345$, $\rho = 2710\,kgm^{-3}$
G1195N (Peng et al., 1998): $E = 63\ GPa$, $\nu = 0.3$, $d_{31} = 254 \times 10^{-12}\ mV^{-1}$, $\epsilon_3 = 15 \times 10^{-9}\ Fm^{-1}$, $\rho = 7600\,kgm^{-3}$
This example is expected to show the improvement in terms of accuracy and efficiency of the present HSDT-*Coupled* formulation over the conventional HSDT formulations. To study the performance of HSDT-based smart beam formulations over a wide range of piezoelectric material proportion in total thickness (Thickness ratio: $r = (2h_p)/h$), the length (L) and total height (h) are taken as constant with values $100\ mm$ and $10\ mm$, respectively while the thicknesses of piezoelectric layer (h_p) and aluminum layer (h_{al}) are varied. For a comparative evaluation of the various HSDT formulations, converged results from ANSYS 2D analysis with a refined mesh size of 100×40 are used.

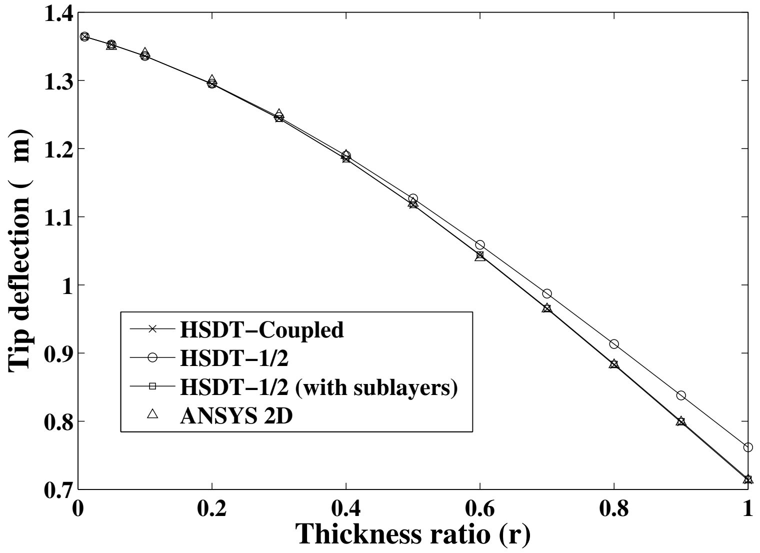

Figure 5.3: Example 1: Actuator configuration: Variation of the tip deflection with thickness ratio (r) for the three-layer cantilever beam actuated by $\pm 10\ volts$.

Static analysis: Actuator configuration

For actuator configuration, the interfaces of piezoelectric layers with aluminum are grounded and potentials of $\pm 10\ volts$ are applied on the free surface of the piezoelectric layers. The variation of tip deflection over a wide range of thickness ratio is plotted in Fig. 5.3. It is evident that the present HSDT-*Coupled* formulation gives accurate results as that of ANSYS 2D simulation. In the higher thickness ratio regimes, the both conventional HSDT-1 and HSDT-2 formulations converge to same inaccurate results, due to piezolocking effect. They demand sublayered modelling to achieve the same level of accuracy as of the present formulation. The results clearly show the advantage of HSDT-*Coupled* formulation, to efficiently handle the piezolocking effects.

The variation of error (%) in the tip deflection due to use of conventional HSDT formulations, with thickness ratio is plotted in Fig. 5.4. As the proportion of piezoelectric material in the beam increases, the error due to the linear assumption of through-thickness potential becomes significant. For both HSDT-1 and HSDT-2 formulations, the maximum difference is observed for a beam of pure piezoelectric material i.e. a *bimorph* configuration. Hence, the bimorph shown in Fig. 5.5 is considered for a detailed study of the induced potential effects.

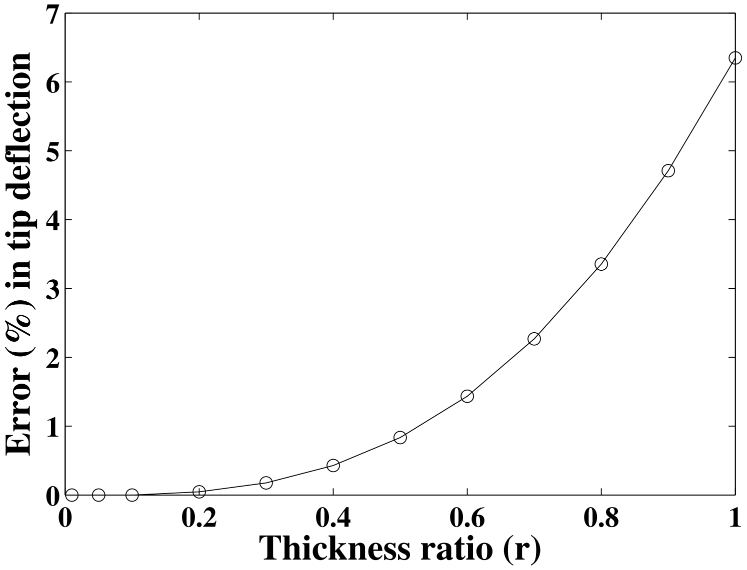

Figure 5.4: Example 1: Actuator configuration: Variation of error (%) in the tip deflection with thickness ratio (r), due to use of the conventional HSDT-1/2 formulations for the three-layer cantilever beam actuated by $\pm 10\ volts$.

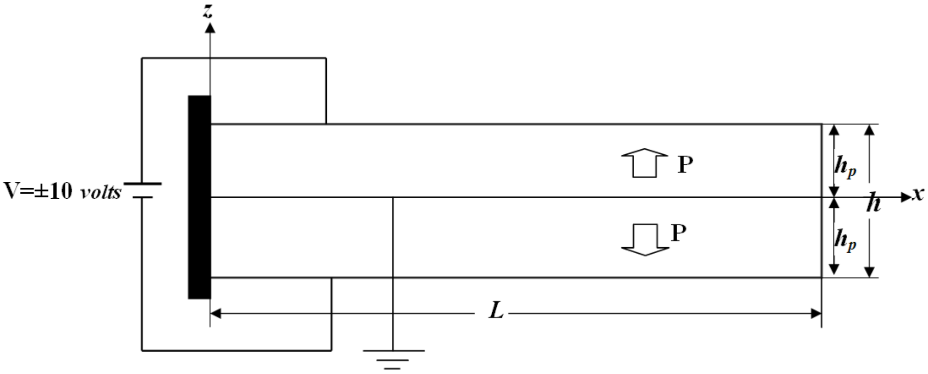

Figure 5.5: Example 1: Bimorph cantilever beam in the actuator configuration.

Table 5.1: Example 1: Actuator configuration: Tip deflection of the bimorph cantilever beam actuated by $\pm 10\, volts$ ($h = 10\, mm, L = 100\, mm$).

Formulations	Tip deflection (μm)
HSDT-1/2	0.762
HSDT-1/2 (with sublayers)	
2 sublayers/layer	0.725
3 sublayers/layer	0.719
4 sublayers/layer	0.716
5 sublayers/layer	0.715
ANSYS 2D	0.714
HSDT-*Coupled*	0.713

Table 5.1 shows the results for the tip deflection of the bimorph for various numbers of sublayers in the modelling with HSDT-1 and HSDT-2 formulations. Both the formulations converge to the same results. As seen from results, only with a sufficient number of sublayers in the modelling of piezoelectric layers, the HSDT-1 and HSDT-2 formulations converge to the accurate values as predicted by HSDT-*Coupled* and ANSYS 2D simulation.

Also, the comparison of results for transverse deflection along the length, through-thickness distributions of potential and axial stress for bimorph are plotted in Figs. 5.6, 5.7 and 5.8, respectively. The conventional HSDT-1 (Elshafei and Alraiess, 2013) and HSDT-2 (Chee et al., 1999) formulations suffer from loss of accuracy due to piezolocking. The results prove the ability of HSDT-*Coupled* to model the piezoelectric beam accurately as of ANSYS 2D and sublayered HSDT.

Static analysis: Sensor configuration

For sensor configuration, the three-layer cantilever beam shown in Fig. 5.2 is subjected to a tip load of $-1000\ N$. The results for tip deflection and potential developed at mid-span are plotted in Figs. 5.9 and 5.10, for various thickness ratios. From these plots, it is clear that present HSDT-*Coupled* formulation is able to yield accurate results as that of ANSYS 2D simulation over the entire range of thickness ratio. The conventional HSDT

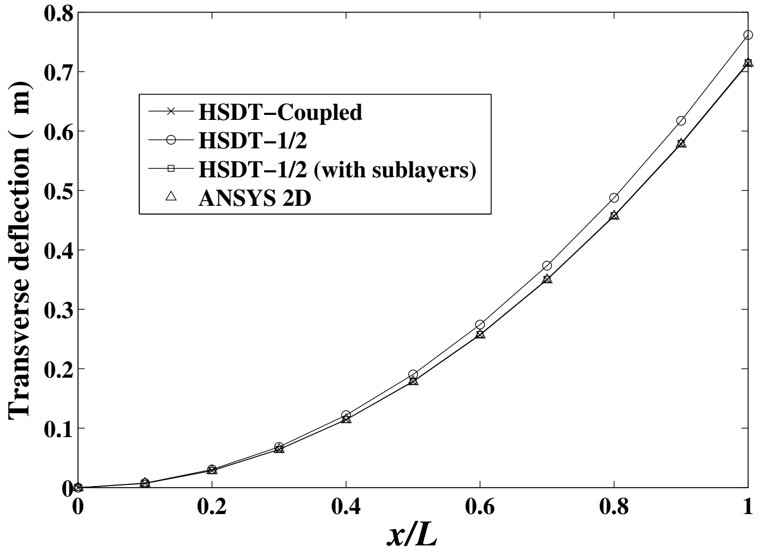

Figure 5.6: Example 1: Actuator configuration: Transverse deflection along the length of the bimorph cantilever beam actuated by ±10 $volts$.

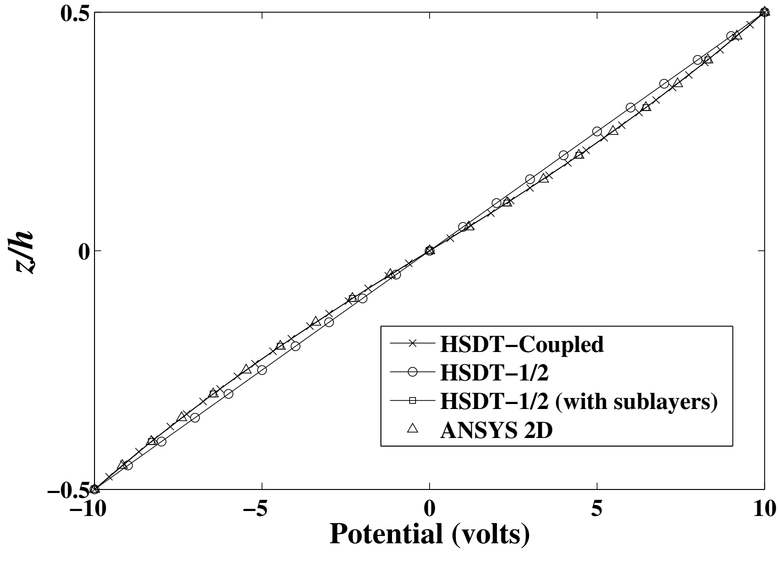

Figure 5.7: Example 1: Actuator configuration: Through-thickness potential distribution in the bimorph cantilever beam actuated by ±10 $volts$.

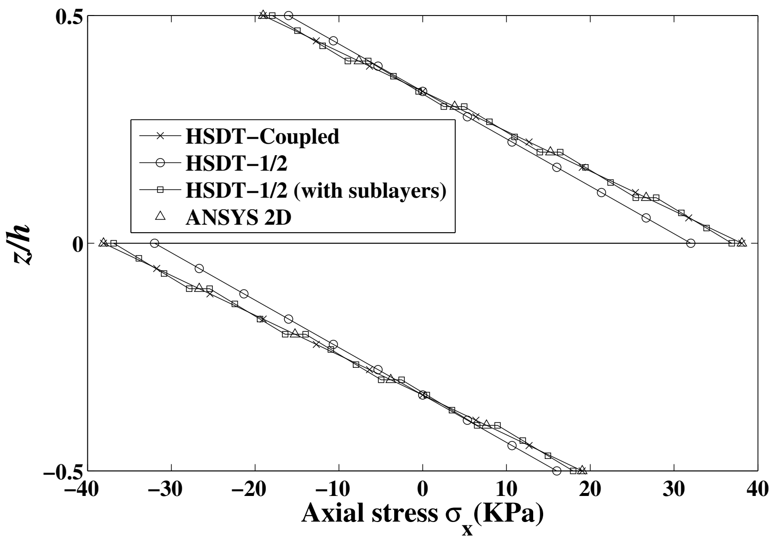

Figure 5.8: Example 1: Actuator configuration: Through-thickness axial stress distribution in the bimorph cantilever beam actuated by $\pm 10\ volts$.

formulations (Elshafei and Alraiess, 2013; Chee et al., 1999) suffer form piezolocking and do not maintain the accuracy consistently. They demand sublayered modelling to achieve same accuracy as that of HSDT-*Coupled*. The inaccuracy due to piezolocking is quantified in the error (%) plotted in Fig. 5.11. The variation of error (%) with thickness ratio shows that as we move from a beam of purely conventional material to a purely piezoelectric material beam i.e. bimorph, the error in the results increases significantly. Hence, the bimorph structure shown in Fig. 5.12 is considered here for detailed study of the induced potential effects.

Table 5.2 shows the results for tip deflection and potential developed across each piezoelectric layer at the mid-span of the bimorph, for different number of sublayers in the modelling with the conventional HSDT-1/2 formulations (Elshafei and Alraiess, 2013; Chee et al., 1999). As seen from results, only with sufficient number of sublayers in the modelling of piezoelectric layers, the conventional HSDT-1/2 formulations converge to the accurate results as predicted by HSDT-*Coupled* and ANSYS 2D simulation.

Also, the results for transverse deflection along the length, potential developed across each layer along the length, through-thickness potential at the mid-span of the bimorph are plotted in Figs. 5.13, 5.14 and 5.15, respectively. It is evident from the figures that results of the present HSDT-*Coupled* formulation closely match with 2D sim-

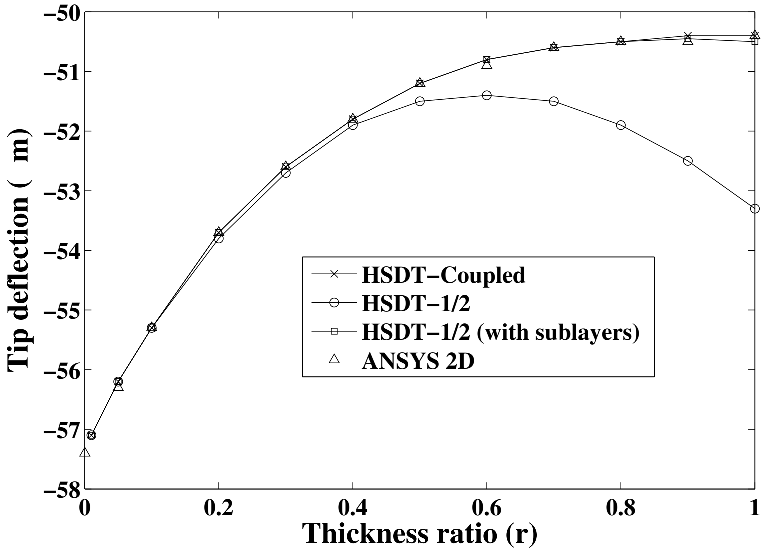

Figure 5.9: Example 1: Sensor configuration: Variation of the tip deflection with thickness ratio (r) for the three-layer cantilever beam subjected to a tip load of $-1000\ N$.

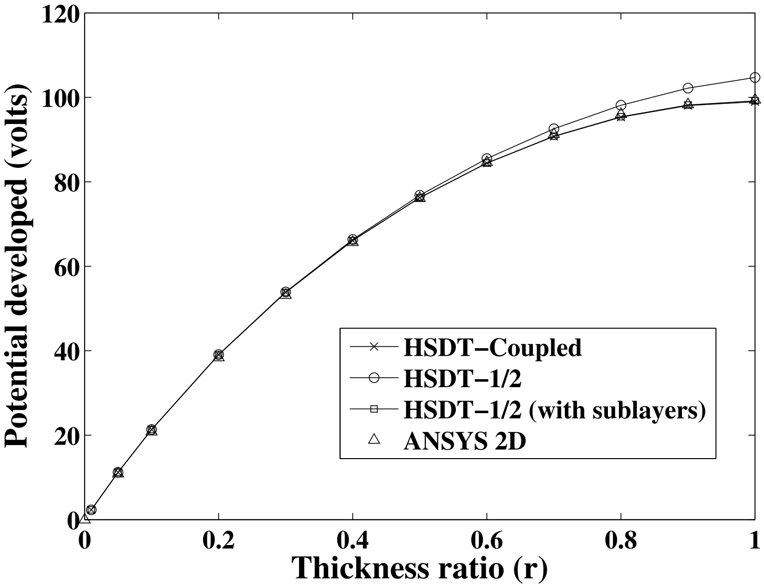

Figure 5.10: Example 1: Sensor configuration: Variation of the potential developed across each piezoelectric layer at the mid-span with thickness ratio (r) for the three-layer cantilever beam subjected to a tip load of $-1000\ N$.

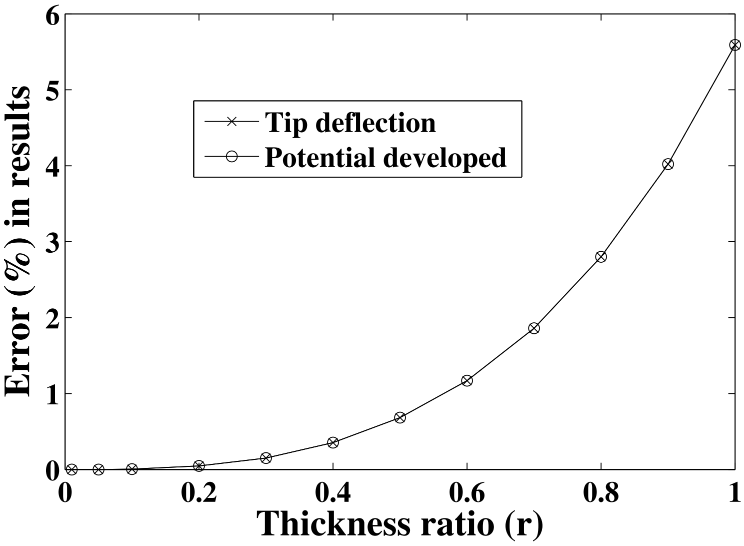

Figure 5.11: Example 1: Sensor configuration: Variation of error ($\%$) in the tip deflection and the potential developed with thickness ratio (r), due to use of the conventional HSDT-1/2 formulations for the three-layer cantilever beam subjected to a tip load of $-1000\ N$.

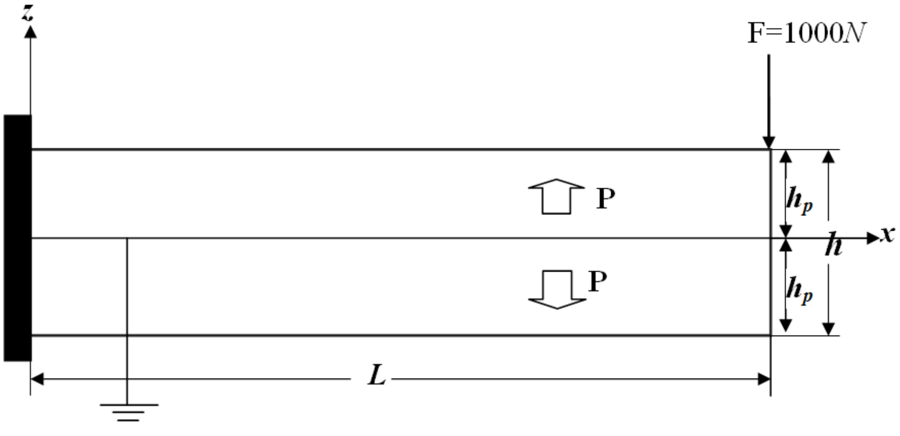

Figure 5.12: Example 1: Bimorph cantilever beam in the sensor configuration.

ulation, while conventional HSDT-1/2 formulations (Elshafei and Alraiess, 2013; Chee et al., 1999) need sublayered models to eliminate loss of accuracy due to piezolocking.

The axial stress distribution at the root of the bimorph is plotted in Fig. 5.16. As seen from the stress plot, the conventional HSDT-1/2 formulations under-predict the maximum value of stress developed and show discontinuity at the interface, which can be improved by the addition of sublayers in the models. The shear stress distribution across the thickness of the beam is plotted in Fig. 5.17. It is clear that the effect of the induced potential on the shear stress distribution is insignificant and hence the results from all the formulations considered are in good agreement.

Table 5.2: Example 1: Sensor configuration: Tip deflection and potential developed at the mid-span of the bimorph cantilever beam subjected to a tip load of $-1000\ N$ ($h = 10\ mm,\ L = 100\ mm$).

Formulation	Tip deflection (μm)	Potential ($volts$)
HSDT-1/2	-53.3	105.55
HSDT-1/2 (with sublayers)		
2 sublayers/layer	-51.1	101.23
3 sublayers/layer	-50.7	100.52
4 sublayers/layer	-50.6	100.25
5 sublayers/layer	-50.6	100.13
ANSYS 2D	-50.5	99.92
HSDT-*Coupled*	-50.5	99.92

Figs. 5.18 and 5.19 show the comparison of convergence characteristics of HSDT-based piezoelectric beam finite element formulations, for the tip deflection and potential developed at the root of the bimorph, respectively. It is noteworthy that HSDT-*Coupled* shows single-element convergence, closely reproducing the ANSYS-2D solutions for both the tip deflection and the potential developed. As evident from these figures, HSDT-1 (Elshafei and Alraiess, 2013) and HSDT-1 (with sublayers) models show a similar pattern of slow convergence. However, the HSDT-2 and HSDT-2 (with sublayers) models based on formulation of Chee et al. (1999) show improvement, exhibiting

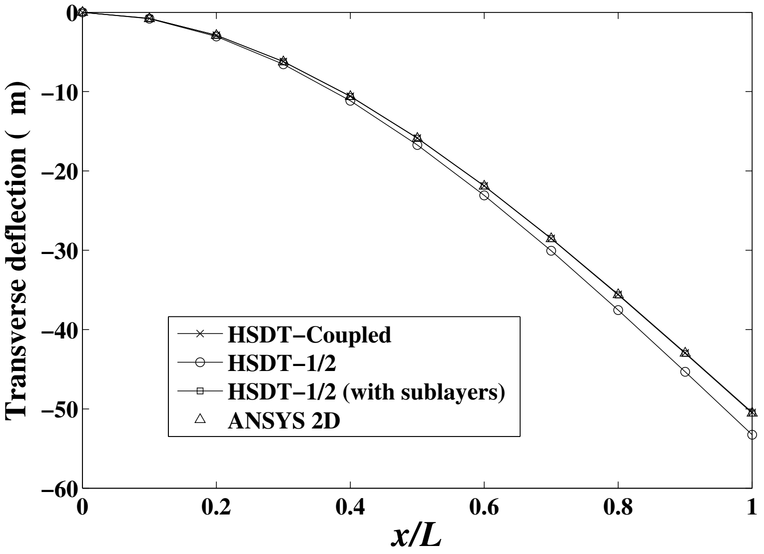

Figure 5.13: Example 1: Sensor configuration: Transverse deflection along the length of the bimorph cantilever beam subjected to a tip load of $-1000\ N$.

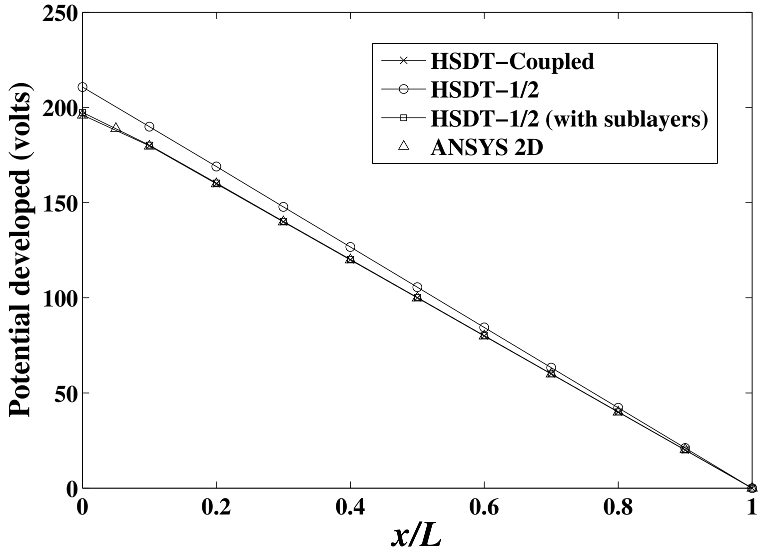

Figure 5.14: Example 1: Sensor configuration: Potential developed across each piezoelectric layer along the length of the bimorph cantilever beam subjected to a tip load of $-1000\ N$.

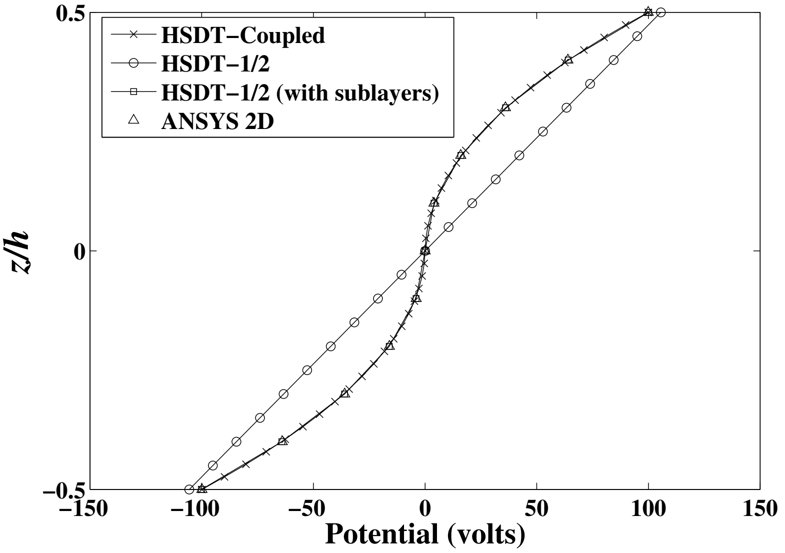

Figure 5.15: Example 1: Sensor configuration: Through-thickness potential distribution at the mid-span of the bimorph cantilever beam subjected to a tip load of $-1000\ N$.

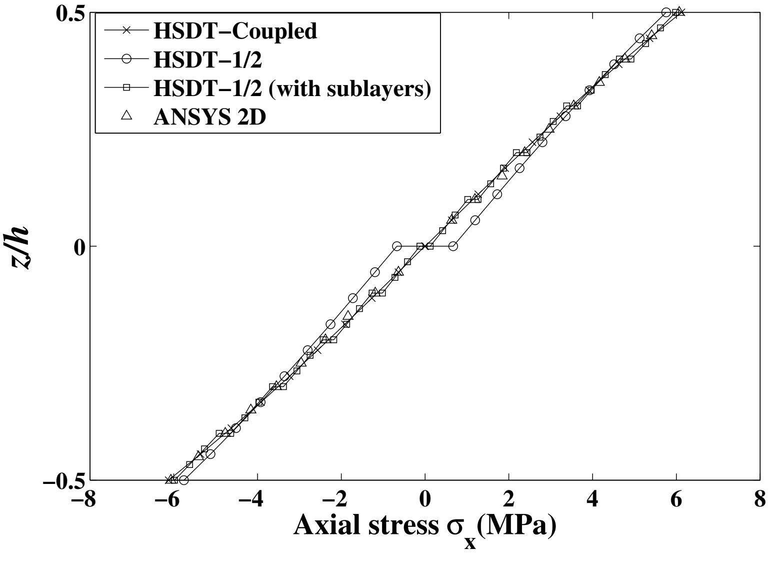

Figure 5.16: Example 1: Sensor configuration: Through-thickness axial stress distribution at the root of the bimorph cantilever beam subjected to a tip load of $-1000\ N$.

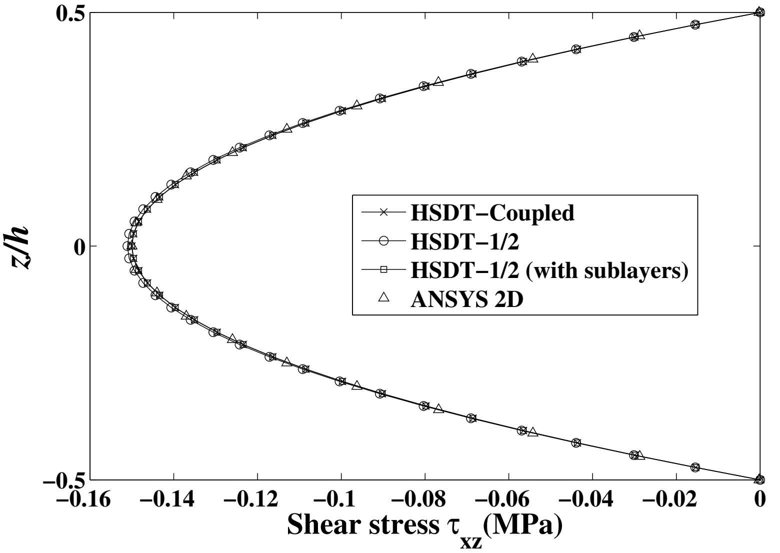

Figure 5.17: Example 1: Sensor configuration: Through-thickness shear stress distribution in the bimorph cantilever beam subjected to a tip load of $-1000\ N$.

single element convergence. It is observed that the sublayered versions of HSDT-1/2 models eventually converge to the accurate results. However, the conventional HSDT-1/2 models (Elshafei and Alraiess, 2013; Chee et al., 1999) overestimate the response and converge to inaccurate results, due to piezolocking effects. This example clearly reveals the role of the coupled polynomial interpolation in improving the accuracy and efficiency of the HSDT-*Coupled* formulation.

Modal analysis

The present formulation is validated here for accuracy and efficiency to predict natural frequencies of the smart cantilever shown in Fig. 5.2. The natural frequencies are evaluated for closed and open circuit electrical boundary conditions. For open circuit, only the interfaces of piezoelectric layers with aluminum core are grounded while, for closed circuit all the faces of piezoelectric layers are grounded. The variations of first natural frequencies in open and closed circuit electrical boundary conditions, with thickness ratio are plotted in Figs. 5.20 and 5.21, respectively. As seen from the figures, the present HSDT-*Coupled* predicts the accurate results as given by ANSYS 2D simulation over the entire range of thickness ratio. The conventional HSDT-1/2 formulations (Elshafei and Alraiess, 2013; Chee et al., 1999) show significant errors due to piezolocking in

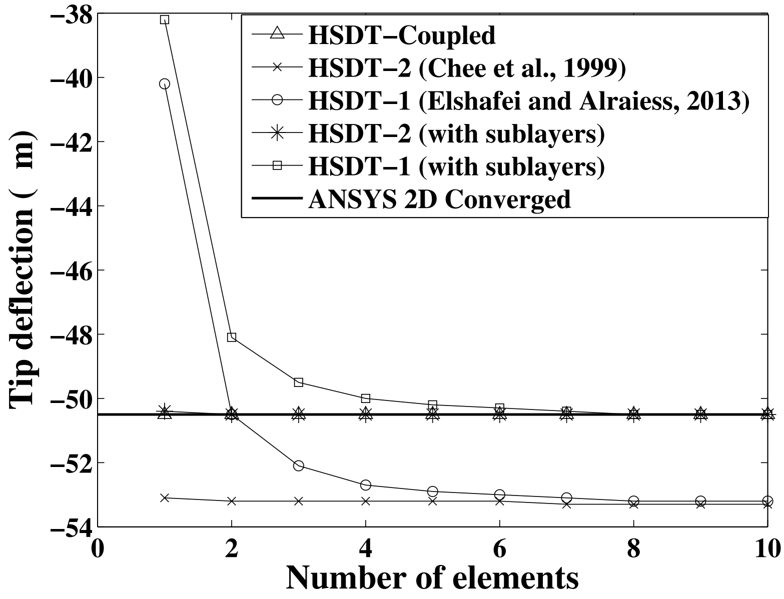

Figure 5.18: Example 1: Sensor configuration: Convergence characteristics of the HSDT-based piezoelectric beam finite elements to predict the tip deflection of the bimorph cantilever beam subjected to a tip load of $-1000\ N$.

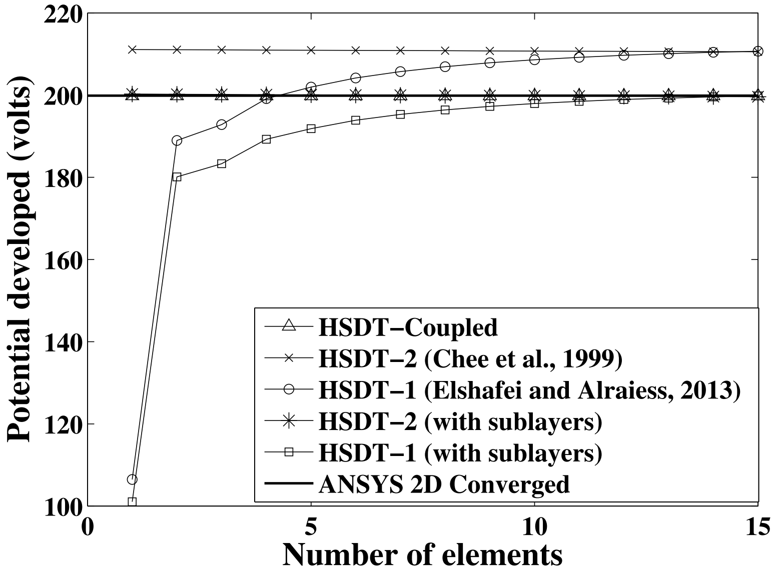

Figure 5.19: Example 1: Sensor configuration: Convergence characteristics of the HSDT-based piezoelectric beam finite elements to predict the potential developed across a piezoelectric layer at the root of the bimorph cantilever beam subjected to a tip load of $-1000\ N$.

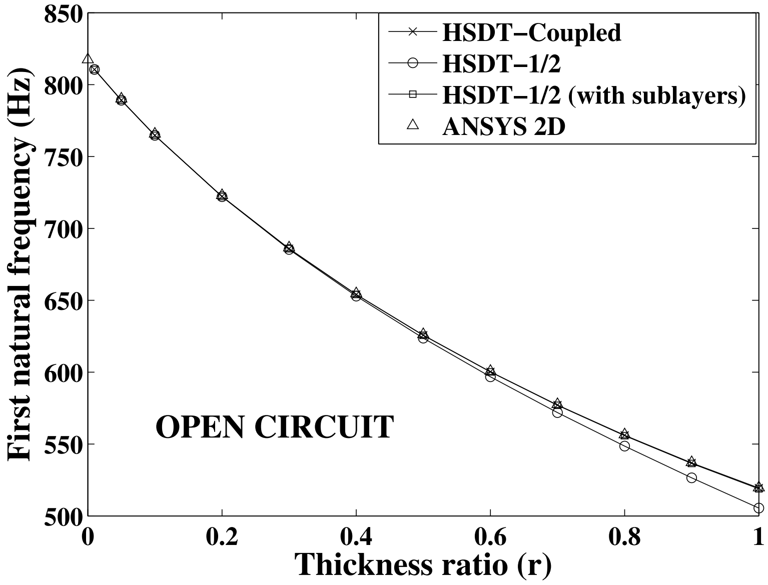

Figure 5.20: Example 1: Modal analysis: Variation of the first natural frequency with thickness ratio (r) for the three-layer cantilever beam in open circuit electrical boundary condition.

the higher thickness ratio regimes and require sublayered modelling to achieve accurate results. The variation of errors (%) with thickness ratio is plotted in Fig. 5.22. As seen from the error plot, the bimorph configuration shows maximum error.

The results for first five natural frequencies for the bimorph cantilever beam are tabulated in Table 5.3. As seen from the results the conventional HSDT-1/2 formulations suffer form piezolocking and require a number of sublayers to reproduce accurate results.

Figs. 5.23 and 5.24 show the comparison of convergence characteristics of HSDT-based piezoelectric beam finite element formulations to predict the first natural frequency of the bimorph in open and closed circuit conditions, respectively. It is noteworthy that HSDT-*Coupled* shows quick convergence, closely reproducing the ANSYS-2D solutions for both open and closed circuit conditions. HSDT-1 (Elshafei and Alraiess, 2013) and HSDT-1 (with sublayers) models show a similar pattern of slow convergence. The HSDT-2 and HSDT-2 (with sublayers) models based on formulation of Chee et al. (1999) show improved convergence compared to HSDT-1 and HSDT-1 (with sublayers). It is observed that the sublayered versions of HSDT- 1 and HSDT-2 eventually converge to the accurate results. However, conventional HSDT-1/2 models (Elshafei

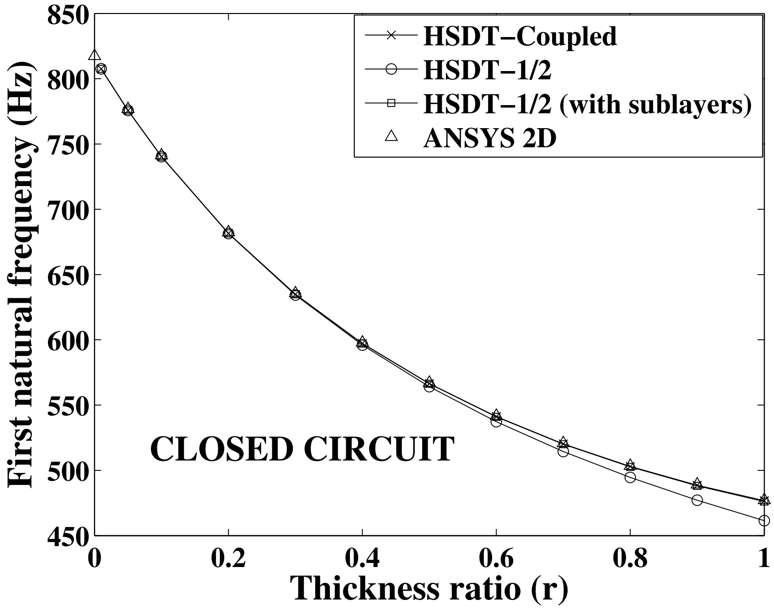

Figure 5.21: Example 1: Modal analysis: Variation of the first natural frequency with thickness ratio (r) for the three-layer cantilever beam in closed circuit electrical boundary condition.

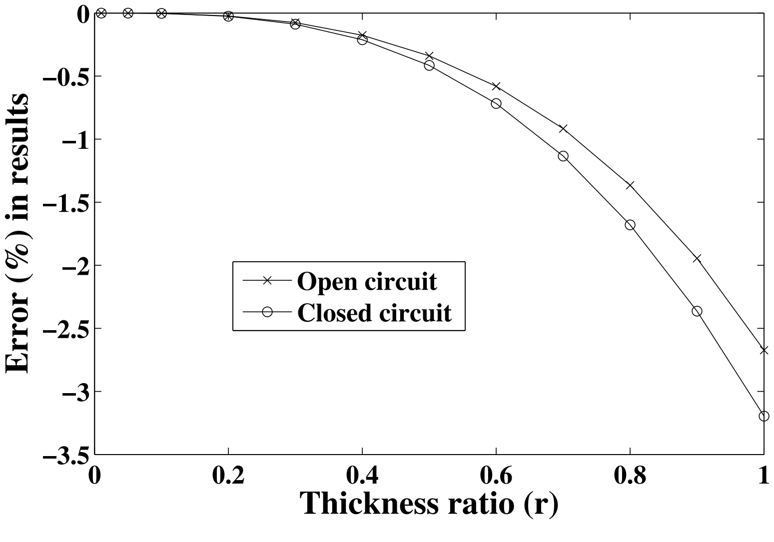

Figure 5.22: Example 1: Modal analysis: Variation of error (%) in the first natural frequency with thickness ratio (r), due to use of the conventional HSDT-1/2 formulations for the three-layer cantilever beam.

Table 5.3: Example 1: Natural frequencies in Hz for the bimorph cantilever beam ($h = 10\,mm,\ L = 100\,mm$).

Electrical Boundary condition	Mode No	HSDT-1/2	HSDT-1/2 (with sublayers)	ANSYS 2D	HSDT *Coupled*
Open Circuit	1^{st}	505.5	519.0	519.8	519.4
	2^{nd}	3012	3089	3089	3090
	3^{rd}	7867	8063	8046	8057
	4^{th}	8115	8115	8120	8115
	5^{th}	14169	14458	14448	14487
Closed Circuit	1^{st}	461.5	476.2	477.2	477.0
	2^{nd}	2768	2851	2857	2855
	3^{rd}	7198	7198	7206	7198
	4^{th}	7290	7493	7508	7506
	5^{th}	13247	13585	13610	13613

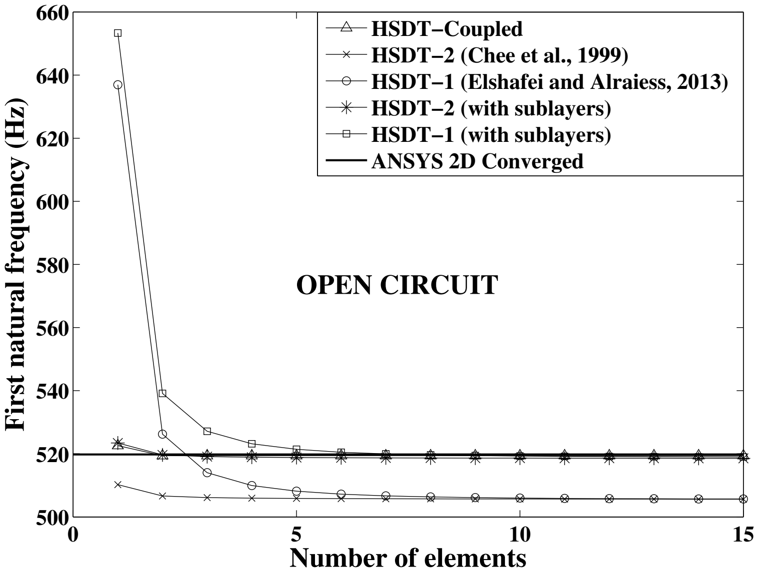

Figure 5.23: Example 1: Modal analysis: Convergence characteristics of the HSDT-based piezoelectric beam finite elements to predict the first natural frequency of the bimorph cantilever beam in open circuit electrical boundary condition.

and Alraiess, 2013; Chee et al., 1999) underestimate the response and converges to inaccurate results, due to piezolocking effects. This example clearly reveals the role of the coupled polynomial interpolation in improving the accuracy and efficiency of the HSDT-*Coupled* formulation.

5.7.2 Example 2: A two-layer asymmetric piezoelectric beam

The test problem chosen here is a two-layer asymmetric piezoelectric cantilever beam having a host layer made up of steel with a surface bonded piezoelectric layer of G1195N material at the top, as shown in Fig. 5.25. The material properties used are:
Steel (Carrera and Brischetto, 2008): $E = 210\ GPa$, $\nu = 0.3$, $\rho = 7850\ kgm^{-3}$
PZT G1195N (Peng et al., 1998): $E = 63\ GPa$, $\nu = 0.3$, $d_{31} = 254 \times 10^{-12}\ m/V$, $\epsilon_3 = 15 \times 10^{-9}\ F/m$, $\rho = 7600\ kgm^{-3}$.

This configuration is expected to show, in addition to piezolocking, the adverse effects of material locking on the convergence of the conventional HSDT piezoelectric beam finite elements and improved performance of the proposed HSDT-*Coupled* for-

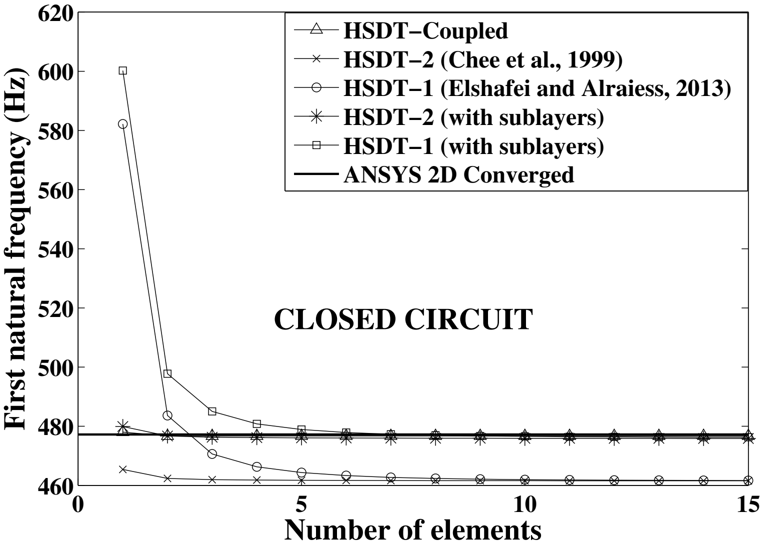

Figure 5.24: Example 1: Modal analysis: Convergence characteristics of the HSDT-based piezoelectric beam finite elements to predict the first natural frequency of the bimorph cantilever beam in closed circuit electrical boundary condition.

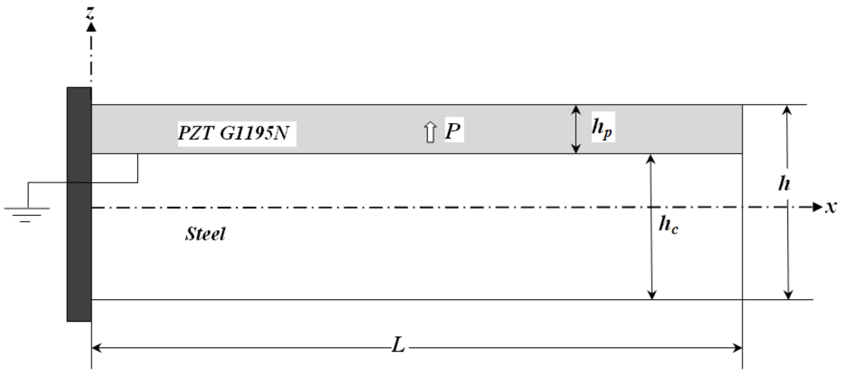

Figure 5.25: Example 2: Geometry of the two-layer cantilever beam with an asymmetrically bonded piezoelectric layer in extension mode.

mulation.

For the present study, the length and total height of the beam are taken as constant ($L = 100\ mm$, $h = 5\ mm$), while thicknesses of the piezoelectric layer (h_p) and the host layer (h_c) are varied. The performances of the HSDT-based piezoelectric beam finite elements are evaluated over a wide range of piezoelectric material proportion in the total beam thickness (thickness ratio: $r = h_p/h$). For a comparative evaluation of various HSDT-based formulations, the converged results from ANSYS 2D simulation with a mesh of 200×20 elements are used.

Static analysis: Sensor configuration

For sensor configuration, the beam shown in Fig. 5.25 is subjected to a tip load of $-1000\ N$. The variations of tip deflection, axial deflection and potential developed across the piezoelectric layer at the root of the beam, with thickness ratio are plotted in Figs. 5.26, 5.27 and 5.28, respectively.

As seen from these graphs, the present HSDT-*Coupled* formulation consistently gives accurate predictions of the results as given by ANSYS 2D simulation, over the entire range of thickness ratio and proves the versatility of the coupled polynomial based formulation. Due to the piezolocking effects, the conventional HSDT-1/2 formulations (Elshafei and Alraiess, 2013; Chee et al., 1999) do not perform consistently accurate. They demand sublayers in the modelling of piezolayer, to achieve the same consistent level of accuracy as of the present HSDT-*Coupled* formulation. The error (%) due to piezolocking in the conventional HSDT-1/2 formulations is quantified in Fig. 5.29 for various thickness ratios. It is seen that the error increases rapidly in the higher thickness ratio regimes.

Figs. 5.30 and 5.31 show the comparison of convergence characteristics of HSDT-based piezoelectric beam finite element formulations, for the tip deflection and the potential developed at the root, respectively. It is noteworthy that HSDT-*Coupled* shows single-element convergence, closely reproducing the ANSYS-2D solutions. Both HSDT-1 (Elshafei and Alraiess, 2013) and HSDT-1 (with sublayers) models show slow convergence patterns which are similar. It may be noted that HSDT-2 and HSDT-2 (with sublayers), which showed single element convergence for symmetric beam in the pre-

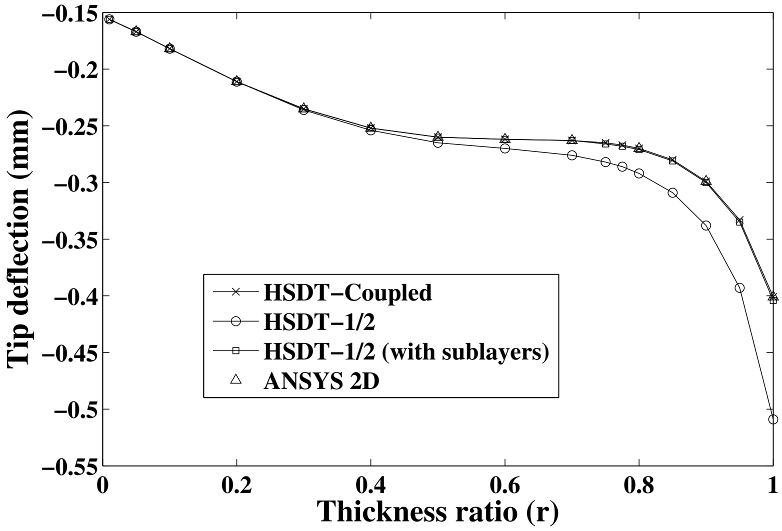

Figure 5.26: Example 2: Sensor configuration: Variation of the tip deflection with thickness ratio (r) for the asymmetric cantilever beam subjected to a tip load of $-1000N$.

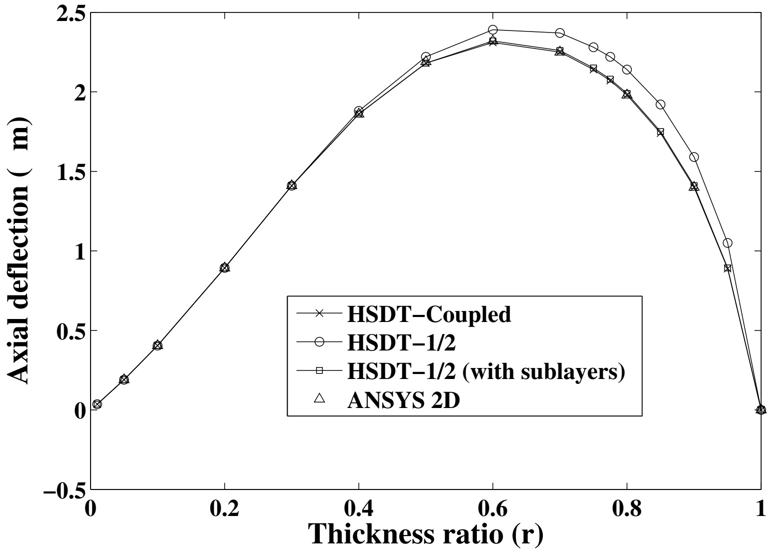

Figure 5.27: Example 2: Sensor configuration: Variation of the axial deflection with thickness ratio (r) for the asymmetric cantilever beam subjected to a tip load of $-1000N$.

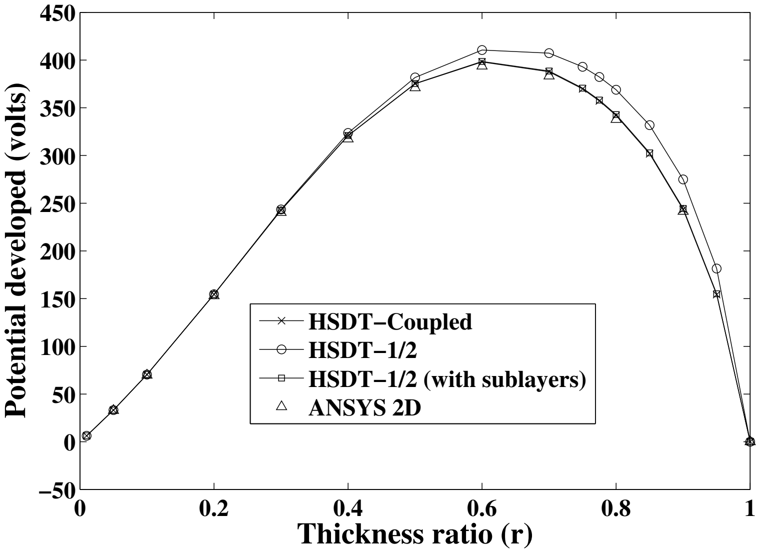

Figure 5.28: Example 2: Sensor configuration: Variation of the potential developed across piezoelectric layer at the root with thickness ratio (r) for the asymmetric cantilever beam subjected to a tip load of $-1000\,N$.

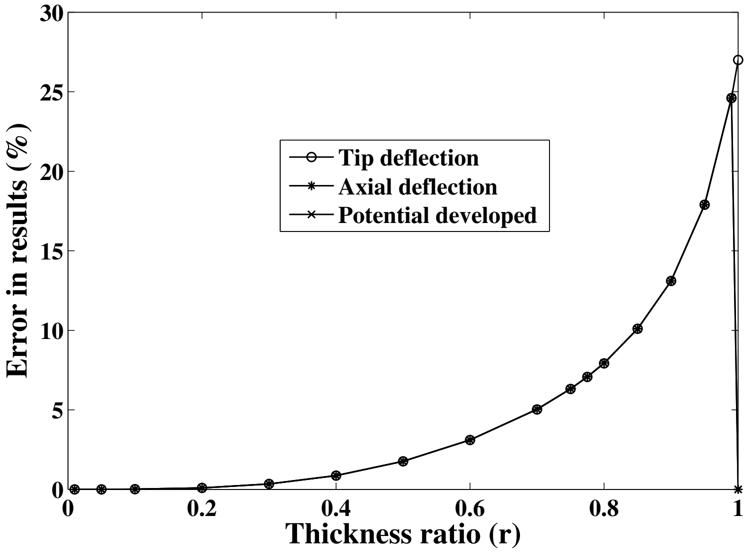

Figure 5.29: Example 2: Sensor configuration: Variation of error (%) in results with thickness ratio (r), due to use of the conventional HSDT-1/2 formulations.

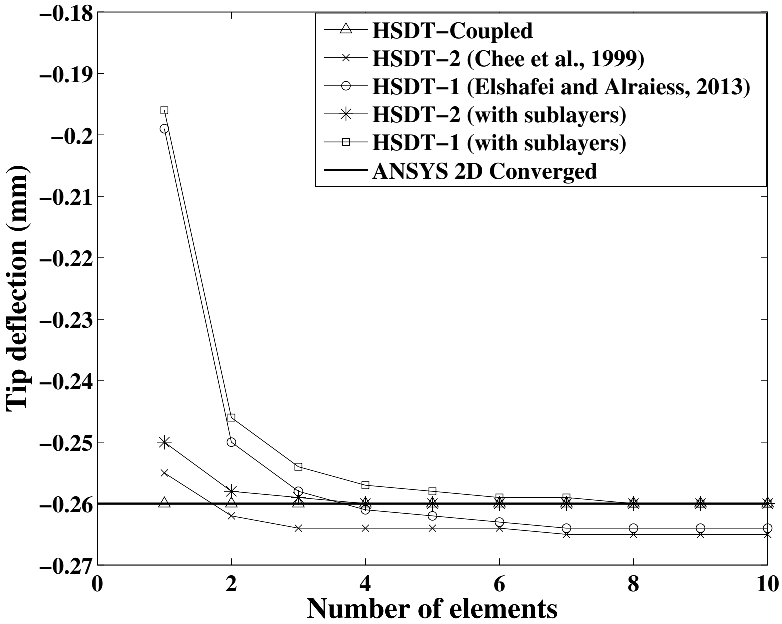

Figure 5.30: Example 2: Sensor configuration: Convergence characteristics of the HSDT-based piezoelectric beam finite elements to predict the tip deflection of the asymmetric cantilever beam ($r = 0.5$) subjected to a tip load of $-1000\ N$.

vious example (Example 1: Figs. 5.18 and 5.19) failed here for asymmetric beam, to reproduce the same performance, due to material locking. It is observed that the sublayered versions of HSDT-1/2 models eventually converges to the accurate results. However, the conventional HSDT-1/2 models (Elshafei and Alraiess, 2013; Chee et al., 1999) overestimate the response and converge to inaccurate results, due to piezolocking effects. This example clearly reveals the efficiency of the present coupled polynomial interpolation over the conventional independent polynomial interpolations.

The improved performance of the HSDT-*Coupled* can be attributed to the coupled polynomial representations of section rotation and axial displacement. The role of the coupled quadratic term in the axial displacement given by Eq. (5.30), in eliminating material locking is evident from the Table 5.4, where the results obtained with and without the coupled quadratic term are tabulated. The results prove the role of the coupled quadratic term in enabling HSDT-*Coupled* to yield single element convergence for the tip deflection and the potential developed. The results of asymmetric beam with $r = 0.5$ given in Table 5.4 are normalized with respect to the converged values obtained from ANSYS 2D simulation, $-0.2598\ mm$ for the tip deflection and $376.09\ volts$ for

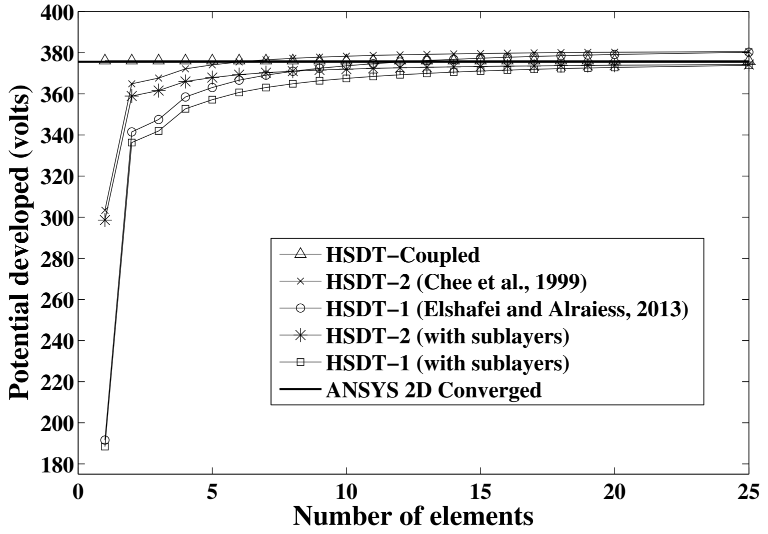

Figure 5.31: Example 2: Sensor configuration: Convergence characteristics of the HSDT-based piezoelectric beam finite elements to predict the potential developed at the root of the asymmetric cantilever beam ($r = 0.5$) subjected to a tip load of $-1000\ N$.

Table 5.4: Example 2: Role of coupled quadratic term in the field interpolation for axial displacement (Eq. (5.30)) in improving the convergence characteristics of HSDT-*Coupled* in static analysis.

Number of elements	Normalized tip deflection		Normalized potential developed at root	
	(with coupled quadratic term)	(without coupled quadratic term)	(with coupled quadratic term)	(without coupled quadratic term)
1	1.000	0.963	1.000	0.793
2	1.000	0.993	1.000	0.953
4	1.000	0.999	1.000	0.971
8	1.000	1.000	1.000	0.983
16	1.000	1.000	1.000	0.990

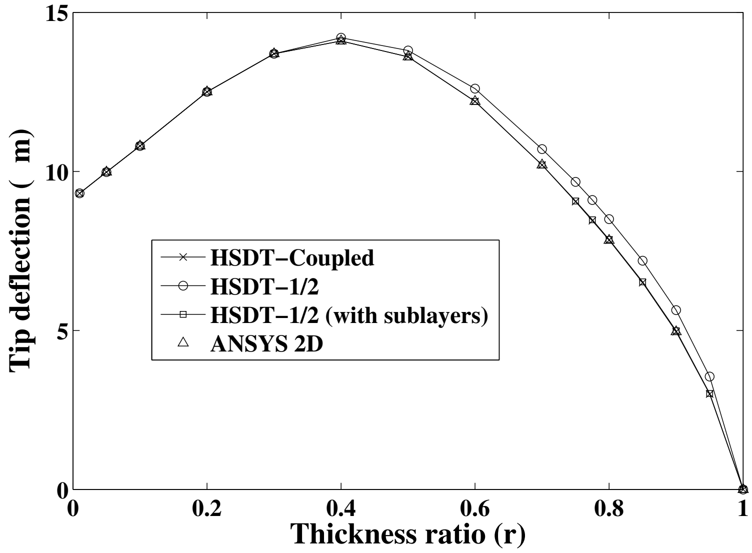

Figure 5.32: Example 2: Actuator configuration: Variation of the tip deflection with thickness ratio (r) for the asymmetric cantilever beam actuated by $100\ volts$.

the potential developed at the root.

Static analysis: Actuator configuration

For actuator configuration, the beam shown in Fig. 5.25 is subjected to a voltage of $100\ volts$. The variations of tip deflection and axial deflection, with thickness ratio are plotted in Figs. 5.32 and 5.33, respectively. As seen from these graphs, the present HSDT-*Coupled* formulation consistently gives accurate predictions of results as given by ANSYS 2D simulation, over the entire range of thickness ratio. Due to the piezolocking effects, the conventional HSDT-1/2 formulations (Elshafei and Alraiess, 2013; Chee et al., 1999) do not yield consistently accurate results. They demand sublayers in the modelling of piezolayer, to achieve the same consistent level of accuracy as of the present HSDT-*Coupled* formulation. The error due to piezolocking in the conventional HSDT-1/2 formulations is quantified in Fig. 5.34 for various thickness ratios.

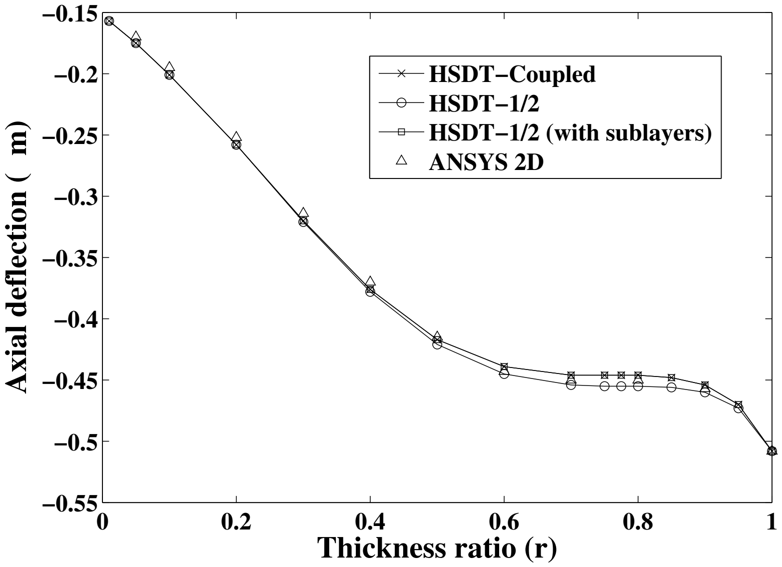

Figure 5.33: Example 2: Actuator configuration: Variation of the axial deflection with thickness ratio (r) for the asymmetric cantilever beam actuated by $100\ volts$.

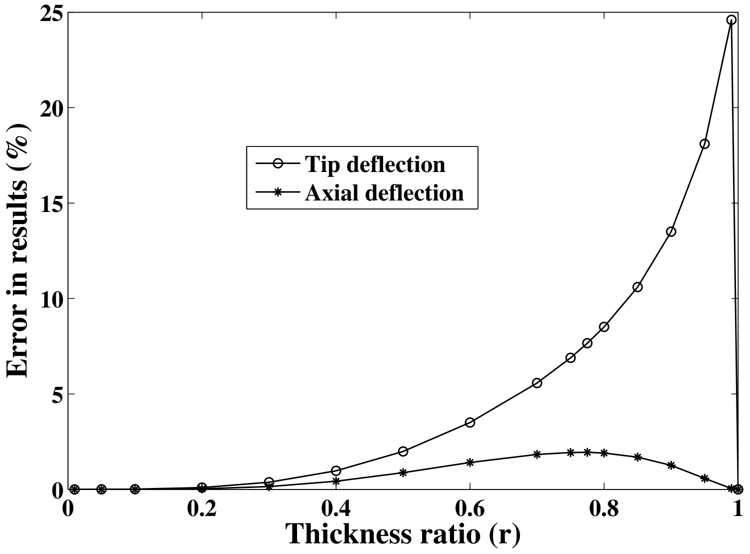

Figure 5.34: Example 2: Actuator configuration: Variation of error (%) in results with thickness ratio (r), due to use of the conventional HSDT-1/2 formulations.

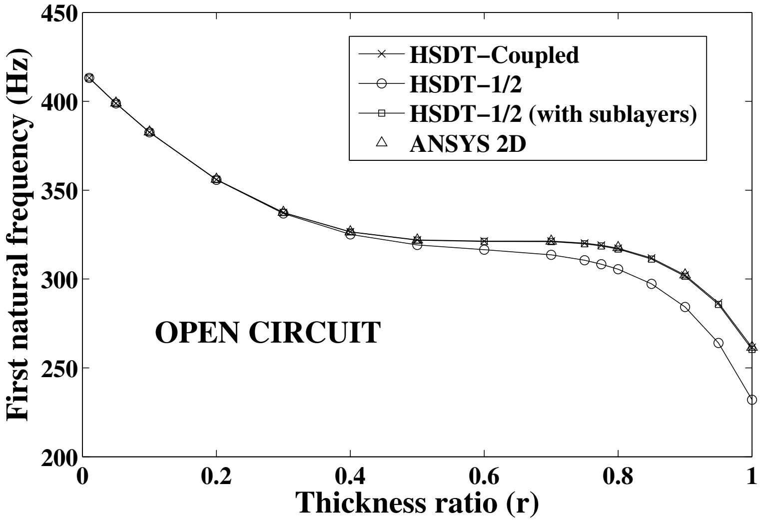

Figure 5.35: Example 2: Modal analysis: Variation of the first natural frequency with thickness ratio (r) for the asymmetric cantilever beam in open circuit electrical boundary condition.

Modal analysis

The present HSDT-*Coupled* formulation is evaluated here for its accuracy and efficiency to predict the natural frequencies of piezoelectric smart beams. The first natural frequency of the asymmetric piezoelectric beam shown in Fig. 5.25 is computed for both open and closed circuit electrical boundary conditions. For open circuit, only the interface of piezoelectric layer with host layer is grounded while for closed circuit, both faces of the piezoelectric layer are grounded. The variations of first natural frequencies with thickness ratio are plotted in Figs. 5.35 and 5.36 for open and closed circuit electrical boundary conditions, respectively. The results from the present HSDT-*Coupled* formulation agree very well with the results from ANSYS 2D simulation. This validates the use of the present coupled polynomial based interpolation displacement fields, to generate consistent element mass matrix. Due to piezolocking effects which are predominant in the higher thickness ratio regimes, the results from the conventional HSDT-1/2 formulations (Elshafei and Alraiess, 2013; Chee et al., 1999) significantly deviate from the accurate results and hence requires sublayered modelling to yield acceptable level of accuracy. The error (%) due to piezolocking in the conventional HSDT-1/2 formulations is plotted in Fig. 5.37 for various thickness ratios.

The convergence graphs for first natural frequency in both open and closed circuit

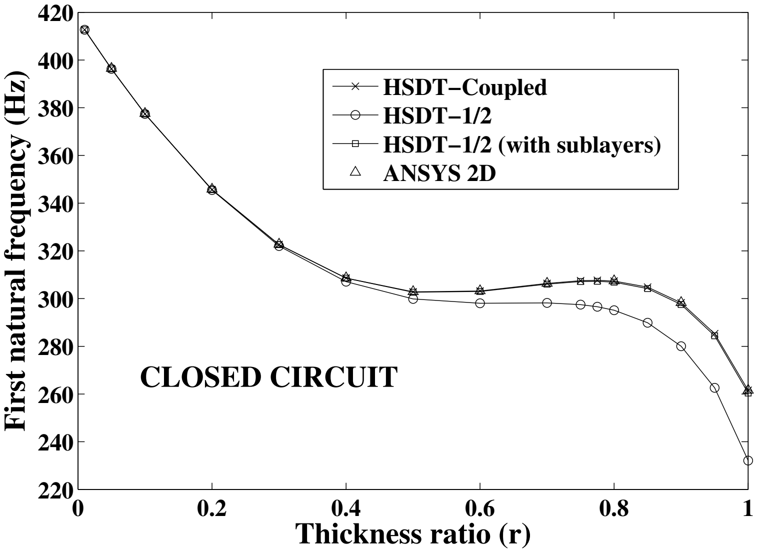

Figure 5.36: Example 2: Modal analysis: Variation of first natural frequency with thickness ratio (r) for the asymmetric cantilever beam in closed circuit electrical boundary condition.

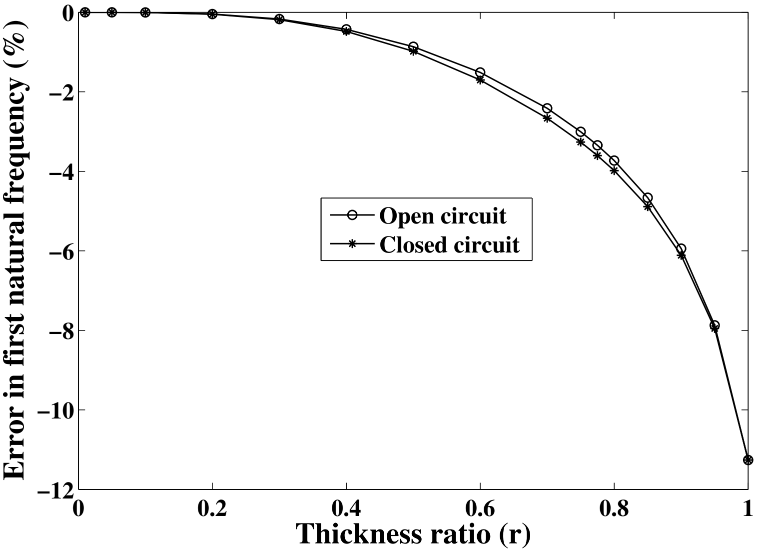

Figure 5.37: Example 2: Modal analysis: Variation of error (%) in results with thickness ratio (r), due to use of the conventional HSDT-1/2 formulation.

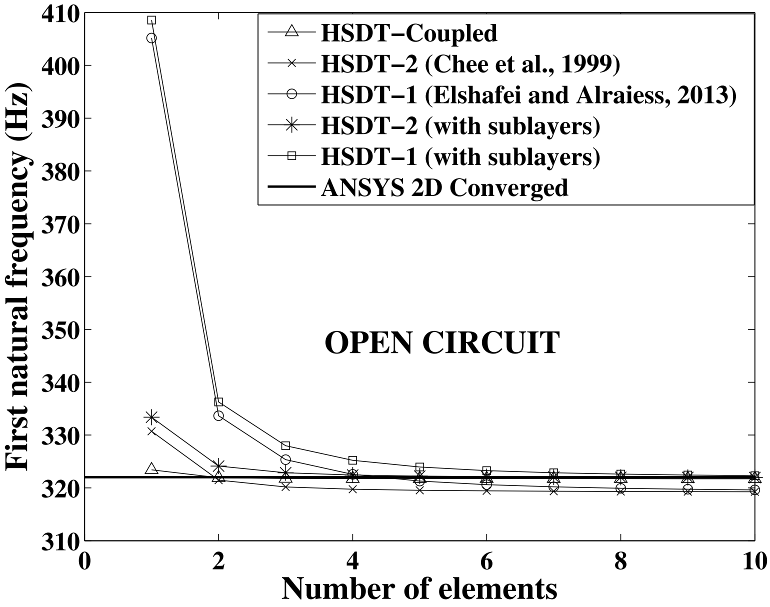

Figure 5.38: Example 2: Modal analysis: Convergence characteristics of the HSDT-based piezoelectric beam finite elements to predict the first natural frequency of the asymmetric cantilever beam ($r = 0.5$) in open circuit electrical boundary condition.

electrical boundary conditions are plotted in Figs. 5.38 and 5.39, respectively. The figures prove the efficacy of the present coupled polynomial interpolation based element stiffness matrix and the corresponding consistent element mass matrix in achieving improved convergence of natural frequencies. Both conventional HSDT-1 (Elshafei and Alraiess, 2013) and HSDT-1 (with sublayers) models show slow and similar convergence patterns. While comparing the performance of HSDT-2 (Chee et al., 1999) and HSDT-2 (with sublayers) models for symmetric beam case (Example 1: Figs. 5.23 and 5.24), it may be noted that there is noticeable deterioration of convergence characteristic for the present asymmetric beam. This deterioration is due to the presence of material locking effects. Also, the conventional HSDT-1/2 formulations (Elshafei and Alraiess, 2013; Chee et al., 1999) suffer from piezolocking, they require sublayers in the modelling, to converge to accurate results.

The role of the coupled quadratic term in the axial displacement given by Eq. (5.30), in eliminating material locking and improving the convergence is evident from the Table 5.5, where the results obtained with and without the coupled quadratic term are tabulated. The results prove the role of the coupled quadratic term in enabling HSDT-

Table 5.5: Example 2: Role of coupled quadratic term in the field interpolation for axial displacement (Eq. (5.30)) in improving the convergence characteristics of HSDT-*Coupled* in modal analysis.

Number of elements	Normalized natural frequency					
	1^{st}		2^{nd}		3^{rd}	
	coupled	linear	coupled	linear	coupled	linear
			Open circuit			
1	1.005	1.035	1.665	1.751	2.202	2.208
2	1.000	1.007	1.011	1.067	1.211	1.268
4	1.000	1.001	1.002	1.014	1.012	1.038
8	1.000	1.000	1.000	1.004	1.003	1.011
16	1.000	1.000	1.000	1.001	1.000	1.003
			Closed circuit			
1	1.005	1.049	1.663	1.793	2.266	2.273
2	1.000	1.011	1.011	1.094	1.255	1.311
4	1.000	1.002	1.002	1.021	1.013	1.057
8	1.000	1.000	1.000	1.005	1.003	1.015
16	1.000	1.000	1.000	1.002	1.000	1.004

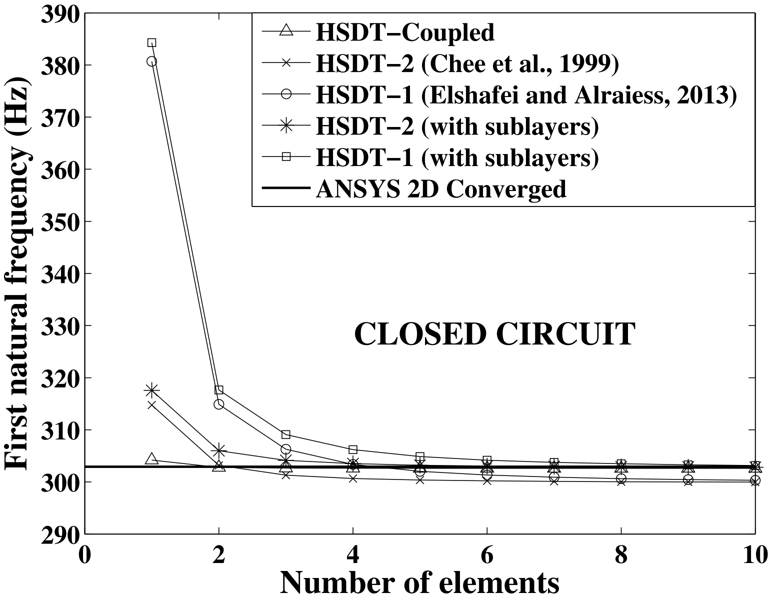

Figure 5.39: Example 2: Modal analysis: Convergence characteristics of the HSDT-based piezoelectric beam finite elements to predict the first natural frequency of the asymmetric cantilever beam ($r = 0.5$) in closed circuit electrical boundary condition.

Coupled to yield quick convergence for natural frequencies. The results of asymmetric beam with $r = 0.5$ given in Table 5.5 are normalized with respect to the converged values from HSDT-*Coupled*.

5.8 Summary

A coupled polynomial interpolation scheme for HSDT piezoelectric beam finite element has been proposed here to enhance its performance by eliminating material locking and piezolocking phenomena. A consistent interpolation for through-thickness potential derived from an electrostatic equilibrium equation has been proposed to eliminate piezolocking. A polynomial expression with a coupled quadratic term has been derived for axial displacement using the governing equilibrium equations. Similarly, a fully coupled quadratic polynomial expression has been derived for section rotation of the beam. The resulting coupled shape functions handle bending-extension coupling and bending-shear coupling in an efficient manner to eliminate material locking and improve curvature representation. While adopting coupled polynomial interpolation, the number of nodal mechanical degrees of freedoms are reduced by one for the present formulation. The merits of the present formulation over the conventional formulations have been proved by the comparison of the results for a set of test problems.

CHAPTER 6

CONCLUSIONS AND SCOPE FOR FUTURE WORK

6.1 Conclusions

This chapter outlines the important conclusions based on the results of study carried out in this thesis. The conclusions are presented in two categories:
(i) **General conclusions** pertaining to broad application of coupled polynomial interpolations in the field of displacement based extension mode piezoelectric finite elements.
(ii) **Specific conclusions** on the application of coupled polynomial interpolations for ESL extension mode piezoelectric beam elements studied in the chapters 3, 4 and 5.

6.1.1 General conclusions

- Coupled polynomial scheme facilitates use of additional higher-order consistent terms in the interpolation of the field variables. As the generalized coefficients associated with the higher-order terms are shared ones, they have far less total number of generalized coefficients compared to the independent polynomials of same order. Thus the coupled fields can be utilized to develop simple elements of improved efficiency and with lesser number of degrees of freedom.

- By properly incorporating the couplings in the polynomial description of field variables, the sensitiveness of the element performance to the geometric and material variations can be eliminated. This leads to finite elements which can perform consistently over a wide range of geometric and material parameter variations.

- The use of coupled polynomial fields significantly improves the convergence characteristics and accuracy of the present coupled piezoelectric element compared to their conventional counterparts.

- By making the best use of available generalized coefficients (and hence the element degrees of freedom) by the way of coupled coefficients in the field interpolations, the coupled displacement field elements prove to be the best cost effective compromise between complex higher-order elements and simple low-order elements based on the independent polynomial interpolations.

6.1.2 Specific conclusions

- The effect of induced potential coupling has been established which affects the accuracy of the piezoelectric beam finite elements. The loss of accuracy due to induced potential coupling is significant when the piezoelectric material dominates the beam cross-section.

- The use of a consistent field approximation for through-thickness electric potential makes the beam element capable of dealing with these accuracy loss due to piezolocking. The induced potential effects have been accommodated through higher-order terms coupled with the curvature strain in the description of the consistent electric potential. The versatility of the present coupled polynomial based EBT, FSDT, HSDT formulations is noteworthy, which yield accurate results irrespective of the piezoelectric material proportion of the beam cross-section.

- The present formulations with coupled consistent potential eliminate the requirement of sublayers in the mathematical modelling of piezolayers, for yielding accurate results.

- By properly incorporating the bending-extension coupling at the field interpolation of axial displacement, the piezoelectric beam element is rendered free of material locking. Hence the ESL EBT, FSDT and HSDT piezoelectric elements can be efficiently used for materially asymmetric beams.

- By properly incorporating the bending-shear coupling at the field interpolation of section rotation, the FSDT piezoelectric beam element is rendered free of shear locking. Hence the FSDT-*Coupled* piezoelectric elements can be efficiently used over a wide range of beam thickness regimes.

- The use of coupled quadratic polynomial for section rotation in FSDT and HSDT based formulations has enhanced the convergence by improved representation of curvature strain.

- In the proposed EBT-*Coupled* and FSDT-*Coupled* piezoelectric beam elements, the number and type of the nodal degrees of freedoms are preserved as of the conventional elements. The use of coupled polynomials have reduced the number of mechanical nodal degrees of freedom from *four* for the conventional HSDT to *three* for the proposed HSDT-*Coupled*, without affecting the applicability.
- The proposed coupled polynomial interpolation based piezoelectric elements are able to maintain the same level of accuracy and convergence characteristics over the entire range of material properties and geometric configuration of the piezoelectric beams.

In a nutshell, the proposed coupled polynomial based interpolation scheme proves to be the most accurate and efficient way to reduce a refined 2D piezoelectric finite element model to a truly 1D piezoelectric beam element model.

6.2 Scope for Future Work

- Extension of above methodologies to the development of efficient and accurate piezoelectric plate finite elements.
- Development of coupled polynomial based beam finite elements for the shear mode beams.

REFERENCES

1. Abramovich, H. (1998). Deflection control of laminated composite beams with piezoceramic layers-closed form solutions. *Composite Structures*, *43*, 217–231.

2. Abramovich, H., and Pletner, B. (1997). Actuation and sensing of piezolaminated sandwich type structures. *Composite Structures*, *38*, 17–27.

3. Ahmad, S. N., Upadhyay, C. S., and Venkatesan, C. (2005). Electroelastic analysis and layer-by-layer modeling of a smart beam. *AIAA Journal*, *43(12)*, 2606–2616.

4. Aldraihem, O. J., and Khdeir, A. A. (2000). Smart beams with extension and thickness-shear piezoelectric actuators. *Smart Materials and Structures*, *9*, 1–9.

5. Aldraihem, O. J., and Khdeir, A. A. (2003). Precise deflection analysis of beams with piezoelectric patches. *Composite Structures*, *60*, 135–143.

6. Aldraihem, O. J., Wetherhold, R. C., and Singh, T. (1996). Intelligent beam structures: Timoshenko theory vs euler-bernoulli theory. In *Proc. of the 1996 IEEE International Conference on Control Applications, Dearborn, MI (September 15-18, 1996).*

7. Aldraihem, O. J., Wetherhold, R. C., and Singh, T. (1997). Distributed control of laminated beams: Timoshenko theory vs. euler-bernoulli theory. *Journal of Intelligent Material Systems and Structures*, *8*, 149–157.

8. Allik, H., and Hughes, T. J. R. (1970). Finite element method for piezoelectric vibration. *International Journal for Numerical Methods in Engineering*, *2*, 151–157.

9. ANSYS-Release12 (2009). *Coupled-field analysis guide*. ANSYS Inc.

10. Balamurugan, V., and Narayanan, S. (2001). Active vibration control of piezolaminated smart beams. *Defence Science Journal*, *51*, 103–114.

11. Beheshti-Aval, S. B., and Lezgy-Nazargah, M. (2010). A finite element model for composite beams with piezoelectric layers using a sinus model. *Journal of Mechanics*, *26(3)*, 335–344.

12. Beheshti-Aval, S. B., and Lezgy-Nazargah, M. (2012). A coupled refined high-order global-local theory and finite element model for static electromechanical response of smart multilayered/sandwich beams. *Archieve of Applied Mechanics*, *82*, 1709–1752.

13. Beheshti-Aval, S. B., and Lezgy-Nazargah, M. (2013). Coupled refined layerwise theory for dynamic free and forced response of piezoelectric laminated composite and sandwich beams. *Meccanica*, *48*, 1479–1500.

14. Beheshti-Aval, S. B., Lezgy-Nazargah, M., Vidal, P., and Polit, O. (2011). A refined sinus finite element model for the analysis of piezoelectric-laminated beams. *Journal of Intelligent Material Systems and Structures*, *22*, 203–219.

15. Bendary, I. M., Elshafei, M. A., and Riad, A. M. (2010). Finite element model of smart beams with distributed piezoelectric actuators. *Journal of Intelligent Material Systems and Structures*, *21*, 747–758.

16. Benjeddou, A., Trindade, M. A., and Ohayon, R. (1997). A unified beam finite element model for extension and shear piezoelectric actuation mechanisms. *Journal of Intelligent Material Systems and Structures*, *8*, 1012–1025.

17. Benjeddou, A., Trindade, M. A., and Ohayon, R. (2000). Piezoelectric actuation mechanisms for intelligent sandwich structures. *Smart Materials and Structures*, *9*, 328–335.

18. Blandford, G. E., Tauchert, T. R., and Du, Y. (1999). Self-strained piezothermoelastic composite beam analysis using first-order shear deformation theory. *Composites: Part B*, *30*, 51–63.

19. Bona, B., Brusa, E., Canestrelli, P., Genta, G., and Tonoli, A. (1994). Finite element modeling and experimental validation of an elastic beam with surface bonded piezoelectric devices. In *Proc. of 1994 IEEE International Conference on Robotics and Automation (May 1994).*

20. Bruant, I., Coffignal, G., Lene, F., and Verge, M. (2001). Active control of beam structures with piezoelectric actuators and sensors: modeling and simulation. *Smart Materials and Structures*, *10*, 404–408.

21. Carpenter, M. J. (1997). Using energy methods to derive beam finite elements incorporating piezoelectric materials. *Journal of Intelligent Matererial Systems and Structures*, *8*, 26–40.

22. Chandrashekhara, K., and Varadarajan, S. (1997). Adaptive shape control of composite beams with piezoelectric actuators. *Journal of Intelligent Material Systems and Structures*, *8*, 112–124.

23. Chee, C. Y. K., Tong, L., and Steven, G. P. (1999). A mixed model for composite beams with piezoelectric actuators and sensors. *Smart Materials and Structures*, *8*, 417–432.

24. Crawley, E. F., and Anderson, E. H. (1990). Detailed models of piezoceramic actuation of beams. *Journal of Intelligent Matererial Systems and Structures*, *1*, 4–25.

25. Crawley, E. F., and deLuis, J. (1987). Use of piezoelectric actuators as elements of intelligent structures. *AIAA Journal*, *25*, 1373–1385.

26. Donthireddy, P., and Chandrashekhara, K. (1996). Modeling and shape control of composite beams with embedded piezoelectric actuators. *Composite Structures*, *35*, 237–244.

27. Duczek, S., and Gabbert, U. (2013). Anisotropic hierarchic finite elements for the simulation of piezoelectric smart structures. *Engineering Computations*, *30(5)*, 682–706.

28. Edery-Azulay, L., and Abramovich, H. (2004). Piezoelectric actuation and sensing mechanisms–closed form solutions. *Composite Structures*, *64*, 443–453.

29. Elshafei, M. A., and Alraiess, F. (2013). Modeling and analysis of smart piezoelectric beams using simple higher order shear deformation theory. *Smart Materials and Structures*, *22*, 35006–35019.

30. Foutsitzi, G., Marinova, D., Hadjigeorgiou, E., and Stavroulakis, G. (2002). Finite element modelling of optimally controlled smart beams. In *28Ih Summer School: Applications of Mathematics in Engineering and Economics (June 8-11, 2002), Sozopol, Bulgaria*.

31. Foutsitzi, G., Marinova, D. G., Hadjigeorgiou, E., and Stavroulakis, G. E. (2003). Robust h2 vibration control of beams with piezoelectric sensors and actuators. In *Proc. 2003 International Conference on Physics and Control, (Vol. 1, pp. 157-162) IEEE*.

32. Friedman, Z., and Kosmatka, J. B. (1993). An improved two-node timoshenko beam finite element. *Computers and Structures*, *47*, 473–481.

33. Gaudenzi, P. (1998). Exact higher order solutions for a simple adaptive structures. *International Journal of Solids and Structures*, *35*, 3595–3610.

34. Gaudenzi, P., Carbonaro, R., and Benzi, E. (2000). Control of beam vibrations by means of piezoelectric devices: theory and experiments. *Composite Structures*, *50*, 373–379.

35. Ha, S. K., Keilers, C., and Chang, F. K. (1992). Finite element analysis of composite structures containing distributed piezoceramic sensors and actuators. *AIAA Journal*, *30(3)*, 772–780.

36. Hanagud, S., Obal, M. W., and Calise, A. J. (1992). Optimal vibration control by the use of piezoceramic sensors and actuators. *Journal of Guidance, Control, and Dynamics*, *15*, 1199–1206.

37. Heyliger, P. R., and Reddy, J. N. (1988). A higher order beam finite element for bending and vibration problems. *Journal of Sound and Vibration*, *126*, 309–326.

38. Huang, D., and Sun, B. H. (2001). Approximate solution on smart composite beams by using matlab. *Composite Structures*, *54*, 197–205.

39. Ikeda, T. (1996). *Fundamentals of piezoelectricity*. Oxford University Press.

40. Jiang, J. P., and Li, D. X. (2007). A new finite element model for piezothermoelastic composite beam. *Journal of Sound and Vibration*, *306*, 849–864.

41. Kapuria, S., and Alam, N. (2006). Effcient layerwise finite element model for dynamic analysis of laminated piezoelectric beams. *Computational Methods in Applied Mechanics and Engineering*, *195*, 2742–2760.

42. Kapuria, S., Dumir, P. C., Ahmed, A., and Alam, N. (2004). Finite element model of efficient zig-zag theory for static analysis of hybrid piezoelectric beams. *Computational Mechanics*, *34*, 475–483.

43. Kapuria, S., and Hagedorn, P. (2007). Unified efficient layerwise theory for smart beams with segmented extension/shear mode, piezoelectric actuators and sensors. *Jornal of Mechanics of Materials and Structures*, *2*, 1267–1298.

44. Khdeir, A. A., and Aldraihem, O. J. (2001). Deflection analysis of beams with extension and shear piezoelectric patches using discontinuity functions. *Smart Materials and Structures*, *10*, 212–220.

45. Khdeir, A. A., Darraj, E., and Aldraihem, O. J. (2012). Free vibration of cross ply laminated beams with multiple distributed piezoelectric actuators. *Journal of Mechanics*, *28(1)*, 217–227.

46. Koko, T. S., Orisamolu, I. R., Smith, M. J., and Akpan, U. O. (1997). Finite-element-based design tool for smart composite structures. In *Proc. SPIE 3039, Smart Structures and Materials 1997: Mathematics and Control in Smart Structures, 125 (June 13, 1997).*

47. Komeili, A., Akbarzadeh, A. H., Doroushi, A., and Eslam, M. R. (2011). Static analysis of functionally graded piezoelectric beams under thermo-electro-mechanical loads. *Advances in Mechanical Engineering*, *Article ID 153731*, 10 pages, doi:10.1155/2011/153731.

48. Krommer, M., and Irschik, H. (1999). On the influence of the electric field on free transverse vibrations of smart beams. *Smart Materials and Structures*, *8*, 401–410.

49. Kumar, K. R., and Narayanan, S. (2008). Active vibration control of beams with optimal placement of piezoelectric sensor/actuator pairs. *Smart Materials and Structures*, *17*, 55008–55022.

50. Lee, S., Cho, B. C., Park, H. C., Goo, N. S., and Yoon, K. J. (2004). Piezoelectric actuator-sensor analysis using a three-dimensional assumed strain solid element. *Journal of Intelligent Matererial Systems and Structures*, *15*, 329–338.

51. Lezgy-Nazargah, M., Vidal, P., and Polit, O. (2013). An efficient fnite element model for static and dynamic analyses of functionally graded piezoelectric beams. *Composite Structures*, *104*, 71–84.

52. Lin, M. W., Abatan, A. O., and Rogers, C. A. (1994). Application of commercial finite element codes for the analysis of induced strain-actuated structures. *Journal of Intelligent Matererial Systems and Structures*, *5*, 869–875.

53. Manjunath, T. C., and Bandyopadhyay, B. (2006). Smart control of cantilever structures using output feedback. *International Journal of Simulation Systems, Science & Technology*, *7*, 51–68.

54. Moutsopoulou, A., Stavroulakis, G., and Pouliezos, T. (2012). Simulation and modelling of smart beams with robust control subjected to wind induced vibration. *Open Journal of Civil Engineering*, *2*, 106–114.

55. Moutsopoulou, A. J., Pouliezos, A. T., and Stavroulakis, G. E. (2013). Modeling of active vibration control in smart structures. *Journal of Civil Engineering and Science*, *2*, 48–61.

56. Narayanan, S., and Balamurugan, V. (2003). Finite element modelling of piezolaminated smart structures for active vibration control with distributed sensors and actuators. *Journal of Sound and Vibration*, *262*, 529–562.

57. Neto, M. A., Yu, W., and Roy, S. (2009). Two finite elements for general composite beams with piezoelectric actuators and sensors. *Finite Elements in Analysis and Design*, *45*, 295–304.

58. Peng, X. Q., Lam, K. Y., and Liu, G. R. (1998). Active vibration control of composite beams with piezoelectrics: A finite element model with third order theory. *Journal of Sound and Vibration*, *209*, 635–650.

59. Plagianakos, T. S., and Saravanos, D. A. (2005). Coupled high-order shear layerwise analysis of adaptive sandwich piezoelectric composite beams. *AIAA Journal*, *43*, 885–894.

60. Rachmadini, Y., Lee, S., Park, H. C., Yoon, K. J., and Goo, N. S. (2005). The effect of electro-mechanical coupling stiffness on the through-the-thickness electric potential distribution of piezoelectric actuators. *Smart Materials and Structures*, *14*, 754–758.

61. Raja, S., Pratap, G., and Sinha, P. K. (2002). Active vibration control of composite sandwich beams with piezoelectric extension-bending and shear actuators. *Smart Materials and Structures*, *11*, 63–71.

62. Raja, S., Sreedeep, R., and Pratap, G. (2004). Bending behavior of hybrid-actuated piezoelectric sandwich beams. *Journal of Intelligent Material Systems and Structures*, *15*, 611–619.

63. Ray, M. C., and Mallik, N. (2004). Active control of laminated composite beams using a piezoelectric fiber reinforced composite layer. *Smart Materials and Structures*, *13*, 146–152.

64. Robbins, D. H., and Reddy, J. N. (1991). Analysis of piezoelectrically actuated beams using a layerwise displacement theory. *Computers and Structures*, *41*, 265–279.

65. Sadilek, P., and Zemcik, R. (2010). Frequency responce analysis of hybrid piezoelectric cantilever beam. *Engineering Mechanics*, *17*, 73–82.

66. Saravanos, D. A., and Heyliger, P. R. (1995). Coupled layerwise analysis of composite beams with embedded piezoelectric sensors and actuators. *Journal of Intelligent Material Systems and Structures*, *6*, 350–363.

67. Sedaghati, R., Zabihollah, A., and Ahari, M. (2006). Sensitivity analysis and optimal design of smart piezolaminated composite beams. *AIAA Journal*, *44*, 2987–2996.

68. Stavroulakis, G. E., Foutsitzi, G., Hadjigeorgiou, E., Marinova, D., and Baniotopoulos, C. C. (2005). Design and robust optimal control of smart beams with application on vibrations suppression. *Advances in Engineering Software*, *36*, 806–813.

69. Sun, B., and Huang, D. (2000). Analytical vibration suppression analysis of composite beams with piezoelectric laminae. *Smart Materials and Structures*, *9*, 751–760.

70. Sze, K. Y., Yang, X. M., and Fan, H. (2004). Electric assumptions for piezoelectric laminate analysis. *International Journal of Solids and Structures*, *41*, 2363–2382.

71. Tzou, H. S., and Tseng, C. I. (1988). Active vibration control of distributed parameter systems by finite element method. *Computers in Engineering*, *3*, 599–604.

72. Tzou, H. S., and Tseng, C. I. (1991). Distributed vibration control and identification of coupled elastic/piezoelectric systems: Finite element formulation and applications. *Mechanical Systems and Signal Processing*, *5*, 215–231.

73. Waisman, H., and Abramovich, H. (2002). Active stiffening of laminated composite beams using piezoelectric actuators. *Composite Structures*, *58*, 109–120.

74. Wang, C. M., Ang, K. K., and Ajit, A. (1999). Shape control of laminated cantilevered beams with piezoelectric actuators. *Journal of Intelligent Matererial Systems and Structures*, *10*, 164–175.

75. Wang, F., Tang, G. J., and Li, D. K. (2007). Accurate modeling of a piezoelectric composite beam. *Smart Materials and Structures*, *16*, 1595–1602.

76. Wang, S. Y. (2004). A finite element model for the static and dynamic analysis of a piezoelectric bimorph. *International Journal of Solids and Structures*, *41*, 4075–4096.

77. Zemcik, R., and Sadilek, P. (2007). Modal analysis of beam with piezoelectric sensors a actuators. *Applied and Computational Mechanics*, *1*, 381–386.

78. Zhang, X. D., and Sun, C. T. (1996). Formulation of an adaptive sandwich beam. *Smart Materials and Structures*, *5*, 814–823.

79. Zhou, Y., Chen, Y., and Ding, H. (2005). Analytical solutions to piezoelectric bimorphs based on improved fsdt beam model. *Smart Structures and Systems*, *1(3)*, 309–324.

APPENDIX A

REDUCED CONSTITUTIVE RELATIONS

A piezoelectric material with isotropic/specially orthotropic properties is considered here. It has axes of material symmetry parallel to the beam axes, in which an electric field is applied in the transverse (z) direction. The elastic, piezoelectric and dielectric material constants are denoted by C_{ij}, e_{kj} $(i, j = 1, ..., 6)$ and ϵ_k $(k = 1, 2, 3)$, respectively. For extension mode of operation, the transversely poled piezoelectric material is bonded/embedded in the host structure. The coupled constitutive equation for such a material is given as (Ikeda, 1996):

$$\begin{bmatrix} \sigma_x \\ \sigma_y \\ \sigma_z \\ \tau_{yz} \\ \tau_{xz} \\ \tau_{xy} \\ D_x \\ D_y \\ D_z \end{bmatrix} = \begin{bmatrix} C_{11} & C_{12} & C_{13} & 0 & 0 & 0 & 0 & 0 & -e_{31} \\ C_{12} & C_{22} & C_{23} & 0 & 0 & 0 & 0 & 0 & -e_{32} \\ C_{13} & C_{23} & C_{33} & 0 & 0 & 0 & 0 & 0 & -e_{33} \\ 0 & 0 & 0 & C_{44} & 0 & 0 & 0 & -e_{24} & 0 \\ 0 & 0 & 0 & 0 & C_{55} & 0 & -e_{15} & 0 & 0 \\ 0 & 0 & 0 & 0 & 0 & C_{66} & 0 & 0 & 0 \\ 0 & 0 & 0 & 0 & e_{15} & 0 & \epsilon_1 & 0 & 0 \\ 0 & 0 & 0 & e_{24} & 0 & 0 & 0 & \epsilon_2 & 0 \\ e_{31} & e_{32} & e_{33} & 0 & 0 & 0 & 0 & 0 & \epsilon_3 \end{bmatrix} \begin{bmatrix} \varepsilon_x \\ \varepsilon_y \\ \varepsilon_z \\ \gamma_{yz} \\ \gamma_{xz} \\ \gamma_{xy} \\ E_x \\ E_y \\ E_z \end{bmatrix} \tag{A.1}$$

in which σ, τ, ε, γ, D and E denote normal stress (N/m^2), shear stress (N/m^2), normal strain, shear strain, electric displacement (C/m^2) and electric field (V/m), respectively.

For a one-dimensional beam, plane stress condition exists and also the width in y-direction is stress-free. Hence we can set $\sigma_y = \sigma_z = \tau_{yz} = \tau_{xy} = \gamma_{yz} = \gamma_{xy} = 0$, while $\varepsilon_y \neq 0$; $\varepsilon_z \neq 0$. For electric fields, we can assume $E_x = E_y = 0$. Only the coupling between the longitudinal motion and transverse electric field is effective for extension mode beams, hence we can neglect other coupling coefficients. Using these conditions in Eq. (A.1), the reduced form of relations can be written as:

$$\begin{bmatrix}\sigma_x\\ \tau_{xz}\\ D_z\end{bmatrix}=\begin{bmatrix}\tilde{Q}_{11} & 0 & -\tilde{e}_{31}\\ 0 & \tilde{Q}_{55} & 0\\ \tilde{e}_{31} & 0 & \tilde{\epsilon}_3\end{bmatrix}\begin{bmatrix}\varepsilon_x\\ \gamma_{xz}\\ E_z\end{bmatrix} \tag{A.2}$$

where

$\tilde{Q}_{11}=Q_{11}-(Q_{12}^2/Q_{22})$, $\tilde{Q}_{55}=Q_{55}$ and $Q_{ij}=C_{ij}-\left(\frac{C_{i3}C_{j3}}{C_{33}}\right)$ $(i,j=1,2,5)$;
$\tilde{e}_{31}=\bar{e}_{31}-\bar{e}_{32}\left(\frac{Q_{12}}{Q_{22}}\right)$ and $\bar{e}_{3i}=e_{3i}-e_{33}\,(C_{i3}/C_{33})$ $(i=1,2)$;
$\tilde{\epsilon}_3=\bar{\epsilon}_3+(\bar{e}_{32}^2/Q_{22})$ and $\bar{\epsilon}_3=\epsilon_3+(e_{33}^2/C_{33})$.

For Euler-Bernoulli beam theory which neglects the shear effects, Eq. (A.2) reduces to:

$$\begin{bmatrix}\sigma_x\\ D_z\end{bmatrix}=\begin{bmatrix}\tilde{Q}_{11} & -\tilde{e}_{31}\\ \tilde{e}_{31} & \tilde{\epsilon}_3\end{bmatrix}\begin{bmatrix}\varepsilon_x\\ E_z\end{bmatrix} \tag{A.3}$$

APPENDIX B

COMPARATIVE EVALUATION OF THE BEAM FORMULATIONS

A comparative evaluation of all the ESL piezoelectric beam finite element formulations is presented. The test problem chosen is a G1195N bimorph, which has highest thickness ratio with a very high piezoelectric coupling coefficient. The geometric parameters are: length $L = 100\ mm$ and height $h = 10\ mm$. The results from the conventional EBT (Bendary et al., 2010), FSDT (Narayanan and Balamurugan, 2003), HSDT (Elshafei and Alraiess, 2013), EBT-*Coupled*, FSDT-*Coupled* and HSDT-*Coupled*, for static and modal analyses, are tabulated in Table B.1. Also, the errors (in percentage) with respect to the benchmark solutions from ANSYS 2D analysis are given in brackets.

Table B.1: Comparative evaluation of piezoelectric beam finite elements for the analysis of the G1195N bimorph cantilever beam ($h=10\ mm,\ L=100\ mm$)

	Conventional			Coupled			ANSYS -2D
	EBT	FSDT	HSDT	EBT	FSDT	HSDT	
Tip defection (μm) for actuation by *±10 volts*	0.762 (6.72 %)	0.762 (6.72 %)	0.762 (6.72 %)	0.713 (-0.14 %)	0.713 (-0.14 %)	0.713 (-0.14 %)	0.714
Tip defection (μm) for a tip load of *-1000 N*	-52.8 (4.55 %)	-53.2 (5.34 %)	-53.3 (5.54 %)	-50.0 (-0.99 %)	-50.4 (-0.19 %)	-50.5 (0.00 %)	-50.5
Potential at root (*volts*) for a tip load of *-1000 N*	208.9 (4.55 %)	210.4 (5.30 %)	211.1 (5.65 %)	198.1 (-0.85 %)	199.4 (-0.20 %)	199.8 (0.00 %)	198.8
First natural frequency (*Hz*) in open circuit	509.2 (-2.03 %)	506.2 (-2.61 %)	505.5 (-2.75 %)	523.3 (0.67 %)	520.3 (0.09%)	519.4 (-0.07 %)	519.8
First natural frequency (*Hz*) in closed circuit	464.2 (-2.72%)	461.9 (-3.20%)	461.5 (-3.29%)	479.7 (0.52 %)	477.6 (0.08 %)	477.0 (-0.04%)	477.2

Results from the present *Coupled* formulations closely match with the ANSYS 2D benchmark solutions, while the conventional formulations show significant errors. In the sensor configuration, the effects of shear deformation can be seen from the results of a tip loaded cantilever. In the actuator configuration, EBT, FSDT and HSDT predict the same value for tip defection, as a constant moment (no shear effects) is induced due to actuation in bimorph.

LIST OF PAPERS BASED ON THESIS

Papers in Refereed International Journals

1. **Litesh N Sulbhewar** and P. Raveendranath (2013) Assessment of induced potential effects on the performance of piezoelectric beam finite elements. ***International Journal of Aerospace and Lightweight Structures***, 3(4), 513-530.
2. **Litesh N Sulbhewar** and P. Raveendranath (2014) A novel efficient coupled polynomial field interpolation scheme for higher order piezoelectric extension mode beam finite elements. ***Smart Materials and Structures***, 23(2), 25024-25033.
3. **Litesh N Sulbhewar** and P. Raveendranath (2014) An accurate higher-order modelling of extension mode smart beams with consistent through-thickness electric potential distribution. ***Journal of Intelligent Material Systems and Structures***, In press (doi:10.1177/1045389X14538531).
4. **Litesh N Sulbhewar** and P. Raveendranath (2014) A numerically accurate and efficient coupled polynomial field interpolation for Euler-Bernoulli piezoelectric beam finite element with induced potential effect. ***Journal of Intelligent Material Systems and Structures*** -In press (doi: 10.1177/1045389X14544149).
5. **Litesh N Sulbhewar** and P. Raveendranath (2014) A conistently efficient and accurate HSDT-based finite element to model extension mode piezoelectric smart beams. ***Journal of Intelligent Material Systems and Structures*** -(Under review after a minor revision).
6. **Litesh N Sulbhewar** and P. Raveendranath (2014) An accurate novel coupled field Timoshenko piezoelectric beam finite element with induced potential effects. ***Latin American Journal of Solids and Structures***, 11(9), 1628-1650.
7. **Litesh N Sulbhewar** and P. Raveendranath (2014) An efficient coupled polynomial interpolation scheme to eliminate material-locking in the Euler-Bernoulli

piezoelectric beam finite element. ***Latin American Journal of Solids and Structures***-In press.

8. **Litesh N Sulbhewar** and P. Raveendranath (2014) A locking-free coupled polynomial Timoshenko piezoelectric beam finite element. ***Engineering Computations***-In press.

9. **Litesh N Sulbhewar** and P. Raveendranath (2014) Performance of consistent through-thickness electric potential distribution for Euler-Bernoulli piezoelectric beam finite elements. ***International Journal of Computer Aided Engineering and Technology***-In press.

10. **Litesh N Sulbhewar** and P. Raveendranath (2014) An accurate modeling of piezoelectric smart beams with first order shear deformation theory. ***International Journal of Modeling, Simulation, and Scientific Computing*** -(Under review after a minor revision).

Presentations in Conferences

1. **Litesh N Sulbhewar** and P. Raveendranath (2014) Geometric effects on the accuracy of Euler-Bernoulli piezoelectric smart beam finite elements, ***Advanced Materials Research***, 984-985, 1063-1073 (doi:10.4028/www.scientific.net/AMR.984-985.1063).

2. **Litesh N Sulbhewar** and P. Raveendranath (2013) Importance of accommodating induced potential effects in modeling of piezoelectric smart beams, In *Proc. NUiCONE 2013*, In press.

3. **Litesh N Sulbhewar** and P. Raveendranath (2014) An efficient way to incorporate shear flexibility in piezoelectric smart beam finite elements, In *Proc. ICKCE 2014*, In press (IEEE Xplore).

4. **Litesh N Sulbhewar** and P. Raveendranath (2014) Effect of higher order through-thickness potential on the performance of Timoshenko piezoelectric smart beam finite elements, In *Proc. ISCO 2014*, In press (IEEE Xplore).

5. **Litesh N Sulbhewar** and P. Raveendranath (2014) On the use of higher order polynomial interpolation to alleviate material locking in piezoelectric beam finite elements, In *Proc. ICCSET 2014*, In press (IEEE Xplore).

Papers Communicated to Refereed Journals

1. **Litesh N Sulbhewar** and P. Raveendranath (2014) A Timoshenko piezoelectric beam finite element with consistent performance irrespective of geometric and material configurations. *Latin American Journal of Solids and Structures*-Under review.

Nomination

The synopsis of present research work was shortlisted among first 10 nominations (from over 50 nominations received worldwide) for the **ISSS Student Award (PhD)** competition organized by *Institute of Smart Structures and Systems, Indian Institute of Science (IISc), Bangalore* during the 7^{th} *ISSS conference*, July-2014.